Tuning the magnetic interactions in GaAs:Mn/MnAs hybrid structures by controlling shape and position of MnAs nanoclusters

DISSERTATION
zur Erlangung des Doktorgrades
der Naturwissenschaften
(Dr. rer. nat.)

vorgelegt von

Dipl.-Phys. Matthias Thomas Elm

- anno 2010 -

JUSTUS-LIEBIG-
UNIVERSITÄT
GIESSEN

I. Physikalisches Institut
Justus-Liebig-Universität Gießen

Contents

Introduction

The realization of magnetoelectronic and spintronic devices is of great interest in the field of electronic devices, because such devices offer extended functionalities by not only using the charge of the electron for information transfer and storage but also the intrinsic angular momentum of the electron, the spin. As an example for such an extended functionality one may mention the non-volatility of the stored information in magnetic random access memory (MRAM). In contrast to the storage media commonly used today like dynamic random access memory (DRAM) in MRAMs the information is not stored electronically but via the magnetization orientation of a magnetic device. The advantage of magnetoelectronic devices is, that the information does not need to be renewed permanently and even is conserved after the shut-down of the power supply. Furthermore, MRAM's consist of metals which makes them more robust and miniaturizable than doped semiconductors. Therefore, magnetoelectronics and spintronics will play a key role for future micro- and nanostructured devices.

The magnetoelectronic devices used today are based in their operation mode mostly on metals, i.e. ferromagnetic metals are used to introduce spin orientation, where the relative change in the resistivity depending on the orientation of the magnetization in the metals is utilized. All the metal-based devices have in common, that their Curie temperatures are much larger than room temperature and that quantum effects only occur at size scales much smaller than the structural size of current devices.

The electron spin is not utilized yet in the semiconductor-based electronic or optoelectronic devices. Nevertheless in semiconductors a considerable degree of spin-polarization can be generated in several ways, e.g. by optical excitation, spin-injection or by spin alignment in a paramagnetic (giant Zeeman splitting in the present of an external magnetic field) or ferromagnetic semiconductor (spontaneous magnetization) [1, 2, 3]. But so far, this is generally only possible for temperatures below room temperatures, which hinders most technological applications. On the other hand, a transformation of spin information into polarized photons in the field of spin optoelectronics can easily be realised with semiconductor devices. The great challenge for the future is the combination of the advantages of both, metal-based magnetoelectronics and semiconductor-based electronics which is the mayor aim in the field of spintronics.

In their simplest form all magnetoelectronic devices consist of two magnetic layers which are separated by a diamagnetic layer beeing either a diamagnetic metal (giant magneto-resistance or GMR-structure)[4, 5] or an insulator (tunneling magneto-resistance or TMR-structure) [6]. The operation of these devices is based on the effect, that the electric resistance of the layered

structure depends on the relative orientation of the magnetization of the
two magnetic layers. The resistance through the layer system is large, if the
magnetizations of the layers are aligned antiparallel. The physical origin of
this effect is strong spin-dependent scattering at the interfaces between the
layers of different magnetic orientation. In the case of a parallel alignment of
the layer's magnetizations, this spin-dependent scattering is reduced leading
to a decreased resistivity. Today GMR- and TMR- structures are employed in
contact-free sensors, magnetic memory, hard-disk reading-heads etc. However,
the device geometry as a layered structure, where the current is mostly applied
perpendicular to the layers, is not ideally suited for integrating these devices
into larger planar structures and to miniaturize them further.

Interesting alternative material systems for new magnetoelectronic devices may
be the so called granular semiconductor-ferromagnet hybrid structures, which
offer the possibility to circumvent the disadvantages mentioned. Granular
hybrid structures consisting of ferromagnetic nanoscale clusters embedded
in a semiconducting matrix material or arranged on the surface combine
ferromagnetic and semiconducting properties in one material system and show
magneto-resistance effects somewhat similar to the GMR- or TMR-effect [7, 8].
In addition, their properties can be tuned in a wide range. This tunability
arises from the larger number of degrees of freedom in this composite hybrid
compared to a single-phase material, e.g. the mean distance between the
clusters, the cluster size and the cluster shape which contribute to a large
extent to the properties of the hybrid [9, 10] can be adjusted separately.
In conventionally synthesised granular hybrid structures the clusters grow
randomly in the host matrix during the growth process. The random cluster
distribution leads to significant variations in the transport behaviour [11],
which is a mayor obstacle in employing such hybrids in devices. Therefore,
the technological application of conventionally grown granular hybrids has
been mainly restricted to macroscopic devices, i.e. where the mean distance
between the clusters is much smaller than the characteristic size of the device.
Macroscopic devices allow one to take advantage of the tuneability of the
hybrid's properties whilst avoiding problems due to statistical fluctuations in
cluster size, number, etc. But, still, hybrids with a random cluster distribution
are not suitable for miniaturized devices and, therefore, they will not play a
role in the long run for nanoelectronics.

A solution for avoiding randomness of cluster distributions, sizes and shapes
may be the new method of selective-area growth of self-assembled MnAs
nanoclusters on pre-patterned (111)B-GaAs substrates. With this method it
is possible to control the spatial arrangement of the clusters on the surface,
the cluster size and also their shape. Therefore, this method can overcome the
problem of randomness of cluster growth and has the potential to actively tune
the structure of individual clusters in order to optimize the sample properties
for new planar magnetoelectronic devices.

In this thesis the magnetic and magneto-transport properties of hybrids
with randomly arranged hexagon-shaped MnAs nanoclusters grown by stan-
dard metal-organic vapour-phase epitaxy (MOVPE) as well as of ordered
arrangements of elongated nanoclusters and cluster chains grown by the new

method of selective-area MOVPE are investigated. The investigation of both the magnetic as well as the magneto-transport properties of such structures is essential in order to access the potential of such structures for device applications, on the one hand, and to understand the physical background of the influence of the clusters on the transport properties and the underlying microscopic mechanisms, on the other hand.

This thesis is divided into four chapters. The first chapter gives an overview of the different kinds of magnetism in solids, where the main focus lies on ferromagnetism. Also the influence of a magnetic field on the transport properties and different resulting magnetoresistance effects are discussed. The second chapter describes the growth of the investigated samples with a random cluster distribution as well as the method of selective-area MOVPE, which was used in order to grow different cluster arrangements. In the next two chapters the experimental results are presented. The third chapter deals with the magnetic properties of the clusters, while in the fourth chapter the influence of the different cluster arrangements on the transport behaviour of the samples is discussed. At the end a summary of the obtained results and an outlook for further investigations is given.

1 Theoretical background

Dilute magnetic semiconducutors (DMS) as well as granular hybrid structures combine ferromagnetic and semiconducting properties in one material system which makes them possible candidates for new spintronic and magnetoelectronic devices. The atoms with a large magnetic moment and in the case of the hybrids also the ferromagnetic inclusions, which are incorporated during the growth process, strongly influence the magnetic as well as the transport properties of the hybrids. In order to optimize these material systems for devices it is necessary to understand the interaction of the magnetic atoms with each other and the influence of the magnetic inclusions on the hybrid's properties. In this first chapter the theoretical background for describing the magnetic interaction and the different kinds of magnetism are shortly described, whereas the main focus lies on the origin of ferromagnetic coupling. This chapter also covers the formation of a domain structure and the magnetic anisotropy of single ferromagnets like the ferromagnetic nanoclusters in the investigated hybrids. Finally, the third part gives an overview of different magnetoresistance effects, which can occur in bulk material, like the ordinary and the anisotropic magnetoresistance effect, or in layered systems, like the giant- and the tunnel-magnetoresistance effect.

1.1 Magnetism in solids

Due to their interaction with an external magnetic field, solids can be divided into three different kinds of magnetic materials, in diamagnetic and paramagnetic materials, where no explicit interaction between the single magnetic moments occurs and in ferro-, ferri- and antiferromagnetic materials (collective magnetism) where the single magnetic moments interact with each other. This coupling leads to a spontaneous magnetization below a certain temperature even without an external magnetic field.

The magnetism in solids can be described with the following material equation:

$$\vec{B} = \mu_0(\vec{H} + \vec{M}),\qquad(1.1)$$

where $\vec{B}$ is the magnetic flux density, μ_0 is the magnetic permeability constant, $\vec{H}$ is the external magnetic field and $\vec{M}$, which is defined as the magnetic moment per unit volume, is the magnetization of the material. For small magnetic fields the magneti is proportional to $\vec{H}$:

$$\vec{M} = \chi\vec{H},\qquad(1.2)$$

where χ is known as the magnetic susceptibility. In general, the magnetic susceptibility is a tensor, which depends on the magnetic field and the temperature. The single tensor elements are given by the first derivative of the magnetization after the field:

$$\chi_{ij} = \frac{\partial M_i}{\partial H_j}. \tag{1.3}$$

For the magnetic flux density follows:

$$\vec{B} = \mu_0(\vec{H} + \vec{M}) = \mu_0(\vec{H} + \boldsymbol{\chi}\vec{H}). \tag{1.4}$$

Before the different kinds of magnetism are discussed it should be mentioned, that magnetism is a purely quantum mechanical phenomenon. For a strictly classical system at thermal equilibrium no macroscopic magnetic moment can occur. This is known as the Bohr-van Leuween-theorem [12, 13]. In classical statistical mechanics the magnetization of N magnetic moments in a unit volume V is given by:

$$M = -\frac{N}{V}\frac{\partial F}{\partial B}, \tag{1.5}$$

with the free energy F given by the expression:

$$F = -k_{\mathrm{B}}T\ln(Z), \tag{1.6}$$

where k_{B} is the Boltzmann constant and T is the temperature. The partition function Z is an integral over a $6N$-dimensional N-electron phase space:

$$Z = \frac{1}{N!h^{3N}} \int\int \prod_{i=1}^{N} d\vec{p}_i d\vec{x}_i \exp(-\beta H(\vec{p}_1, ..., \vec{p}_N, \vec{x}_1, ..., \vec{x}_N)) \tag{1.7}$$

with the Planck constant h, $\beta = k_{\mathrm{B}}T$ and the classical Hamiltonfunction

$$H = \sum_{i=1}^{N} \frac{1}{2m_{\mathrm{e}}} \left(\vec{p}_i + e\vec{A}(\vec{x}_i)\right)^2 + \varphi(\vec{x}_1, ..., \vec{x}_N), \tag{1.8}$$

where m_{e} is the electron mass, e is the electron charge, $\vec{A}$ is the magnetic vector potential, φ is the electrical potential, and $\vec{p}_i$ and $\vec{x}_i$ denote the momentum and position of the ith electron, respectively. The magnetic field only enters in the form $\vec{p}_i + e\vec{A}(\vec{x}_i)$ where it may be eliminated by a simple shift of the origin of the momentum integrations, which run from $-\infty$ to ∞ and are therefore unaffected by the shift. Therefore the free energy F is independent of the magnetic field and the magnetization, which is proportional to $\partial F/\partial B$, vanishes. Thus a quantum theoretical treatment is needed in order to describe any magnetic phenomenon.

There are three different origins for the magnetic moment of atoms: the electron spin, their orbital angular momentum about the nucleus, and the change in the orbital momentum induced by an applied magnetic field. While the first two effects give a paramagnetic contribution, the last one results in a diamagnetic behaviour of the atom.

1.1.1 Diamagnetism

Diamagnetism occurs in every solid, but only in solids where the diamagnetic contribution is not dominated by paramagnetic or collective magnetism contributions, one speaks of a diamagnetic material. The term diamagnetism is applied to every material with a negative susceptibility, where the magnetic moments, which are induced by a magnetic field, are opposite to the applied field. This is similar to Lenz's law in electromagnetism, where the change of the flux through an electrical circuit induces a current to oppose the flux change. There are two major kinds of diamagnetism: the diamagnetism of atoms which is known as Larmor-diamagnetism and the diamagnetism of conducting electrons known as Landau-diamagnetism.

Larmor-diamagnetism
The Larmor-diamagnetism occurs in single atoms and ions with completely filled shells. The diamagnetic contribution to the magnetic susceptibility[1] in this case is:

$$\chi_{\text{Larmor}} = \frac{\mu_0 N m}{BV} = -\frac{\mu_0 N Z e^2}{6 m_e V} \langle r^2 \rangle, \tag{1.9}$$

where N is the number of atoms per unit volume V, Z is the number of electrons of the atom, $\langle r^2 \rangle$ is the mean square distance of the electrons from the nucleus, and μ_0 is the permeability constant. The magnetic moment $\vec{m}$ is therefore given by:

$$\vec{m} = -\frac{e^2 \langle r^2 \rangle}{6 m_e} \vec{B}. \tag{1.10}$$

This result for the Larmor-diamagnetic contribution to the magnetic response describes the suceptibility of noble gases and of simple ions with filled shells, such as Na^+ or Cl^-, in good agreement with the experimental results.

Landau-diamagnetism
In the case of solids the conduction electrons also show a diamagnetic contribution, which is known as Landau-diamagnetism. This diamagnetic contribution arises from the coupling of the applied field to the orbital motion of the electrons. In the case of a free electron gas like in metals the magnetic field leads to a energy-quantization of the electron wave vector in the plane perpendicular to the direction of the magnetic field, while the electron motion along the field direction is not affected. The resulting energy levels are called Landau-levels. The change of the system's energy due to the applied magnetic field leads to a magnetization (see (1.5)). This is the Landau-diamagnetism and the Landau-susceptibility is given by:

$$\chi_{\text{Landau}} = -\frac{1}{6} \mu_0 \mu_B^2 g_0^2 D(E_F), \tag{1.11}$$

where $g_0 = 2$ is the so-called g-factor of the free electron, $\mu_B = \frac{e\hbar}{2m_e}$ is the Bohr-magneton, $D(E_F)$ is the density of states at the Fermi-energy E_F and $\hbar$ is the Planck constant h divided by 2π.

---

[1]also known as diamagnetic Langevin suceptibility

1.1.2 Paramagnetism

A paramagnetic behaviour can be found in atoms, ions or solids which possess permanent magnetic moments. Without an external magnetic field the magnetic moments are statistically distributed due to the thermal energy, so that no resulting magnetization is observable. Applying a magnetic field leads to an alignment of the magnetic moments along the field direction, which is in competition to their thermal motion, and leads to a positive magnetic susceptibility. As for the diamagnetism one distinguishes between the paramagnetism of free atoms (Langevin-paramagnetism) and the paramagnetism of the itinerant moments of the conduction electrons (Pauli-paramagnetism).

Langevin-paramagnetism and the Curie-Law
The magnetic moments of atoms or ions which are responsible for the Langevin-paramagnetism result from partially filled electron shells. The magnetic moment of a single atom is given by:

$$\vec{m}_J = -g\mu_{\mathrm{B}}\vec{J},\tag{1.12}$$

where the total angular momentum $\vec{J}$ is the sum of the orbital angular momentum $\vec{L}$ and the spin angular momentum $\vec{S}$ and g is the Landé-factor:

$$g = 1 + \frac{J(J+1) + S(S+1) - L(L+1)}{2J(J+1)}.\tag{1.13}$$

The total angular momentum is quantized along a certain direction. If the quantization axis is chosen along the z-direction the z-component for the magnetic moment $\vec{m}_J$ is given by:

$$m_z = -g\mu_{\mathrm{B}}m_J \quad \text{with} \quad m_J = -J, -J+1, ..., J.\tag{1.14}$$

If a magnetic field is applied along the z-direction the degeneracy of these $2J+1$ energy levels is lifted and the corresponding energies are:

$$E_J = -\vec{m}_J\vec{B} = -m_z B = -g\mu_{\mathrm{B}}m_J B,\tag{1.15}$$

The partition function Z of such a system is then given by:

$$Z = \sum_{m_J=-J}^{J} exp\left(\frac{E_J}{k_{\mathrm{B}}T}\right) = \sum_{m_J=-J}^{J} exp\left(\frac{-g\mu_{\mathrm{B}}m_J B}{k_{\mathrm{B}}T}\right).\tag{1.16}$$

This expression can easily be calculated using the geometric series, which leads to:

$$Z = \frac{e^{(\beta g\mu_{\mathrm{B}}B(J+1/2))} - e^{(-\beta g\mu_{\mathrm{B}}B(J+1/2))}}{e^{(\beta g\mu_{\mathrm{B}}B/2)} - e^{(-\beta g\mu_{\mathrm{B}}B/2)}},\tag{1.17}$$

with $\beta = \frac{1}{k_{\mathrm{B}}T}$.

Using (1.6) the magnetization of N such atoms in a volume V is given by:

$$M = -\frac{N}{V}\frac{\partial F}{\partial B} = \frac{N}{V}g\mu_{\mathrm{B}}JB_J(\beta g\mu_{\mathrm{B}}JB),\tag{1.18}$$
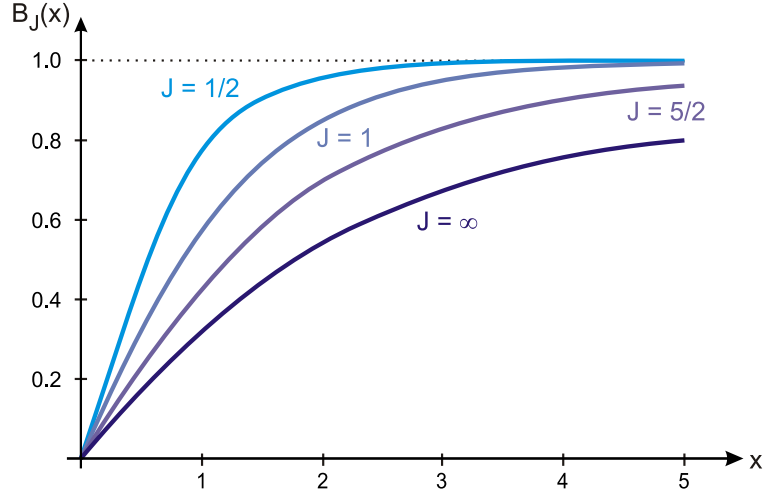
Figure 1.1: Plot of the Brillouin function $B_J(x)$ for different values of the total angular momentum J.

with the Brillouin function $B_J(x)$, which is defined by:

$$B_J(x) = \frac{2J+1}{2J} \coth\left(\frac{2J+1}{2J}x\right) - \frac{1}{2J}\coth\left(\frac{1}{2J}x\right) \tag{1.19}$$

and shown in Figure 1.1 for different values of J.

In the limit $T \to 0$ or $B \to \infty$ the magnetization reaches a maximum value M_s, which is called the saturation magnetization:

$$M_\mathrm{s} = \frac{N}{V}g\mu_\mathrm{B}J, \tag{1.20}$$

i.e. in this case all the magnetic moments are aligned along the direction of the magnetic field. A more important limit is the case of high temperature and low magnetic field, i.e. $g\mu_\mathrm{B}B \ll k_\mathrm{B}T$. In this case the Brillouin function can be written as a Taylor expansion:

$$\coth(z) \approx \frac{1}{z} + \frac{1}{3}z + O(z^3), \quad B_J(x) \approx \frac{J+1}{3J}x + O(x^3). \tag{1.21}$$

The magnetic suceptibility can then be written as:

$$\chi_\mathrm{Langevin} = \frac{N}{V}\frac{\mu_0\mu_\mathrm{B}^2 g^2}{3}\frac{J(J+1)}{k_\mathrm{B}T} = \frac{C}{T}. \tag{1.22}$$

This is the Curie-law with the Curie constant C:

$$C = \frac{N}{V}\frac{\mu_0\mu_\mathrm{B}^2 g^2}{3}\frac{J(J+1)}{k_\mathrm{B}}. \tag{1.23}$$

The paramagnetic suceptibility (1.22) at room temperature is about a factor of 500 larger than the Larmor-diamagnetic suceptibility (1.9). For systems
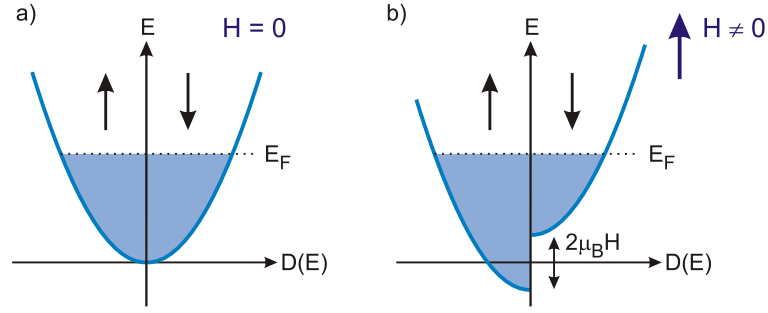
Figure 1.2: Pauli-paramagnetism at zero temperature. a) Without an external
           magnetic field the bandstructure is spin degenerated. b) Applying
           a magnetic field leads to a band splitting and a redistribution of the
           electrons, which is the origin of the Pauli-paramagnetism.

with atoms with partially filled shells the diamagnetic contribution is therefore
dominated by the paramagnetic behaviour.

Pauli-paramagnetism

The paramagnetic contribution of the conduction electrons in solids arises from
the splitting of the energy bands with different spin orientation when a mag-
netic field is applied, which is shown schematically in Figure 1.2. Due to this
Zeemann-splitting the density of states of each spin direction is shifted by:

$$\Delta E = \pm g_0 \mu_B m_s B = \pm \mu_B B, \tag{1.24}$$

where $g_0 = 2$ is the g-factor and $m_s = 1/2$ is the spin quantum number of the
electron. The band splitting leads to a redistribution of the electron occupation
in each band in order to achieve a uniform energy level at the Fermi energy.
The difference in the occupation number of the spins with different orientations
leads to the Pauli-paramagnetism with the magnetization:

$$M = \mu_B^2 D(E_F) B \tag{1.25}$$

and the Pauli-susceptibility:

$$\chi_{\text{Pauli}} = \mu_0 \mu_B^2 D(E_F). \tag{1.26}$$

1.1.3 Ferromagnetism

Ferromagnetism is a collective phenomenon, where the magnetic moments of
single atoms interact with each other. Due to this interaction a ferromagnet
possesses a spontaneous magnetic ordering below a certain temperature, the so-
called Curie-temperature T_C, i.e. the magnetic moments tend to align parallel
to each other. Above the Curie-temperature the magnetic moments lose their
ordered state because of thermal excitation and the material behaves like a
paramagnet.

The Curie-Weiss law

In order to describe a ferromagnetic behaviour, one may assume an internal exchange field, which lines up neighbouring magnetic moments parallel to each other. This exchange field is also called molecular field or Weiss-field, after Pierre Weiss, who was the first who postulated such a field in 1907 [14]. In the mean field approximation each magnetic moment now experiences an exchange field $\vec{B}_{\mathrm{E}}$ proportional to the existing magnetization even without an external magnetic field:

$$\vec{B}_{\mathrm{E}} = \mu_0 \lambda_{\mathrm{W}} \vec{M}, \tag{1.27}$$

where λ_{W} is called the molecular-field or Weiss-field constant which correlates the magnetization with the exchange field. By introducing B_{E} a ferromagnet in an external field B_0 can be considered as a Langevin-paramagnet which experiences a total field B_{tot} given by:

$$B_{\mathrm{tot}} = B_0 + \mu_0 \lambda_{\mathrm{W}} M. \tag{1.28}$$

The magnetization is then given by (1.18):

$$M = M_{\mathrm{s}} B_J(y) \tag{1.29}$$

$$\mathrm{with} \quad y = \frac{g\mu_{\mathrm{B}} J(B_0 + \mu_0 \lambda_{\mathrm{W}} M)}{k_{\mathrm{B}} T}. \tag{1.30}$$

At high temperatures above the Curie-Temperature T_{C}, where the magnetic moments lose their ferromagnetic ordering, the Brillouin function may again be written as a Taylor expansion (1.21) and for the magnetization follows:

$$M = \frac{N}{V} \frac{\mu_{\mathrm{B}}^2 g^2}{3} \frac{J(J+1)}{k_{\mathrm{B}} T} (B_0 + \mu_0 \lambda_{\mathrm{W}} M) = \frac{C}{T} (H + \lambda_{\mathrm{W}} M), \tag{1.31}$$

where C again is the Curie constant. The magnetic suceptibility can then be written as:

$$\chi = \frac{C}{T - \lambda_{\mathrm{W}} C} = \frac{C}{T - \Theta}. \tag{1.32}$$

This equation is known as the Curie-Weiss law and Θ is called the Curie-Weiss parameter. At $T = \Theta$ the susceptibility diverges, which means that one gets a non-zero magnetization even without an external magnetic field. Therefore, for a ferromagnet, Θ can be interpreted as the Curie-temperature, which is then given by:

$$T_{\mathrm{C}} = \Theta = \lambda_{\mathrm{W}} C = \frac{N}{V} \frac{\lambda_{\mathrm{W}} \mu_0 \mu_{\mathrm{B}}^2 g^2}{3} \frac{J(J+1)}{k_{\mathrm{B}}}. \tag{1.33}$$

In the limit $T \to 0$ and $B_0 = 0$ the magnetization reaches the saturation value

$$M(T=0) = M_{\mathrm{s}}(0) = \frac{N}{V} g\mu_{\mathrm{B}} J, \tag{1.34}$$

where all magnetic moments are aligned along one direction. The temperature dependence of the saturation magnetization between $T = 0$ and the Curie-temperature in the case of $B_0 = 0$ can be written as:

$$\frac{M_{\mathrm{s}}(T)}{M_{\mathrm{s}}(0)} = B_J \left(\frac{g\mu_{\mathrm{B}} J \mu_0 \lambda_{\mathrm{W}} M_{\mathrm{s}}(T)}{k_{\mathrm{B}} T} \right). \tag{1.35}$$
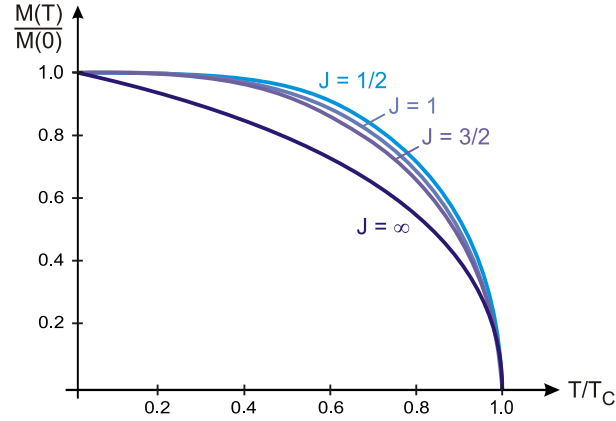
Figure 1.3: Temperature dependence of the reduced saturation magnetization $M_s(T)/M_s(0)$ for different values of J plottet versus the reduced temperature T/T_C.

Using equation (1.34) and the relation $\lambda_W = T_C/C$ one obtains:

$$\frac{M_s(T)}{M_s(0)} = B_J \left(\frac{3J}{J+1} \frac{T_C}{T} \frac{M_s(T)}{M_s(0)} \right), \tag{1.36}$$

which can be solved numerically or graphically. The result for different values of J is shown in Figure 1.3.

The phenomenological theory of Weiss describes many ferromagnetic materials very well, e.g. iron ($T_C = 1044$ K) and nickel ($T_C = 627$ K), although they have strongly differing Curie temperatures. However, Weiss theory gives no explanation for the origin of the exchange field and the resulting ferromagnetic ordering.

The exchange interaction
The origin of the exchange field cannot be explained classically. The classical interaction, which may be responsible for a ferromagnetic coupling between magnetic moments, is the direct dipole-dipole interaction. For two neighbouring magnetic moments separated by a distance a, typically a few Å, the dipole-dipole interaction is of the order of:

$$E \sim 2\frac{\mu_0 \mu_B^2}{4\pi a^3} \approx 1.6 \cdot 10^{-23}\,\text{J} \approx k_B \cdot 1.8\,\text{K}, \tag{1.37}$$

which is too small to explain ferromagnetism at temperatures above a few Kelvin. Instead the ferromagnetic ordering originates from the so-called exchange interaction, which is a consequence of the Pauli principle and the Coulomb interaction. The Pauli principle, which results from the quantum mechanical principle of indistinguishability of particles, prohibits that two electrons at the same place have completely the same quantum numbers. Because of this principle, for example, two electrons whose spins are aligned parallel have a larger distance from each other and therefore a lower Coulomb energy

compared to two electrons with antiparallel spins. At the same time, their kinetic energy is larger because they occupy more extended states.

Therefore the exchange interaction leads to an energy difference between a parallel and an antiparallel alignment of electrons which can be described with the Heisenberg Hamiltonian [15]:

$$\hat{H} = -\sum_{i,j} J_{ij} \hat{\vec{s}}_i \hat{\vec{s}}_j. \tag{1.38}$$

The summation extends over all spin pairs $\hat{\vec{s}}_i$ and $\hat{\vec{s}}_j$ in the lattice and J_{ij} is the so-called exchange integral between spin i and spin j, which depends, amongst other things, on the distance between the position of the two spins i and j. The sign of the exchange integral determines the magnetic coupling between the neighbouring spins. For $J_{ij} > 0$ it comes to a ferromagnetic alignment and for $J_{ij} < 0$ the spins couple antiferromagnetically, i.e. they show an antiparallel alignment.

In solids different types of exchange interaction may occur, which can lead to ferromagnetism:

Direct exchange

In the case of direct exchange the overlap of the electrons' wavefunctions have to be large enough in order to result in a ferromagnetic alignment of the spins, which is schematically shown in figure 1.4 a). Only in some solids this mechanism leads to ferromagnetism, because even in solids the overlap between neighbouring orbitals is usually simply to small. For example in the case of iron the expansion of the wavefunction of the $3d$ electrons, which carry the magnetic moment, is only 1/10 of the distance between the iron atoms. The direct exchange therefore cannot explain the parallel spin alignment in this ferromagnet.

Indirect exchange

More important for a long-range ferromagnetic alignment of the magnetic moments in solids is the indirect exchange, where the electrons' wavefunctions do not directly overlap. Instead the electrons and therefore also their spins can "hop" with a certain probability between neighbouring lattice sites in order to minimize the total energy. Two famous examples for an indirect exchange are the so-called superexchange and the double exchange.

Superexchange occurs for example in manganese oxide, which is schematically shown in figure 1.4 b). In this case the five $3d$ electrons of the Mn^{2+}-ion are aligned parallel according to Hund's rule. Due to the Pauli principle a bonding between the Mn^{2+}-ion and the O^{2-}-ion is only possible, if the electron of the oxygen ion is oriented antiparallel to the $3d$ electrons. Because the p-orbital of the oxygen is completely filled, the two p electrons are oriented antiparallel to each other, which leads, as described above, to an antiparallel bonding of the second Mn^{2+}-ion. The magnetic moments of the two Mn^{2+}-ions are therefore coupled with each other via three antiparallel interactions which leads to an antiferromagnetic ordering of the Mn^{2+}-ions in the material.

The second indirect exchange mechanism, the double exchange, occurs, if both
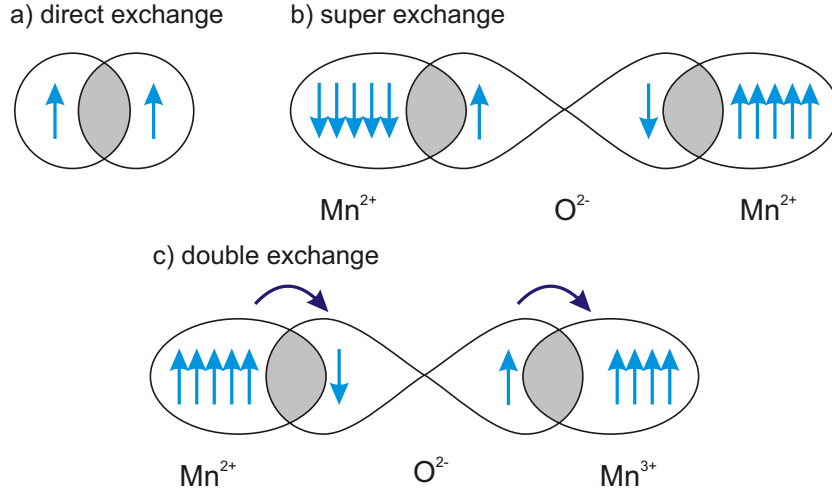
Figure 1.4: Illustration of the direct exchange (a) as well as the superexchange
(b) and the double exchange (c) of manganese oxide as two examples
for indirect exchange.

magnetic ions possess different valence states (figure 1.4 c)). In this case one
electron of the filled $3d$ orbital of the Mn^{2+}-ion can hop via the diamagnetic
O^{2-}-ion into the empty state of the $3d$ orbital of the Mn^{3+}-ion, if the spins
of the Mn-ions are oriented parallel to each other. The hopping process leads
to a reduction of the total energy and therefore to a ferromagnetic alignment
between the Mn ions.

The RKKY-interaction

A further indirect exchange interaction is the Rudermann-Kittel-Kasuya-
Yosida-interaction (RKKY-interaction), which occurs in metals with partially
filled inner shells and delocalised s or p electrons. Especially for rare earth met-
als, this interaction is the most important mechanism which can cause ferro-
and antiferromagnetism. Due to the hyperfine interaction the delocalized con-
duction electrons couple with the magnetic moments of the ions [16]. This
coupling leads to a local change of the spin polarization of the electrons around
the ions, i.e. depending on the distance between electron and magnetic ion the
spin is oriented parallel or antiparallel to the magnetic moment of the ion. The
spin polarization on the other hand influences the other ions and it comes to
a coupling between the magnetic ions mediated by the conduction electrons.
With this model Kasuya [17] and Yosida [18] could explain the magnetic or-
dering of manganese in a copper matrix, which shows either ferromagnetic or
antiferromagnetic behaviour depending on the manganese content in the ma-
trix.

The Heisenberg Hamiltonian describing the RKKY-interaction can be written
as:

$$\hat{H} = -\sum_{i,j} J_{ij}^{\text{RKKY}} \hat{\vec{s}_i} \hat{\vec{s}_j}, \qquad (1.39)$$
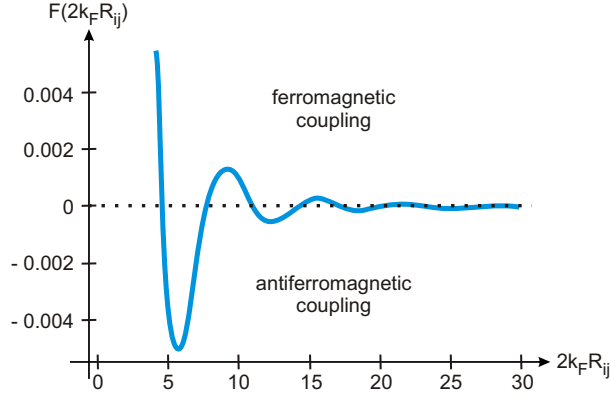
Figure 1.5: Plot of the Friedel oszillation $F(2k_\mathrm{F}R_{ij})$ of the exchange integral J_{ij}^{RKKY}. While for a positive J_{ij}^{RKKY} a ferromagnetic coupling is obtained, a negative J_{ij}^{RKKY} leads to an antiferromagnetic coupling between neighboured spins.

with the exchange integral:

$$J_{ij}^{\mathrm{RKKY}} = \frac{I^2 k_\mathrm{F}^6}{E_\mathrm{F}} \frac{\hbar^2 V^2}{N^2(2\pi^3)} F(2k_\mathrm{F}R_{ij}) \tag{1.40}$$

and

$$F(x) = \frac{\sin(x) - x\cos(x)}{x^4}. \tag{1.41}$$

Here, I is the magnetic moment of the ion, k_F is the Fermi wavevektor and R_{ij} is the distance between the two magnetic moments at position i and j.

The function $F(x)$, which is shown in figure 1.5, and therefore J_{ij}^{RKKY} are oscillating depending on the distance R_{ij}. These oscillations are called Friedel-oscillations and lead to a ferromagnetic coupling for positive values and to an antiferromagnetic coupling for negative values of $F(x)$. The range of the RKKY-interaction is given by:

$$J_{ij}^{\mathrm{RKKY}} \propto \frac{1}{R_{ij}} \tag{1.42}$$

and is in contrast to the direct exchange a long-range interaction.

Itinerant exchange

The ferromagnetism of metals like the transition metals iron, cobalt and nickel cannot be understood with the interaction mechanisms described above. The reason is, that in these metals, the $3d$ electrons, which carry the magnetic moments, are no longer localized but also involved in the bonding. The electrons are therefore delocalized and the original atomic energy levels have broadened into narrow energy bands. The magnetism in such materials is called itinerant-electron magnetism or band-magnetism and results from a spontaneous splitting of the energy bands, which is schematically shown in figure 1.6.

Figure 1.6: Spontaneous splitting of the energy bands for up and down spin even without an external magnetic field.

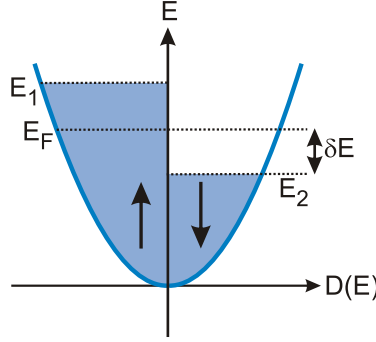The reason for the spontaneous energy splitting is the exchange interaction which favours a parallel alignment of the electron spins. The corresponding energy can be written as:

$$E_{\mathrm{ex}} = J_{\mathrm{eff}} n_\uparrow n_\downarrow, \tag{1.43}$$

where J_{eff} is the effective exchange integral, $n_\uparrow$ and $n_\downarrow$ are the numbers of electrons with spin up and down, respectively, and the sum $n = n_\uparrow + n_\downarrow$ is the total number of $3d$ electrons per atom. Without a band splitting the number of electrons in each spin subband is given by:

$$n_\uparrow = n_\downarrow = \frac{n_\uparrow + n_\downarrow}{2}. \tag{1.44}$$

The gain in exchange energy due to a parallel spin alignment can therefore be written as:

$$\Delta E_{\mathrm{ex}} = J_{\mathrm{eff}} n_\uparrow n_\downarrow - \frac{1}{4} J_{\mathrm{eff}} (n_\uparrow + n_\downarrow)^2 = -\frac{1}{4} J_{\mathrm{eff}} (n_\uparrow - n_\downarrow)^2. \tag{1.45}$$

Due to the redistribution in the band the electrons have to occupy states of higher kinetic energy E_{kin}. For a small displacement $\delta E = E_{\mathrm{F}} - E_2 = E_1 - E_{\mathrm{F}}$ this loss in kinetic energy is given by:

$$\Delta E_{\mathrm{kin}} = \frac{1}{2} (n_\uparrow - n_\downarrow) \delta E, \tag{1.46}$$

and for the total energy variation follows:

$$\Delta E_{\mathrm{tot}} = \Delta E_{\mathrm{ex}} + \Delta E_{\mathrm{kin}} = -J_{\mathrm{eff}} \frac{1}{4} (n_\uparrow - n_\downarrow)^2 + \frac{1}{2} (n_\uparrow - n_\downarrow) \delta E. \tag{1.47}$$

Since $D(E_{\mathrm{F}})\delta E = \frac{1}{2}(n_\uparrow - n_\downarrow)$, one may write:

$$\Delta E_{\mathrm{tot}} = \frac{1}{4} \frac{(n_\uparrow - n_\downarrow)^2}{D(E_{\mathrm{F}})} (1 - J_{\mathrm{eff}} D(E_{\mathrm{F}})). \tag{1.48}$$

If $(1 - J_{\mathrm{eff}} D(E_{\mathrm{F}})) > 0$, the state of lowest energy is achieved if $n_\uparrow = n_\downarrow$ and the system behaves non-magnetic. If $(1 - J_{\mathrm{eff}} D(E_{\mathrm{F}})) < 0$, it comes to a splitting

of the $3d$ band and therefore to a ferromagnetic behaviour. This condition is known as the Stoner-criterion [19]:

$$J_{\text{eff}}D(E_{\text{F}}) > 1. \tag{1.49}$$

A large density of states $D(E_{\text{F}})$ at the Fermi-energy and a large value for J_{eff} lead therefore to ferromagnetism in metals. The density of states of the s and the p electron bands is considerably smaller than that of the d-band. This explains, why itinerant magnetism occurs only in elements with a partially filled d band.

1.2 Properties of ferromagnets

The direct dipole-dipole interaction is, as already mentioned in section 1.1.3, very weak and typically a thousand times smaller than the exchange interaction which is responsible for the ferromagnetic coupling. However, the exchange interaction is a short-range interaction and falls off exponentially with spin separation whereas the dipole-dipole interaction has a range propotional to $1/R^3$. As a consequence, the dipolar energies can have a significant influence on the magnetic properties of a macroscopic ferromagnet, when an enourmous number of spins is involved.

1.2.1 Magnetic anisotropy

Although the Hamiltonian for the exchange interaction (equation (1.38)) has a completely isotropic structure, where the interaction only depends on the angle between the spins, one observes for ferromagnets, that they are easier to magnetize along certain directions. Therefore magnetization curves show a different behaviour for different crystallographic axes, which is shown exemplarily for the $3d$ transition metals iron and nickel in figure 1.7. Because of this magnetic anisotropy the prefered orientation of the magnetization is along a certain
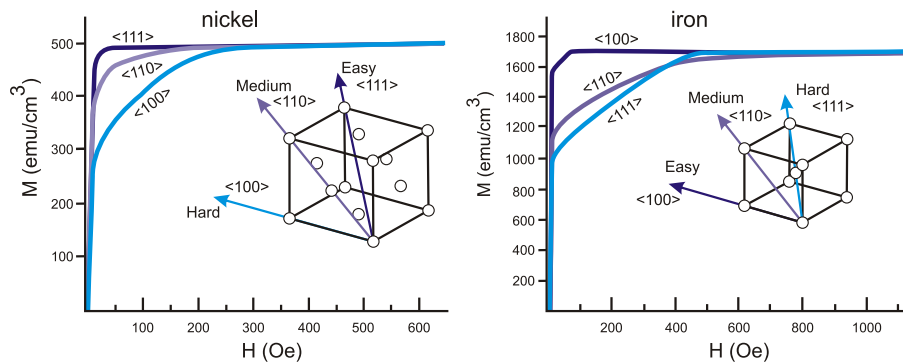

Figure 1.7: Magnetization curves for single crystals of nickel and iron along different crystallographic directions (after [20]).

direction, which is called easy axis. Along this direction a smaller external magnetic field is needed in order to reach the saturation magnetization, which is the $\langle 111 \rangle$-axis in the case of nickel and the $\langle 100 \rangle$-axis in the case of iron. The axis, where the largest field is needed to saturate the magnetization is called hard axis; in the case of nickel it is the $\langle 100 \rangle$-axis and the $\langle 111 \rangle$-axis for iron. The magnetic anisotropy results mainly from two interactions [21], the dipole-dipole interaction:

$$\hat{H}_{\mathrm{dd}} = \frac{1}{4\pi\epsilon_0} \frac{1}{R_{ij}^3} \left(\vec{s}_i \vec{s}_j - \frac{3}{R_{ij}^2} (\vec{s}_i \vec{R}_{ij})(\vec{s}_j \vec{R}_{ij}) \right), \qquad (1.50)$$

and the spin-orbit-interaction:

$$\hat{H}_{LS} = -\lambda_{LS} \vec{L}_i \vec{S}_i = -\frac{e}{2m_e^2 c^2} \left(\frac{1}{R} \frac{d\varphi}{dR} \vec{L}_i \vec{S}_i \right), \qquad (1.51)$$

where ϵ_0 is the permeability constant, λ_{LS} is the spin-orbit-coupling constant, m_e the electron mass, c the velocity of light and φ the coulomb-potential, which the spin experiences. $\vec{L}_i$ and $\vec{S}_i$ are the angular momentum and the spin momentum, respectively. Both interactions couple the spin orientation $\vec{S}$ with the crystal orientation of the lattice $\vec{R}$. Therefore the strength of the interactions depends on the position of the spins with respect to the lattice which leads to the magnetic anisotropy.

No complete theoretical description of the magnetic anisotropy is available today, but it is possible to give a phenomenological description with only a few parameters using simple symmetry considerations. The magnetic anisotropy strongly influences the shape of the free energy density, whose minima determine the orientation of the magnetization. Therefore, the symmetry of the anisotropy has to be found in the symmetry of the free energy. There are two contributions to the magnetic anisotropy [22], the magnetocrystalline anisotropy which is caused by the symmetry of the crystal lattice and the uniaxial anisotropy, which has its origin in external influences, such as effects of strain or crystal surface.

For example, in the case of a cubic crystal one defines α_x, α_y and α_z as the cosines of the angles between the magnetization $\vec{M}$ and the $\langle 001 \rangle$ equivalent crystal axes, i.e. $\alpha_i = M_i/M$ and combines them in a way to achieve the corresponding cubic or uniaxial symmetry. From symmetry considerations the expression for the cubic anisotropy must be an even power of each α_i, providing that opposite ends of the crystals are magnetically equivalent, and it must be invariant under interchanges of the α_i among each other. The first possible combinations which satisfy these symmetry conditions, $\alpha_x^2 + \alpha_y^2 + \alpha_z^2$, does not alter the free energy. Therefore the cubic anisotropy does not provide any contribution until the fourth order. Usually the sixth order is also considered and higher orders can be neglected. That is why the contribution of cubic anisotropy to the free energy can be written as [23, 22]:

$$F_{\mathrm{cubic}} = K_1 V(\alpha_x^2 \alpha_y^2 + \alpha_y^2 \alpha_z^2 + \alpha_z^2 \alpha_x^2) + K_2 V \alpha_x^2 \alpha_y^2 \alpha_z^2, \qquad (1.52)$$
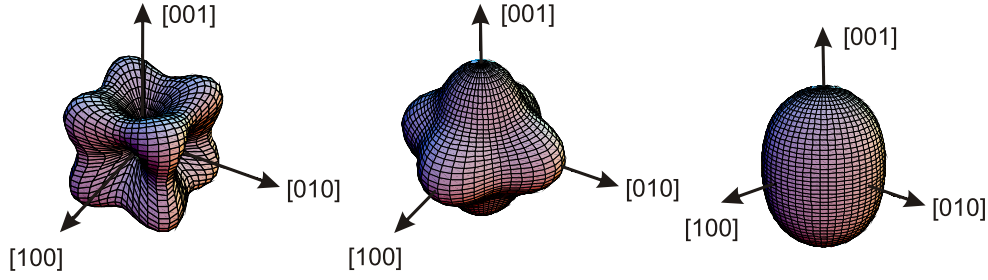
Figure 1.8: Representation of the free energy surface for positive cubic (left) and negative cubic (middle) anisotropy, where the $\langle 001 \rangle$-axes are easy and hard magnetic axes, respectively. The right representation shows the free energy surface for an uniaxial anisotropy in [001]-direction.

with the anisotropy constants K_1, K_2 and the unit volume V. The contribution of the cubic anisotropy to the free energy is shown in figure 1.8. The left representation in figure 1.8 shows the surface of the free energy with a positive cubic anisotropy ($K_1 > 0$), while in the middle the free energy surface with a negative cubic anisotropy ($K_1 < 0$) is shown. In both representations the constant K_2 was set to zero. One can see, that for positive cubic anisotropy the free energy surface shows minima along the cubic main axis, i.e. they are magnetic easy axes, while for negative cubic anisotropy these axes are magnetic hard axes, where the free energy surface exhibits maxima.

For the uniaxial anisotropy the contribution to the free energy is given by [22]:

$$F_{\mathrm{u}} = K_{\mathrm{u}} V (\vec{e}_{\mathrm{M}} \vec{\alpha})^2, \tag{1.53}$$

where K_{u} is the uniaxial anisotropy constant and $\vec{e}_{\mathrm{M}}$ is the unit vector for the hard magnetic axis. Figure 1.8 shows the surface of the free energy for a sample with an uniaxial anisotropy along the [001]-direction.

1.2.2 Domain structure

At temperatures well below the Curie-temperature, a ferromagnetic specimen normaly appears to be "unmagnetized", but can easily be magnetized by exposing it to an external magnetic field. Again the reason for this behaviour is the long ranged dipole-dipole interaction, which leads to a high magnetic dipolar energy for a specimen with a uniform magnetization, where all spins are pointing in the same direction. The energy can be reduced by dividing the specimen into macroscopic, uniformly magnetized domains, whose magnetizations point in different directions as shown schematically in figure 1.9, so that the magnetic moment of the whole specimen nearly vanishes. But the formation of domains does not only lead to a gain in energy. The spins at the boundaries of the domains have to pay exchange energy penalty due to their local non-equilibrium alignment with respect to their neighbour spins. However, the exchange interaction is a short-range interaction and therefore only the spins near the domain
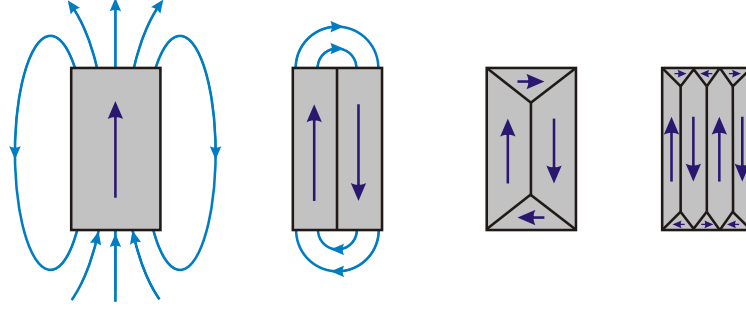
Figure 1.9: A single ferromagnetic specimen has a large magnetic dipolar en-
ergy. By the formation of domains the dipolar energy can drastically
be reduced.

boundaries are affected. On the other hand, the long-range character of the
dipole-dipole interaction leads to a decrease in energy of every spin, if magnetic
domains are formed. Therefore, as long as the domains are not to small, the
domain formation is favored.

In order to reduce the exchange energy per spin at the domain boundaries,
domain walls are formed, where the reversal of the spin orientation is distributed
over many spins. If the spin reversal of 180° between to domains is distributed
over n spins, then each spin will be rotated by π/n with respect to its neigbour
spin. In a classical picture the difference in exchange energy per pair ΔE_{ex} is
then given by:

$$\Delta E_{\text{ex}} = -J_{\text{eff}}S^2 + J_{\text{eff}}S^2 \cos\left(\frac{\pi}{n}\right) \approx -J_{\text{eff}}S^2\frac{\pi^2}{2n^2}, \qquad (1.54)$$

where S is the spin quantum number, J_{eff} is the exchange integral and using
the relation $\cos(\phi) \approx 1 - \frac{1}{2}\phi^2$ for small angles ϕ. The exchange energy between
neighboured spins is therefore lowest, if an infinite number of spins is involved
in forming the domain wall and the wall thickness would be infinite.
The reason for a finite wall thickness is the anisotropy energy. While the magne-
tization in the domains is oriented along the magnetic easy axes, the orientation
of the spins forming the domain wall have to differ from the axes of easy mag-
netization. This increases the anisotropy energy, which is roughly proportional
to the wall thickness.

In order to estimate the domain wall thickness the energy per unit area of the
wall, which is the sum of the contributions from the exchange and the anisotropy
energy, has to be minimized with respect to n. For each line of $n + 1$ spins the
exchange energy per unit area $1/a^2$, where a is the lattice constant, is given by
[24]:

$$\sigma_{\text{ex}} = \frac{E_{\text{ex}}}{a^2} = n\frac{\Delta E_{\text{ex}}}{a^2} = -J_{\text{eff}}S^2\frac{\pi^2}{2na^2}, \qquad (1.55)$$

while the anisotropy energy per unit area is the corresponding anisotropy con-
stant K times the wall thickness na [24]:

$$\sigma_{\text{ani}} = \frac{E_{\text{ani}}}{a^2} \approx Kna. \qquad (1.56)$$
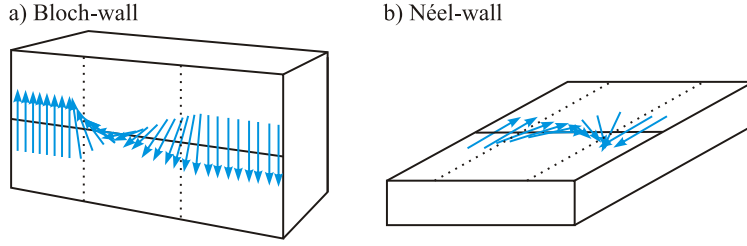
Figure 1.10: Schematical illustration of a) a Bloch-wall and b) a Néel-wall.

The minimum of the sum of the energies with respect to n is then given by:

$$\frac{\partial(\sigma_\text{ex} + \sigma_\text{ani})}{\partial n} = 0 = J_\text{eff} S^2 \frac{\pi^2}{2n^2 a^2} + K a \qquad (1.57)$$

and therefore:

$$n = \sqrt{-J_\text{eff} S^2 \frac{\pi^2}{2Ka^3}}. \qquad (1.58)$$

One distinguishes between two different kinds of domain walls, the Bloch-wall and the Néel-wall, which are shown schematically in figure 1.10. In the case of the Bloch-wall (figure 1.10 a)) the spins are rotated in the plane parallel to the wall, while for the Néel-wall the rotations takes place perpendicular to the domain wall (figure 1.10 b)). In thin ferromagnetic films the formation of Néel-walls is therefore prefered, mainly because a large amount of energy is needed in order to rotate the spins out of the film.

1.3 Magnetoresistance effects

Applying a magnetic field to a solid not only acts on the spin orientation of the electrons or the magnetic moments but also strongly influences the electron motion and therefore the electronic transport properties. For example measuring the resistivity of a solid in an external magnetic field, one observes a change of the resistivity as a function of external field. This effect is called magnetoresistance effect and occurs in magnetic as well as in non-magnetic materials. For comparing the magnetoresistance effects of different materials one may define the relative magnetoresistance ρ_MR, which is given by the difference between the resistivity with and without a magnetic field, normalized to the resistivity without a magnetic field:

$$\rho_\text{MR} = \frac{\rho(B,T) - \rho(0,T)}{\rho(0,T)}. \qquad (1.59)$$

Depending on the material system, one observes different magnetoresistance effects which result in a positive or in a negative magnetoresistance. In non-magnetic metals usually a positive magnetoresistance occurs, while in ferromagnetic metals the alignment of the spins results in a negative magnetoresistance.

The existence of magnetic moments in materials can therefore strongly influence the transport properties.

In the following a short phenomenological description of different magnetoresistance effects is given.

1.3.1 Ordinary magnetoresistance

All non-magnetic metals show a positive magnetoresistance effect, the so-called ordinary magnetoresistance (OMR). The reason for this effect is the Lorentz force,

$$\vec{F}_{\mathrm{L}} = -e\vec{v} \times \vec{B}, \tag{1.60}$$

which acts on the electrons due to the magnetic field. The Lorentz force influences the electron motion and forces the electrons onto circular orbits between two scattering events. For example scattering can occur with defects, impurities or phonons, which decreases the mean free path length and therefore increases the resistivity.

The OMR can not be described within the Drude model [25, 26], where the electrons are treated as free particles, which are accelerated in an electrical field $\vec{E}$ until they collide with a scattering center. For the equation of motion in this model follows:

$$m\frac{d^2\vec{r}}{dt^2} + \frac{m_{\mathrm{e}}}{\tau}\frac{d\vec{r}}{dt} = (-e)\vec{E}, \tag{1.61}$$

where the so-called relaxation time τ is the mean free time between two scattering events. Due to the collisions the electron system reaches an equilibrium state where the electrons posses a mean velocity $\vec{v}_{\mathrm{d}}$, the drift velocity. The current density $\vec{j}$ is then given by:

$$\vec{j} = -ne\vec{v}_{\mathrm{d}}, \tag{1.62}$$

where n is the electron density of the solid. In dynamic equilibrium the drift velocity can be calculated from equation 1.61:

$$\vec{v}_{\mathrm{d}} = -\frac{e\tau}{m_{\mathrm{e}}}\vec{E} = -\mu\vec{E}, \tag{1.63}$$

with the mobility $\mu = \frac{|e|\tau}{m_{\mathrm{e}}}$. Combining equation 1.62 and 1.63 for the current density one obtains:

$$\vec{j} = \left(\frac{ne^2\tau}{m_{\mathrm{e}}}\right)\vec{E} = \sigma\vec{E} = \frac{1}{\rho}\vec{E}. \tag{1.64}$$

This expression is known as Ohm´s law with $\sigma = (ne^2\tau/m_{\mathrm{e}})$ and $\rho = 1/\sigma$ as the the electric conductivity and the resistivity, respectively.

Applying an additional external magnetic field in z-direction ($\vec{B} = B_z\vec{e}_z$) to a sample where the current is applied in x-direction, the Lorentz force leads to a deflection of the electrons in y-direction resulting in a build-up of a transversel electric field E_{H} perpendicular to the current direction. This field is the so-called Hall-field after E. H. Hall, who discovered this phenomenon in 1879 [27].

In equilibrium the Hall-field compensates the influence of the magnetic field and the electrons only move along the x-direction. Solving the equation of motion one obtains for isotropic crystal properties the resisitivity tensor $\boldsymbol{\rho}$:

$$\vec{E} = \boldsymbol{\rho}(B)\vec{j} \tag{1.65}$$

with

$$\boldsymbol{\rho}(B) = \frac{1}{\sigma_0} \begin{pmatrix} 1 & \omega_c\tau & 0 \\ -\omega_c\tau & 1 & 0 \\ 0 & 0 & 1 \end{pmatrix}. \tag{1.66}$$

Here $\sigma_0 = ne^2\tau/m_e$ is the conductivity of the Drude model and $\omega_c = eB_z/m_e$ is the angular frequency of the electron on its circular orbit, the so-called cyclotron frequency. Inverting the tensor $\boldsymbol{\rho}$ yields the conductivity tensor $\boldsymbol{\sigma}$:

$$\boldsymbol{\sigma}(B) = \frac{\sigma_0}{1 + \omega_c^2\tau^2} \begin{pmatrix} 1 & -\omega_c\tau & 0 \\ \omega_c\tau & 1 & 0 \\ 0 & 0 & 1 + \omega_c^2\tau^2 \end{pmatrix}. \tag{1.67}$$

Because of the Hall-field parallel to the y-direction, the current density in this direction vanishes at equilbrium ($j_y = 0$) and the Hall-field can be determined using:

$$E_H = E_y = -\left(\frac{\omega_c\tau}{\sigma_0}\right)j_x = -\left(\frac{B_z}{ne}\right)j_x = R_H B_z j_x, \tag{1.68}$$

where $R_H = -1/ne$ is the Hall-coefficient, which is independent of the specific material parameters and only depends on the carrier density and the charge of the carriers. For the magnetoresistance follows:

$$\rho_{xx}(B) = \frac{1}{\sigma_0}. \tag{1.69}$$

Therefore in the Drude model the resistivity does not depend on the external magnetic field.

The simplest possibility to extend the Drude-model in order to describe the ordinary magnetoresistance effect is to assume two different kinds of carriers, e.g. electrons and holes in semiconductors but also s and p electrons in metals. In general both kinds of carriers have different effective masses m_i^*, different relaxation times τ_i and eventually different charges q_i. In an electric field the effective current density j_{tot} is given by the sum of the current densities of the two different kinds of carriers:

$$\vec{j}_{\text{tot}} = \vec{j}_1 + \vec{j}_2 = \boldsymbol{\sigma}_1(B)\vec{E} + \boldsymbol{\sigma}_2(B)\vec{E}. \tag{1.70}$$

For the magnetoresistance follows:

$$\rho_{xx}(B) = \frac{\sigma_1\left(1 + \omega_{c2}^2\tau_2^2\right) + \sigma_2\left(1 + \omega_{c1}^2\tau_1^2\right)}{(\sigma_1 + \sigma_2)^2 + (\sigma_1\omega_{c2}\tau_2 + \sigma_2\omega_{c1}\tau_1)^2}, \tag{1.71}$$

with $\sigma_i = n_i q_i^2 \tau_i / m_i^*$ and the relative change of the magnetoresistance in an external magnetic field is given by [28]:

$$\rho_{\mathrm{MR}} = \frac{\rho_{xx}(B) - \rho_{xx}(0)}{\rho_{xx}(0)} = \frac{\sigma_1 \sigma_2 \left(\frac{q_1 \tau_1}{m_1^*} - \frac{q_2 \tau_2}{m_2^*} \right)^2 B_z^2}{(\sigma_1 + \sigma_2)^2 + \left(\frac{q_1 \tau_1}{m_1^*} \sigma_1 + \frac{q_2 \tau_2}{m_2^*} \sigma_2 \right)^2 B_z^2}. \tag{1.72}$$

The relative magnetoresistance therefore only vanishes for $\omega_{c1} \tau_1 = \omega_{c2} \tau_2$, i.e. when only one type of carriers is responsible for the transport. Otherwise, one finds a quadratic behaviour of the magnetoresistance at small magnetic fields, which can be observed for example in non-magnetic metals like gold and copper [29], and a saturation of the magnetoresistance at high fields. This behaviour is known as ordinary magnetoresistance. The OMR occurs in every material system, but in many cases the OMR is dominated by much larger MR effects of a different origin.

1.3.2 Extraordinary magnetoresistance

A second positive magnetoresistance effect, which dominates the transport behaviour in metal-semiconductor hybrid structures, is the extraordinary magnetoresistance (EMR). It was first described in 1963 by H. Weiß and M. Wilhelm in the high-mobility semiconductor InSb with metallic NiAs inclusions [30] and shows a quadratic magnetic field dependence, which can reach values up to 150000% at 1 T in the hybrid system InSb/Au [31].

The basic idea to explain this large magnetoresistance effect is shown in figure 1.11. If the conductivity difference between the metal and the semiconductor is large, the local electric field is always perpendicular to the equipotential surface of the highly conductive inclusion. Therefore, without a magnetic field the current flows directly into the metal inhomogeneity, which acts as a short circuit [32] as shown in figure 1.11 a).

At finite magnetic field applied in z-direction, the carriers are deflected by the Lorentz force, which results in a Hall-field perpendicular to the current direction. The resulting total electric field, consisting of the applied electric field E_x
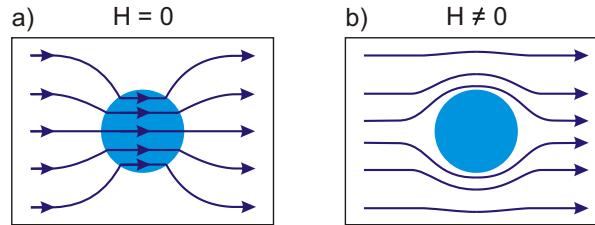

Figure 1.11: Schematic explanation of the extraordinary effect. a) Without a magnetic field the metallic inclusions in a metal-semiconductor hybrid structure act as a short circuit. b) For large magnetic fields the current is deflected around the inclusions, which leads to an increase of the resistivity.

and the Hall-field E_H, is rotated with respect to the current direction by the so-called Hall-angle, which is given by [33]:

$$\tan(\theta_\mathrm{H}) = \frac{E_\mathrm{H}}{E_x} = \frac{R_\mathrm{H} B_z}{\rho_{xx}} = \mu B_z. \tag{1.73}$$

At high magnetic fields and for a high carrier mobility of the semiconductor the Hall-angle between the total electric field and the current direction reaches 90° and the Hall-field is oriented perpendicular to the equipotential surface of the metallic inclusion. In this case the current density is deflected around the inhomogeneities, which leads to a current path parallel to the surface of the metallic inclusion, as shown in figure 1.11 b). The metallic inclusion acts then as a open circuit [32].

The transition of the metallic inclusion from a short circuit, where the current path leads through the high conductive metal, to a open circuit, where the current path goes through the lower conducting semiconductor, leads to the extraordinary magnetoresistance.

1.3.3 Large linear magnetoresistance

A very unusual positive magnetoresistance effect, which is recently strongly under investigation, can be observed in silver-rich silver chalcogenides, like $\mathrm{Ag}_{2+\delta}\mathrm{Se}$ and $\mathrm{Ag}_{2+\delta}\mathrm{Te}$ [34, 35]. While for many semiconductors or metals a ordinary magnetoresistance is observed, which saturates at high fields, the silver chalcogenides exhibit over the temperature range from 4 K to 300 K an enormously large and linear magnetoresistance effect, which is observable from low magnetic fields of a few mT up to extremely high fields of 55 T [36]. Additionally the unusual magnetoresistance behaviour only occurs in heterogeneous samples, where small silver clusters and precipitates are embedded in the material system, while homogeneous samples show the known OMR [37, 34].

Until now the origin of this linear behaviour is not clear. However, because the silver-rich silver chalcogenides are granular structures and the two-phase character of the material strongly influences the observed MR effects, a proposed explanation is, that the large linear MR arises from macroscopic inhomogeneities of the samples. In order to describe this behaviour, different theoretical models have been developed, where the inhomogeneities are modelled in various ways, e.g. with spatially varying conductivities in a macroscopically disordered semiconductor [36, 38], or with compact inclusions of different size and form, which possess other transport properties than the surrounding material [39, 40].

In all theoretical descriptions the large linear magnetoresistance effect results from the inhomogeneity of the material system and is given by [38]:

$$\rho_\mathrm{LLMR} = \bar{\rho}_0 \left(\sqrt{1 + (\bar{\mu}B)^2} \right), \tag{1.74}$$

where $\bar{\rho}_0$ and $\bar{\mu}$ are the mean resistivity and the mean mobility of the material system, respectively.

1.3.4 Anisotropic magnetoresistance

In 1857 William Thompson measured the resistivity of the ferromagnetic metals iron and nickel and observed that the resistivity is largest, when the external magnetic field is applied parallel to the current direction and lowest for a field orientation perpendicular to the current direction [41]. This effect is known as anisotropic magnetoresistance (AMR), which is characteristic for ferromagnets. At low magnetic fields the anisotropic magnetoresistance results from the anisotropy of the resistivity of the ferromagnet, i.e. the resistivity depends on the relative orientation between the magnetization $\vec{M}$ and the current density $\vec{j}$. With increasing field the anisotropic magnetoresistance follows the magnetization orientation due to the alignment of the domains and saturates, as soon as the magnetization is oriented parallel to the magnetic field. The saturation value thereby depends on the relative orientation between the current density and the magnetic field. For fields larger than the saturation value $\vec{B}_{\mathrm{s}}$, one observes the ordinary magnetoresistance.

The origin of the anisotropy of the resistivity in ferromagnets is the spin-orbit coupling, which leads to a non-spherical charge distribution of the d orbitals which cause the magnetic moments. Because this asymmetry is connected with the orientation of the spin, a rotation of the spin direction also leads to a rotation of the charge distribution. The anisotropy of the resistance therefore reflects the anisotropy of the wavefunctions of the d electrons [42, 43]. Due to the non-spherical charge distribution the conduction electrons experience different scattering cross sections for a magnetization oriented parallel or perpendicular to the current direction, which leads to the observed anisotropic magnetoresistance.

From simple symmetry considerations one finds for isotropic materials, that the magnetoresistance of a single ferromagnetic domain can be described by [44]:

$$\rho \;=\; \rho_\perp + (\rho_\parallel - \rho_\perp)\cos^2(\theta_{\mathrm{M}}). \tag{1.75}$$

Here $\rho_\perp$ and $\rho_\parallel$ are the values of the resistivity when the current density is perpendicular and parallel to the magnetization direction, respectively, and θ_{M} is the angle between current density $\vec{j}$ and magnetization $\vec{M}$. Without magnetic field the magnetization of the domains in bulk material is distributed randomly. The mean value of $\cos^2(\theta)$ is then given by $1/3$ and therefore the resistivity can be written as [44]:

$$\rho = \frac{\rho_\parallel + 2\rho_\perp}{3} + (\rho_\parallel - \rho_\perp)\left(\cos^2(\theta_{\mathrm{M}}) - \frac{1}{3}\right). \tag{1.76}$$

The difference $(\rho_\parallel - \rho_\perp)$ is called spontaneous resistivity anisotropy and $\bar{\rho} = (\rho_\parallel + 2\rho_\perp)/3$ is the average resistivity. For the anisotropic magnetoresistance follows [43]:

$$\rho_{\mathrm{AMR}} = \frac{\rho(B_S) - \bar{\rho}}{\bar{\rho}} = \frac{(\rho_\parallel - \rho_\perp)}{\bar{\rho}}\left(\cos^2(\theta_{\mathrm{M}}) - \frac{1}{3}\right). \tag{1.77}$$
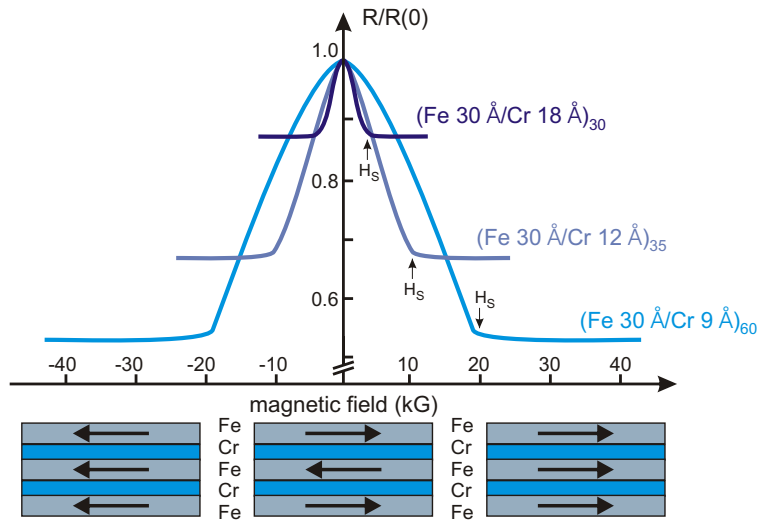
Figure 1.12: Giant magnetoresistance of Fe/Cr superlattices at 4.2 K. The resistivity is largest for an antiparallel alignment of the ferromagnetic layers and a Cr layer thickness of 0.9 nm (after [4]).

In general, the resistivity for the current parallel to the magnetization is higher than for the current perpendicular to the magnetization (i.e. $\rho_\parallel > \rho_\perp$), but sometimes also the opposite situation is found [45].

1.3.5 Giant magnetoresistance

Not only in bulk materials but also in layered structures consisting of alternating magnetic and non-magnetic layers, the magnetic materials strongly influence the properties of the system. For example in 1986 Peter Grünberg discovered, that a multilayer consisting of Fe/Cr-layers shows a antiferromagnetic coupling between two neighbouring iron layers, if the separating chrom-layer has a thickness of 1 nm [5]. The reason for this behaviour is an indirect exchange interaction, which leads to a ferromagnetic or antiferromagnetic coupling between the magnetic layers depending on the thickness of the non-magnetic layer between them [46].

The electrical transport through such layered structures strongly depends on the relative orientation of the magnetization of the ferromagnetic layers. If one aligns the antiferromagnetically coupled magnetizations of a layer structure parallel by applying an external magnetic field, one observes a decrease of the resistivity of the structure [4, 47], which is shown in figure 1.12. This effect is known as giant magnetoresistance effect (GMR) because the change in the resistivity is very large, up to 80% at room temperature [48], and independent of the relative orientation between the current direction and the external magnetic field.

The GMR effect is defined as the difference in the resistivity between parallel and antiparallel alignment of the magnetization, $\rho_{\uparrow\uparrow}$ and $\rho_{\uparrow\downarrow}$, respectively,

normalized to the resistivity for a parallel alignment [49]:

$$\rho_{\mathrm{GMR}} = \frac{\rho_{\uparrow\downarrow} - \rho_{\uparrow\uparrow}}{\rho_{\uparrow\uparrow}}. \tag{1.78}$$

In a simple model the GMR can be understood by assuming different scattering rates of the carriers for a parallel and an antiparallel alignment of the carrier spin and the magnetization orientation of the magnetic layer. In transition metals mainly the $4s$ electrons are responsible for the transport due to their lower effective masses compared to the $3d$ electrons. Additionally the scattering time strongly depends on the density of states. A large density of states of the $3d$ electrons at the Fermi level leads to a strong scattering of the $4s$ electrons into the $3d$ states and therefore to a high scattering rate and a large resistivity. Because the $3d$ density of states in the ferromagnetic layer is split due to the exchange interaction, a certain spin orientation experiences different scattering rates for different magnetization orientations as long as the spin is conserved during the scattering process. If the magnetic layers are aligned parallel, one spin orientation experiences only low scattering rates in all ferromagnetic layers due to the small $3d$ density of states at the Fermi level. Therefore a parallel alignment results in a decrease of the resistivity of the multilayer structure compared to an antiparallel alignment, which is shown schematically in figure 1.13.

The giant magnetoresistance cannot only be observed in layered multistructures, but also in granular hybrid structures, where ferromagnetic particles are embedded in a non-magnetic matrix [7, 50]. Without a magnetic field the magnetization orientation of the single-domain particles is distributed randomly, but can be oriented parallel in an external magnetic field. The resulting GMR depends on the magnetization orientation of the particles, the particle size and their density in the non-magnetic matrix. Because of the random distribution of the particle magnetization in zero field, the giant magnetoresistance which can be achieved in such structures is in general only half as large as in layered systems, where the magnetic field switches from an antiparallel to a parallel configuration.

1.3.6 Tunnel magnetoresistance

A second magnetoresistance effect, which occurs in structures consisting of magnetic layers, is the tunnel magnetoresistance (TMR), which was first observed in a Fe/Ge/Co-junction at $4.2\,\mathrm{K}$ by M. Jullière in 1975 [6]. Such a TMR-structure consists of two magnetic layers, but in contrast to the GMR-structure, a thin insulating layer instead of a non-magnetic one is used to separate the ferromagnetic layers, which hinders a magnetic coupling between them and leads to a tunneling of the electrons through the insulating barrier. Like in a GMR-multilayer, the resulting tunnel current depends on the relative orientation of the two magnetic layers, i.e. a high resistivity of the structure is obtained for an antiparallel and a low resistivity for a parallel alignment. In order to
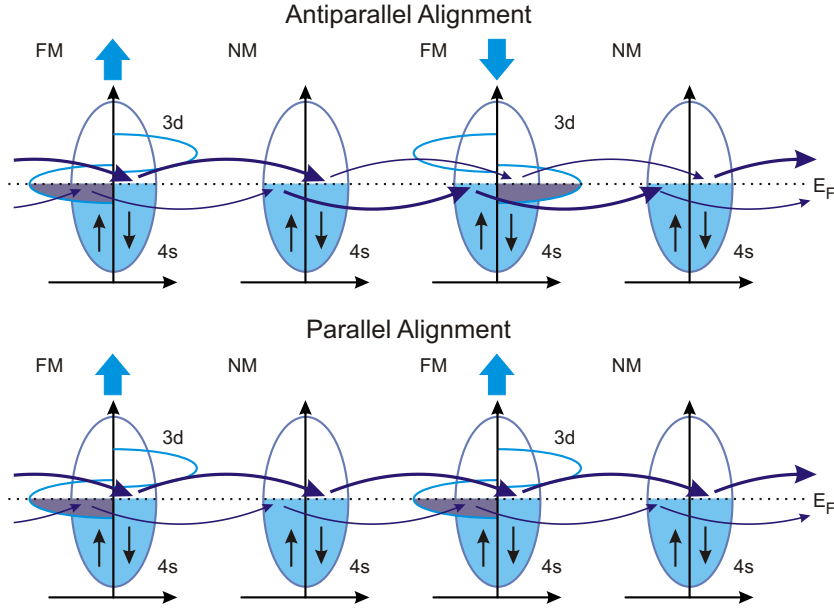
Figure 1.13: Schematic view of the bandstructure of a GMR-multistructure consisting of magnetic and non-magnetic layers for an antiparallel (top) and a parallel alignment (bottom) of the layer magnetization. Due to the exchange interaction the $3d$ density of states is splitted. A large $3d$ density of states at the Fermi level E_F leads to high scattering rates and therefore to a small current (thin arrows) for the respective spin orientation, while a small $3d$ density of states results in a large current (thick arrows).

achieve an antiparallel alignment even without a coupling between the layers one uses ferromagnetic layers which have a common easy axis, but different coercitivities. Therefore the two layers can be oriented antiparallel by applying a magnetic field with a field strength chosen between the two coercive fields, while for higher or lower field strengths a parallel alignment is obtained.

As the GMR effect, the TMR effect is defined as the difference in the resistivity between parallel and antiparallel alignment of the magnetization normalized to the resistivity for a parallel alignment:

$$\rho_{\mathrm{TMR}} = \frac{\rho_{\uparrow\downarrow} - \rho_{\uparrow\uparrow}}{\rho_{\uparrow\uparrow}}. \tag{1.79}$$

The simplest model to explain the TMR-effect is based on the assumptions, that the two magnetic layers are completely isolated by the insulating barrier [6] and that the tunnel current between the two ferromagnetic metals is proportional to the product of the density of states at the Fermi energy of the two metals on either side of the insulator [51]. Because the tunnel current in a TMR-structure is predominantly carried by the d electrons [52] and almost no spin-flip tunneling occurs [51] a large tunnel current is obtained if for one spin orientation a large $3d$ density of states is available in both ferromagnetic layers. This is the case for a parallel alignment of the two magnetic layers as schemat-
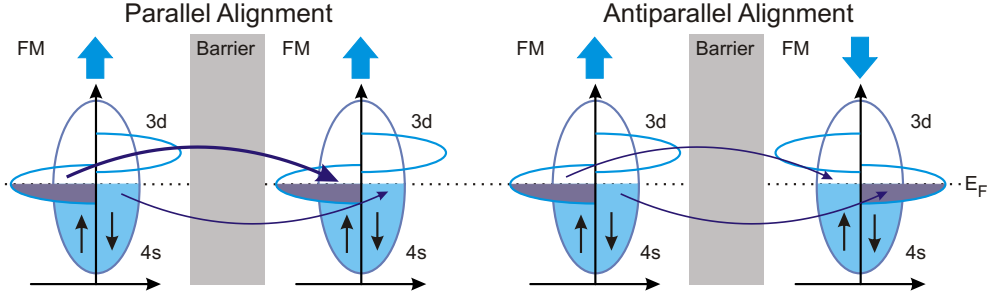
Figure 1.14: Schematic view of the band structure of a TMR-junction. Because
            the tunnel current is proportional to the $3d$ density of states of both
            magnetic layers, a large tunnel current (thick arrow) for one spin
            orientation is obtained for a ferromagnetic alignment (left). For an
            antiparallel alignment only a low tunnel current (thin arrow) can
            be found for both spin orientations (right).

ically shown in figure 1.14. For an antiparallel alignment one spin orientation
experiences only a low $3d$ density of states in one of the ferromagnetic layers
due to the band splitting caused by the exchange energy, and therefore only a
low tunnel current is obtained, which leads to a high resistivity.

The magnitude of the TMR effect therefore strongly depends on the difference
in the density of states of the two spin orientations. For TMR-structures con-
sisting of transition metals or alloys, e.g. Co or Ni, TMR effects of 50 % at
room temperature can be achieved. For a tunnel structure consisting of two
amorphous CoFeB ferromagnetic layers separated by an insulating MgO barrier,
even a TMR effect up to 230 % is obtained at room temperature [53].

2 Self-assembled growth of MnAs clusters on (111)B substrates by MOVPE

Conventional granular GaMnAs/MnAs hybrid structures are prepared either by Mn-ion implantation into GaAs followed by thermal annealing [54, 55], by thermal annealing of $Ga_{1-x}Mn_xAs$ alloys grown by molecular beam epitaxy (MBE) with a Mn content x of a few percent [56, 57, 58], or by standard metal-organic vapour phase epitaxy (MOVPE) [59, 60]. In the first two cases the annealing of the samples at temperatures above the growth temperature leads to the formation of MnAs clusters in the GaMnAs matrix, while in the third case the clusters form self-assembled during the growth due to the lower solubility of Mn in GaAs at higher growth temperatures [61]. All three preparation methods result in random cluster distributions in the sample, which hinders a technological utilization of the hybrid structures as nanoelectronic devices. In order to overcome this problem, it is necessary to position the clusters in a controlled way, which can be done by the new method of self-assembled MOVPE growth on pre-patterned substrates.

In this chapter the sample preparation and the growth conditions for the investigated samples are described, which were grown at the Research Center for Integrated Quantum Electronics (RCIQE) of the Hokkaido Universtity in Sapporo, Japan, in the group of Prof. Dr. Shinjiroh Hara. The first part gives a short overview of the basic principles of the MOVPE growth, while the second part describes in detail the growth procedure for the investigated samples and the investigation of the quality of the clusters after the growth by scanning electron microsopy (SEM).

2.1 Basic principles of metal-organic vapour phase epitaxy

Metal-organic vapour phase epitaxy (MOVPE), also known as metal-organic chemical vapour deposition (MOCVD) or organo-metallic vapour phase epitaxy (OMVPE), is a low-pressure up to atmospheric pressure growth technique. It was invented in 1969 by H. M. Manasevit and W. I. Simpson [62] and is nowadays a wide-spread and well developed technique in order to grow high quality semiconductors as crystalline thin films. The basic principle of MOVPE is,

N₂ H₂

purifier

pressure controller

massflow controller

valve: normally closed

valve: normally open

reactor

sample

mixing chamber

susceptor

vent line

scrubber

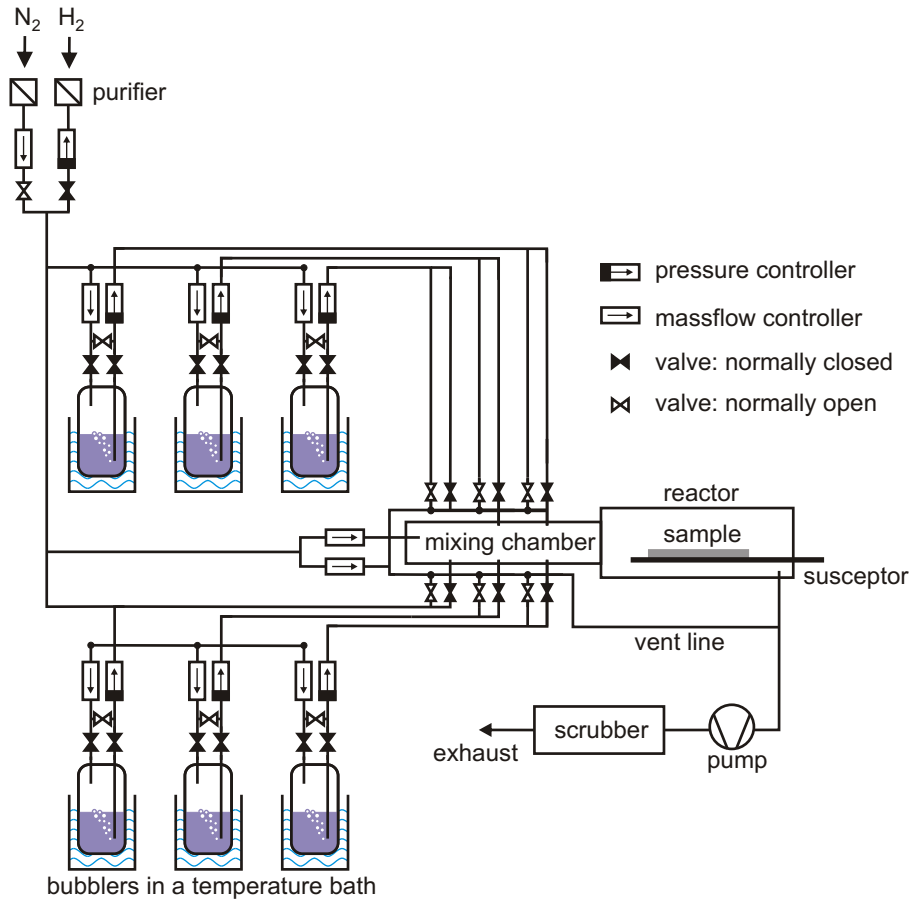exhaust

pump

bubblers in a temperature bath

Figure 2.1: Sketch of a MOVPE reactor system. The flow of the carrier gas through the bubblers is controlled by pressure and massflow controllers and guided to the mixing chamber and the reactor. The sample in the reactor is located on a susceptor which is heated up to the growth temperature. The scrubber eliminates the residuals of the growth.

that it uses, in contrast to, for example, the molecular beam epitaxy technique, organic-metallic precursors instead of metallic reactants, which are decomposited at high temperatures and deposited on the sample surface.

Figure 2.1 shows a schematic overview of a MOVPE-system. The carrier gas (N₂ or H₂), which is cleaned with a purifier to guarantee high purity, is guided to the metall-organic precursor sources, which are situated in cylinders made of stainless steel. The cylinders are called bubblers, because the carrier gas "bubbles" through the sources, in order to carry the metal-organic precursors in the gas phase to the reactor. Using different valves and controlling the mass flows, the pressures and the temperatures of the sources, which are placed into temperature-controlled baths, it can be controlled whether the carrier gas is guided through a source and how much of the precursor will be carried to the reactor. In the reactor the substrate is located on the so-called susceptor, which
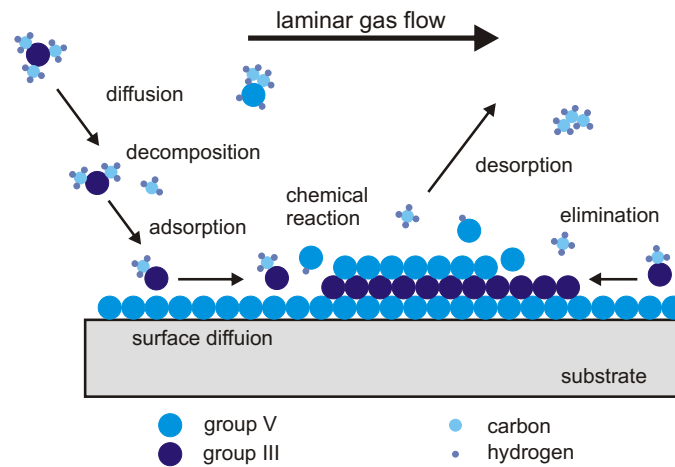
Figure 2.2: Schematic illustration of the MOVPE-growth.

is heated up to a constant growth temperature, typically in the temperature
range from 500°C to 1200°C. The high temperatures in the reactor lead to
serveral gas phase reactions and to the decomposition of the precursors. On
the subtrate surface the reactants are adsorbed and the growth of the crystalline layer is initiated. The organic parts of the precursors, like carbon, are
ideally desorbed and carried away by the carrier gas. This growth process is
schematically shown in figure 2.2. After the reactor and the pump the carrier gas passes a scrubber, which eliminates the residuals of the growth or the
portion of precursors that did not react.

2.2 Self-assembled growth of randomly distributed hexagon-shaped nanoclusters on (111)B GaInAs/InP surfaces

Three samples with self-assembled hexagon-shaped MnAs nanoclusters, which
are randomly distributed on the surface, were grown by MOVPE. For the growth
of these samples, as well as for the growth of the cluster arrangements, which is
discussed in section 2.3, a (111) orientation of the substrate was used because
it is well suited for the self-assembled growth of MnAs nanoclusters on zincblende III-V semiconductors. The reason is, that the c-plane of the hexagonal
MnAs clusters, which crystallize in NiAs-symmetry [63, 64, 9], matches very
well the (111) surface of the substrate as both are of the same symmetry. The
NiAs-structure of the MnAs nanoclusters is shown in figure 2.3.
The growth was performed in several steps [63, 66, 67]. In the first step an
InP buffer layer was grown on an InP(111)B wafer, followed by the growth
of an undoped GaInAs layer. For the growth of the two layers in a horizontal low-pressure MOVPE system, tri-methyl-gallium (TMGa, $(CH_3)_3Ga$), tri-methyl-indium (TMIn, $(CH_3)_3In$), tertiary-butyl-phosphine (TBP, t-$C_4H_9PH_2$)
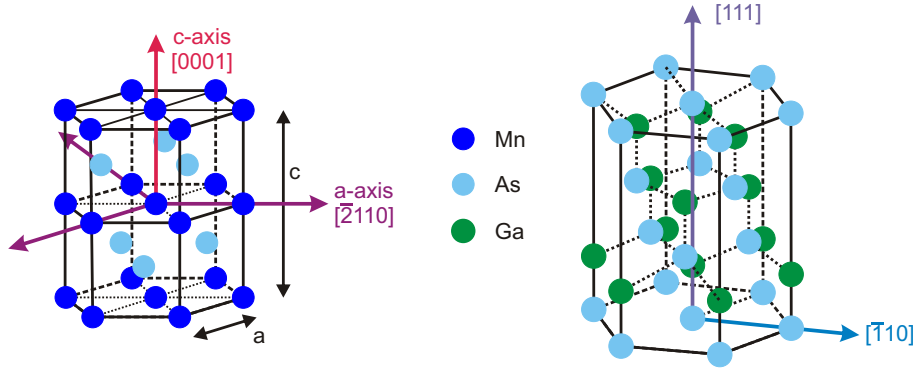
Figure 2.3: Arrangement of hexagonal MnAs in NiAs-crystal structure (left) and of zincblende GaAs in a pseudohexagonal unit cell (right) after Ref. [65]. In MnAs the manganese atoms are positionated in hexagon-shaped planes, which are perpendicular to the c-axis. The same symmetry can be found for the surface of zinc-blende (111)B GaAs.

and 20%-arsine (AsH$_3$) diluted in hydrogen were used as sources for the group III and V materials. The InP layer was grown at a growth temperature (T_G) of 600°C, while for the GaInAs layer the growth temperature was increased to 650°C. The V/III ratio, defined as the partial pressure ratio between the group V and the group III source materials, was 50 for the InP layer and 100 for the GaInAs layer. The estimated partial pressures for the precursors TMIn and TMGa were 3.3×10^{-6} and 2.3×10^{-6} atm, respectively.

For the self-assembled growth of the MnAs nanoclusters, the organometallic precursor Bis(methyl-cyclopentadienyl) manganese, (CH$_3$C$_5$H$_4$)$_2$Mn, was introduced to the reactor with 20%-AsH$_3$ diluted in H$_2$, which posseses compared to other commonly used Mn-precursors a relativ low melting point (ca. 60°C) and reduces the risc of a contamination with oxygen. In order to increase the vapour pressure, the temperature of the (CH$_3$C$_5$H$_4$)$_2$Mn was controlled at 70°C resulting in an estimated vapour pressure of around 0.25 Torr.

The growth of the self-assembled nanoclusters strongly depends on the MOVPE growth conditions [67], such as the growth time, the growth temperature, and the V/Mn-ratio, defined as the ratio of the partial pressures of arsine and (CH$_3$C$_5$H$_4$)$_2$Mn. The series of samples with self-assembled nanoclusters was grown at a constant growth temperature of 650°C and an estimated partial pressure of 1.1×10^{-6} atm for (CH$_3$C$_5$H$_4$)$_2$Mn. The parameters for the growth of the different layers are also listed in table 2.1. The V/Mn-ratio for the three samples was 375, 750 and 1125, which resulted in a random cluster distribution with different cluster densities on the sample surface of 2.83×10^8, 6.18×10^8 and 6.57×10^8 nanoclusters per cm^2, respectively. The cluster densities were determined from atomic force microscopy (AFM) images of the samples surfaces, which are shown in figure 2.4.

As can be seen in the AFM images, the hexagonal nanoclusters were grown self-assembled on the (111)B GaInAs layer, which has a very flat surface with
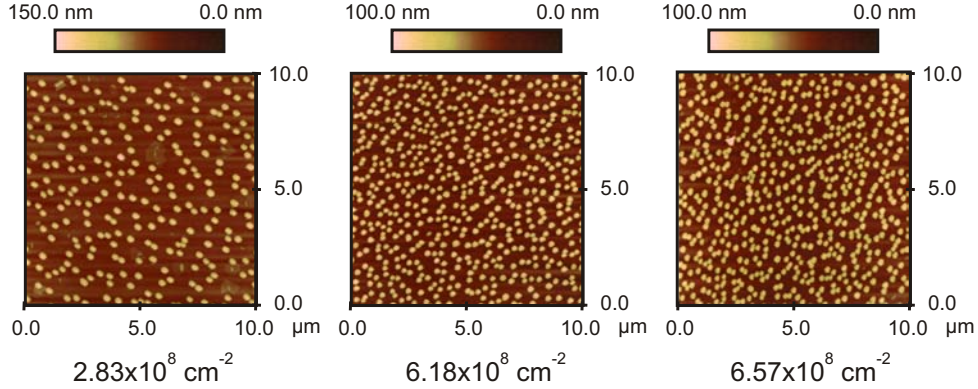
Figure 2.4: Atomic force microscopy (AFM) images of the surface of the three
samples with randomly distributed hexagon-shaped MnAs nano-
clusters. The cluster density increases from left to right from
2.83×10^8 to 6.18×10^8 and finally to 6.57×10^8 nanoclusters per cm^2.

atomic steps and some large terraces. The nanoclusters have a typical diame-
ter of 150 nm and measure about 60-80 nm in height. Hara et al. also showed
by electron beam diffraction patterns, that the nanoclusters have a hexagonal
NiAs-type crystallographic structure with a c-axis parallel to the $[\bar{1}\bar{1}\bar{1}]$-direction
of the zinc-blende-type (111)B GaInAs layer [66].

In order to investigate the randomly distributed clusters in more detail, scanning
electron microscopy (SEM) images of the surfaces of the three samples were
recorded. The results are shown in figure 2.5. For all three samples one can
clearly see the hexagon-shaped nanoclusters, which possess well defined crystal
facets and which were also observed by AFM. Additionally the SEM images
reveal, that for the samples with a cluster density of 2.83×10^8 and 6.18×10^8
nanoclusters per cm^2 additional clusters of ellipsoidal shape are observable,
while for the sample with the highest cluster density of 6.57×10^8 nanoclusters
per cm^2 this type of cluster cannot be found. Instead, some cluster complexes
are visible. The cluster complexes probably arise from two cluster seeds in close

layer	T_{G}	V/III- or V/Mn-ratio	cluster density
InP	600°C	50	
GaInAs	650°C	100	
MnAs I	650°C	375	2.83×10^8 cm^{-2}
MnAs II	650°C	750	6.18×10^8 cm^{-2}
MnAs III	650°C	1125	6.57×10^8 cm^{-2}

Table 2.1: Growth parameters of the three samples with a random distribu-
tion of hexagon-shaped MnAs nanoclusters. Varying the V/Mn-ratio
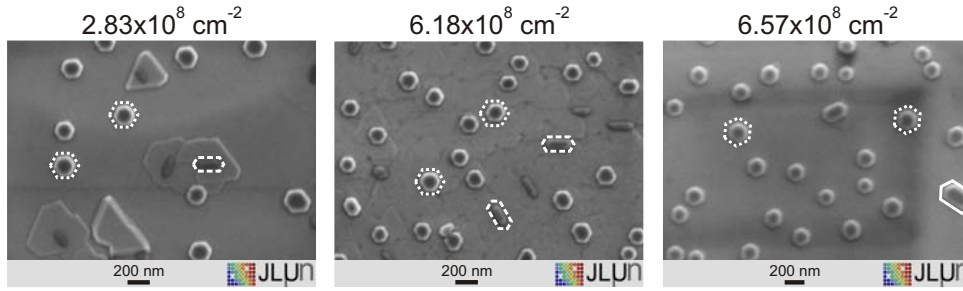leads to different cluster densities on the sample surface.

Figure 2.5: Scanning electron microscopy images (SEM) of the sample surface of the three samples with different densities of randomly distributed, hexagon-shaped MnAs nanoclusters. For all samples hexagon-shaped nanoclusters (dotted line) were found. The sample with the highest cluster density (right) also shows cluster complexes (solid line), while for the other two samples ellipsoidal clusters (dashed line) are observabel.

vicinity, which merge during the growth process of the clusters resulting in one single elongated cluster complex.

2.3 Selective-area growth of MnAs cluster arrangements on pre-patterned (111)B GaAs substrates

As shown in the previous section, it is possible to grow self-assembled hexagon-shaped MnAs nanoclusters with well-defined crystal facets and a high degree of uniformity on (111)B surfaces. Unfortunately the growth process results in a random cluster distribution on the surface of the samples. The new method of selective-area MOVPE growth on pre-patterned substrates allows one to prepare samples with regular cluster arrangements and cluster chains [66, 68, 69].

2.3.1 Pre-patterning of the substrate

Figure 2.6 shows a schematic representation of the fabrication process for the controlled positioning of the nanoclusters. As substrates semi-insulating (111)B GaAs wafers were used, which were covered with an amourphous silicondioxide (SiO$_2$) layer with a thickness of 20-30 nm. The layer was deposited by plasma sputtering. During the sputtering process atoms are ejected from a silicondioxide target due to the bombardment of the target with argon ions. The ejected SiO$_2$-atoms are deposited on to the (111)B GaAs substrate surface. After the deposition of the SiO$_2$-layer on to the substrate, the wafer was cleaved into several pieces each about 3×3 cm^2 in size. These sample pieces were cleaned successively with acetone, ethanol and water in an ultrasonic bath for several minutes in order to remove all dirt from the surface.
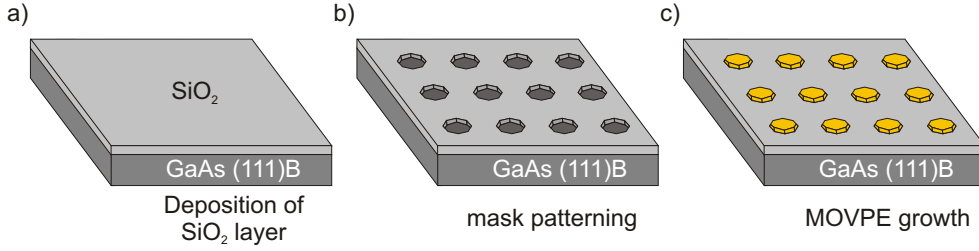
Figure 2.6: Fabrication process for the selective-area growth of MnAs nanoclus-
ters. a) An amourphous SiO_2 layer is deposited by plasma sputter-
ing on the (111)B GaAs substrate. b) In a second step the SiO_2
layer is patterned by electron beam lithography and wet-chemical
etching. c) During the MOVPE growth the nanoclusters assemble
in the SiO_2 openings.

For the structuring by electron beam lithography a primer, which guarantees a
good adherence of the resist on the sample surface, and a positive resist were
deposited on the sample using a spin-coater. The spin coater rotated with 500
rotations per minute (rpm) for three seconds followed by 8000 rpm for 30 s.
Two pre-bake steps were carried out. At first the sample was pre-baked in an
oven at 170°C for 2 min followed by a second pre-bake at 90°C for 5 min. After
the pre-bake the desired regular arrangement was transferred into the resist by
electron beam lithography. Finally the resist was developed with xylene for 2
minutes.

After a hard-bake at 140°C for 10 min the pattern was transfered into the SiO_2
layer by wet-chemical etching with buffered hydrofluoric acid (BHF). Etch-
ing solution was a mixture of HF and NH_4F in parts of 1:10 with an etching
rate of around 1.7 nm/s. Finally the remaining resist was removed with NN-
Dimethylacetamide. In the artificial structuring process prior to the MOVPE
growth, the SiO_2-layer is removed selectively at the points, where the MnAs
clusters shall be formed in the self-organised process, i.e. the patterned SiO_2
layer serves as mask for the MnAs growth by MOVPE [66, 68, 69].

Typical SEM images of the resulting pattern after the etching process are shown
in figure 2.7. In the SEM images the SiO_2 layer, which covers the substrate,
looks grey, while the dark region is the (111)B GaAs, where the layer was re-
moved during the etching step. The left image of figure 2.7 shows the complete
pattern of one sample consisting of an array of squares, which are $100 \times 100 \ \mu m^2$
in size. The right image shows a detailed view of such a square, which is struc-
tured with the mask openings, where the single MnAs cluster will be formed in
the growth process. By varying the size and the shape of the openings in the
SiO_2, the size and the shape of the MnAs clusters can be determined.

The large area of uncovered (111)B GaAs substrate between the squares is nec-
essary to accomodate the manganese offered in the growth process which is not
needed for the cluster growth. This leads to a regular growth of the MnAs
nanoclusters in the openings and guarantees, that no manganese is deposited
on the SiO_2 layer between the openings for the single clusters.

2.3.2 Self-assembled growth of the MnAs clusters by MOVPE

Before the actual self-assembled growth of the MnAs nanoclusters again an efficient cleaning of the pre-patterned substrate was carried out. For this purpose the samples were cleaned successively with acetone, water and Semicoclean, a special acid solution in the ultrasonic bath, for 10 min respectively. After introducing the samples into the MOVPE growth reactor, the samples were heated up to 630°C for 5 minutes for thermal cleaning. At first a thin AlGaAs buffer layer was grown at 800°C for 3 minutes. This buffer layer is needed to prevent a diffusion of the manganese into the GaAs substrate, and therefore guarantees a regular growth of the clusters in the openings. Without the AlGaAs layer, no MnAs clusters are formed in some of the openings [68]. For the growth of the AlGaAs buffer layer, tri-methyl-gallium, tri-methyl-aluminium (TMAl, $(CH_3)_3Al$) and as group V material 20%-arsine diluted in H_2 were used as source materials [70] and the V/III-ratio was 343.

For the self-assembled growth of the MnAs nanoclusters, the same source materials as for the growth of the randomly distributed hexagon-shaped nanoclusters were used, i.e. $(CH_3C_5H_4)_2Mn$ and 20%-AsH_3 diluted in H_2. Again the growth temperature as well as the V/Mn-ratio are crucial parameters for the self-assembled growth of MnAs nanoclusters. As Wakatsuki et al. have shown [69], a growth temperature of 750°C leads to a cluster formation not only in the openings, but also on the SiO_2 mask with decreasing cluster densities on the SiO_2 layer for increasing V/Mn-ratios, while no cluster can be found between the openings for a V/Mn-ratio of 1125 and a relatively high growth temperature of 800°C or above. Wakatsuki et al. explained these experimental results with a longer migration length of Mn-As compounds on the SiO_2 mask than that of Mn atoms and/or other Mn compounds. A relatively high V/Mn-ratio, where the Mn-As compounds are formed, results in a decreasing density of unintentionally deposited MnAs on the SiO_2 mask due to the more efficient migration of the Mn-As compounds to the openings. Additionally, at high temperatures the thermally activated migration of Mn-As compounds on the surface is increased, so that at high growth temperatures and a high V/Mn-ratio the deposition of
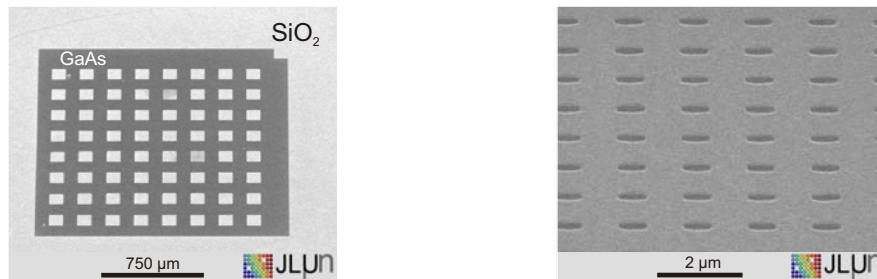

Figure 2.7: SEM images of a typical sample after the patterning of the SiO_2 layer (left). The grey region is the SiO_2, while the dark area is the (111)B GaAs substrate, where the layer was removed. In the grey SiO_2 squares the opening for the MnAs clusters (right) are located.

layer	T_G	V/III- or V/Mn-ratio	Growth time t_G
AlGaAs	800°C	343	3 min
MnAs	825°C	1125	10 min

Table 2.2: Parameters for the growth of the AlGaAs buffer layer and the MnAs
nanoclusters.

residual MnAs on the SiO_2 pattern is avoided.

Therefore, in order to achieve a regular growth of the MnAs only in the SiO_2 openings, the growth temperature, the growth time and the V/Mn-ratio were set to 825°C, 10 min and 1125, respectively, at a partial pressure of the $(CH_3C_5H_4)_2Mn$ in the MOVPE reactor of 5.2×10^{-7} atm. The parameters for the growth of the AlGaAs buffer layer and the MnAs clusters are also listed in table 2.2.

2.3.3 Influence of the orientation of the openings on the cluster growth

In order to investigate the influence of the orientation of the openings in the SiO_2 mask with respect to the crystal axes of the underlying (111)B GaAs substrate on the growth of the MnAs nanoclusters, samples with two types of elongated mask openings were prepared. In the first case, the major axes of the elongated openings were oriented either parallel to the $\langle\bar{1}10\rangle$-direction of the substrate or perpendicular to it, i.e. along the $\langle\bar{2}11\rangle$-direction. For the second sample, the openings were oriented either along the $\langle\bar{1}10\rangle$-direction or rotated by an angle of 120° about the [111] direction. The SEM images of the resulting openings of both samples are shown on the left of figure 2.8. In both cases the openings are well defined due to the isotropic etching of the SiO_2 layer. The openings for the sample with an orientation either parallel or perpendicular to the $\langle\bar{1}10\rangle$-direction of the substrate have a length of about 900 nm and a width of 200 nm. The openings for the second sample are smaller in size with a length of about 650 nm and a width of 150 nm.

In the center of figure 2.8, SEM images of the resulting MnAs nanoclusters are shown. In both cases the nanoclusters assemble in the openings with a well defined orientation which is reflected by the formation of crystal facets. The a-axes of the clusters and the $\langle\bar{1}10\rangle$-direction of the substrate exhibit always the same crystallographic relationship [71, 68]. The clusters which were grown in openings with an axis of elongation parallel to the $\langle\bar{2}11\rangle$-direction (top images in figure 2.8) cannot reproduce the shape defined by the mask openings because of a faster growth rate along the a-axes of the clusters. This results in a more pronounced growth of the clusters perpendicular to the major axis of elongation compared to the clusters oriented parallel to the $\langle\bar{1}10\rangle$-direction of the substrate. The resulting cluster shape is schematically shown on the right of figure 2.8.

As can be seen on the SEM images, the preferred growth of the nanoclusters along the a-axes strongly influences the aspect-ratio of the clusters, defined as
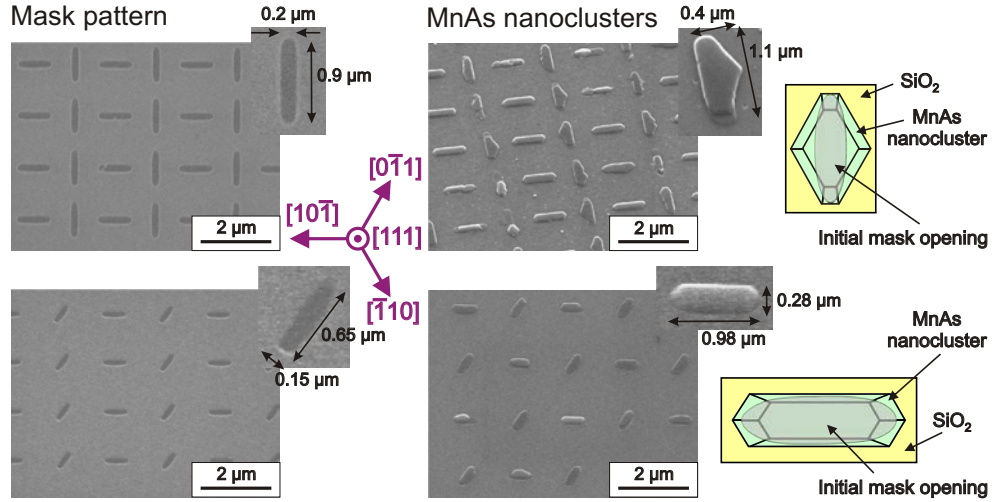
Figure 2.8: SEM images of the openings in the SiO$_2$ mask (left) and the corresponding MnAs clusters (middle). The crystal axes of the MnAs nanoclusters prefer to grow along the $\langle\bar{1}10\rangle$-direction of the substrate, what leads to small aspect ratios for openings perpendicular to the $\langle\bar{1}10\rangle$-direction of the substrate (top). For the clusters grown in openings parallel to the $\langle\bar{1}10\rangle$-direction (bottom) a large aspect-ratio can be achieved. The shapes of the MnAs nanoclusters for different orientations of the openings are schematically shown on the right.

the ratio between length and width. The nanoclusters grown perpendicular to the $\langle\bar{1}10\rangle$-direction have a length of about $1.1\,\mu$m and a width of $400\,$nm, and therefore an aspect-ratio of 2.75. However, the clusters grown parallel to the $\langle\bar{1}10\rangle$-direction show an aspect-ratio of 3.5 with a length of around $980\,$nm and a width of about $280\,$nm, although they were grown in initial openings with a smaller aspect-ratio than the clusters perpendicular to this direction. Thus, in order to obtain high quality clusters with a large aspect-ratio defined by the mask openings, the initial openings in the SiO$_2$ layer have to be oriented parallel to the $\langle\bar{1}10\rangle$-direction of the substrate or parallel to equivalent ones, which are rotated by 120° about the [111]-direction with respect to the $\langle\bar{1}10\rangle$-direction.

2.3.4 Influence of the fabrication process on the aspect-ratio

Not only the orientation of the openings, but also the fabrication process itself, has an influence on the aspect-ratio of the elongated MnAs clusters, i.e. due to the structuring of the SiO$_2$ layer and the self-assembled growth the aspect-ratio of the resulting nanoclusters strongly differs from the designed one. In order to investigate, how the aspect-ratio of the elongated nanoclusters is affected by the fabrication process, four samples with different mask openings were prepared. The openings of the four patterns designed had an aspect-ratio of 2, 4.8, 8 and 10, respectively, with a length of 310, 480, 600 and 300 nm and a width of 155,
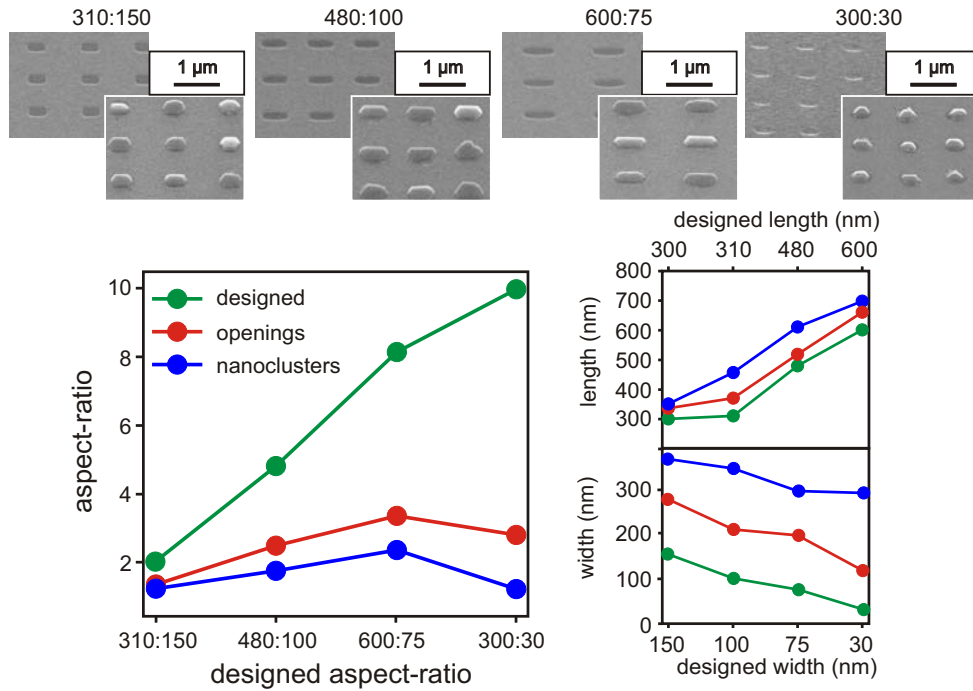
Figure 2.9: Influence of the fabrication process on the aspect-ratio of the elongated nanoclusters. Due to the structuring of the SiO$_2$ and the self-assembled growth, the aspect-ratio of the initial mask openings and the resulting nanoclusters is strongly decreased compared to the designed ones. SEM images of the corresponding mask openings and nanoclusters are shown on top.

100, 75 and 30 nm, respectively.

Figure 2.9 shows the influence of the structuring process and the self-assembled growth on the aspect-ratio of the elongated MnAs nanoclusters. As can be seen here the aspect-ratio of the initial mask openings in the SiO$_2$ layer after the etching step is drastically reduced compared to the designed ones, especially for the openings with a high aspect-ratio. The reason for this change of the aspect-ratio is, that, due to the structuring of the SiO$_2$ layer, all openings are increased of about 50 nm in length and 100 nm in width. The asymmetric change of the size of the mask openings is caused during the exposure of the resist due to the broadening of the electron beam and the proximity effect. In addition, the developing and the wet-chemical etching process lead to an isotropic increase of the size of the openings. Nevertheless, the relative change of the width due to the structuring process is much larger than the relative change of the length of the mask openings leading to a decrease of the aspect-ratio, which mainly affects the small openings with a high aspect-ratio. For example, the mask openings with a designed aspect-ratio of 10, i.e. a length of 300 nm and a width of 30 nm, show in the SEM images a length of 350 nm and a width of 120 nm. Due to the structuring the length and the width are therefore increased by 117% and 400%, respectively, which results in a reduction of the aspect-ratio
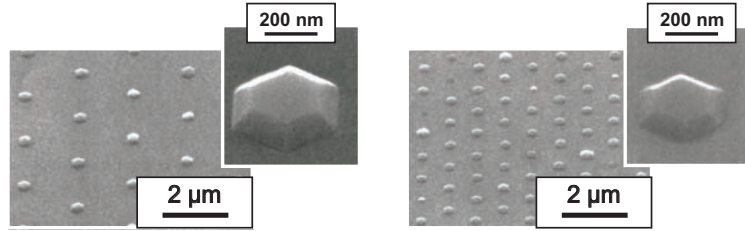
Figure 2.10: SEM images of the regularly arranged hexagon-shaped MnAs nanoclusters. The diameter of the nanoclusters varies between 170 nm and 1.2 μm.

by a factor of 3.4.

But not only the structuring of the SiO$_2$ layer, also the self-assembled growth decreases the aspect-ratio of the nanoclusters. After the formation of the MnAs clusters with well defined crystal facets in the openings, the single nanoclusters seem to grow isotropically in lateral direction with increasing growth time. The same behaviour can also be observed for the growth of hexagon-shaped nanoclusters, whose diameter increases continuously with increasing growth time [69]. Due to the isotropic growth the relative enhancement in size of a MnAs nanocluster along the minor axis is therefore larger than along the major axis leading to a decreasing aspect-ratio of the elongated MnAs cluster compared to the initial opening.

Thus, the structuring of the SiO$_2$ mask as well as the isotropic growth in lateral direction limits the minimal size of the nanoclusters.

2.3.5 Prepared arrangements of nanoclusters and cluster chains

Five different samples of self-assembled nanoclusters were grown by selective-area MOVPE on pre-patterned (111)B-GaAs substrates based on the findings described above. The first sample consists of different regular arrangements of hexagon-shaped nanoclusters. The diameter of the nanoclusters varies between 260 nm and 1.8 μm with a pitch between 1 and 3 μm. SEM images of two of the grown arrangements are exemplarily shown in figure 2.10.

Each of the remaining four samples consists of four different cluster arrangements. Three samples were grown with elongated nanoclusters, which have a length of 700 nm and a width of 350 nm. SEM images of the different arrangements of elongated nanoclusters are shown in figure 2.11. On the first sample, the major axis of the elongated clusters is always oriented along the $\langle\bar{1}10\rangle$-direction of the (111)B GaAs substrate. The first arrangement of this sample is an array of nanoclusters with a pitch of 1.5 μm along the $\langle\bar{1}10\rangle$-direction and of 1.0 μm along the $\langle\bar{2}11\rangle$-direction, resulting in a cluster density of 6.53×10^7 nanoclusters per cm^2, i.e. the nanoclusters cover 16.7% of the surface. In the second arrangement the pitch along the $\langle\bar{1}10\rangle$-direction was reduced to 1.0 μm and increased along the $\langle\bar{2}11\rangle$-direction to 1.5 μm in order to keep a constant cluster density on the surface. Furthermore, the clusters are no longer arranged

a) Sample 1
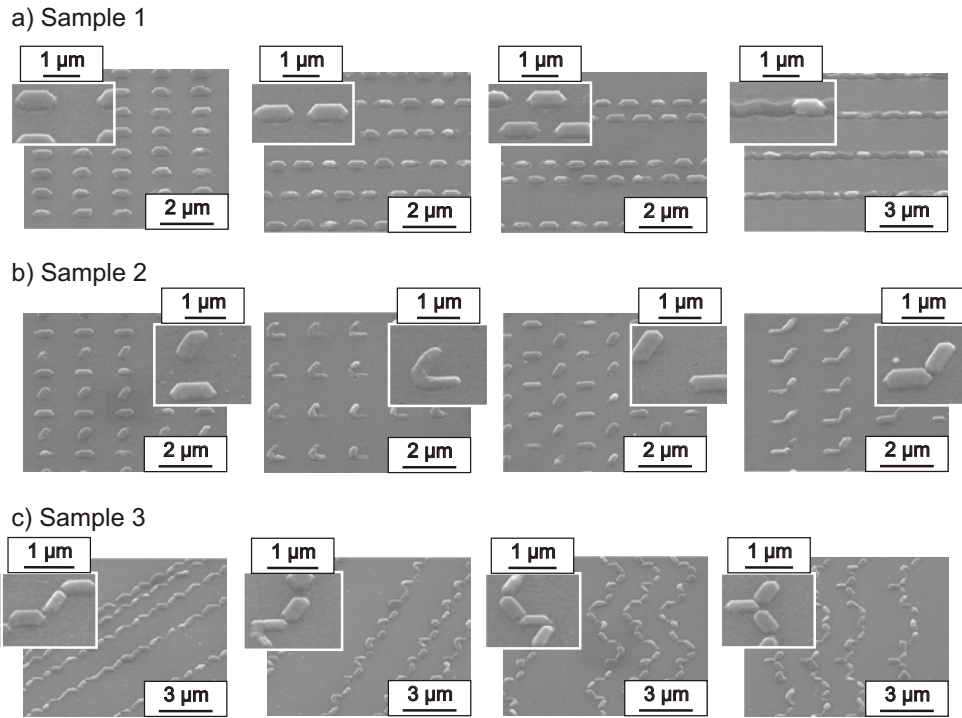
b) Sample 2

c) Sample 3

Figure 2.11: SEM images of the three prepared samples with different arrangements of elongated nanoclusters.

on a rectangular grid. Instead every second line of nanoclusters was shifted about $500\,\mathrm{nm}$ along the $\langle\bar{1}10\rangle$-direction. For the third and fourth arrangement, every second cluster row was shifted successively along the $\langle\bar{2}11\rangle$-direction in order to decrease the distance between the clusters. For the fourth arrangement the designed distance between the mask openings of neighboured cluster rows was reduced to $75\,\mathrm{nm}$, in order to achieve a merging of the nanoclusters during the growth resulting in cluster chains along the $\langle\bar{1}10\rangle$-direction, as shown on the right SEM image in figure 2.11 a).

The second sample consists of four arrangements with elongated nanoclusters with a major axis oriented along the $\langle\bar{1}10\rangle$-direction. Every second cluster was rotated by an angle of $120°$ about the $[111]$-direction, as shown in figure 2.11 b). For two arrangements the pitch along the $\langle\bar{1}10\rangle$-direction is $1.5\,\mu\mathrm{m}$ and $1.2\,\mu\mathrm{m}$ along the $\langle\bar{2}11\rangle$-direction, while for the other two arrangements two clusters of different orientation were grown next to each other to obtain cluster complexes of two coupled nanoclusters of different orientation.

On the third sample with elongated nanoclusters, four different kinds of cluster chains were grown, which are shown in figure 2.11 c). As in the case of the arrangement with cluster chains oriented along the $\langle\bar{1}10\rangle$-direction, the designed distance between the openings in the SiO_2 layer was $75\,\mathrm{nm}$, to achieve a merging of the clusters during the growth. Unfortunately, the clusters show some small openings.
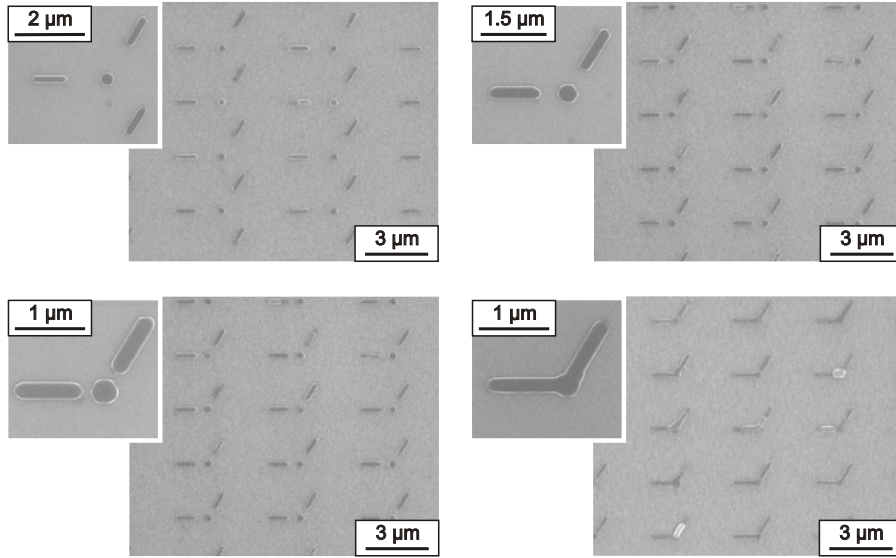
Figure 2.12: SEM images of the fivth sample with a structure consisting of one hexagon-shaped nanocluster and two elongated clusters. The distance of the initial mask openings between the clusters was succesively reduced in order to investigate the cluster coupling.

Finally, on the last sample, a structure consisting of one hexagon-shaped nanocluster and two elongated nanoclusters was grown. One elongated cluster is oriented along the $\langle\bar{1}10\rangle$-direction, while the other one is rotated by 120° about the [111]-direction with respect to the first cluster. Several of these structures are regularly arranged on the sample surface with a pitch of 3.6 - 5.4 μm along the $\langle\bar{1}10\rangle$-direction and 2.5 μm along the $\langle\bar{2}11\rangle$-direction as shown in figure 2.12. The hexagon-shaped nanocluster has a diameter of 340 nm, while the elongated clusters are 1 μm × 200 nm in size resulting in a high aspect-ratio of 5. This high aspect-ratio was obtained preparing initial mask openings in the SiO_2 layer with a length of 900 nm and a width of 100 nm. In order to investigate the magnetic coupling between the different nanoclusters the distances between them was gradually reduced throughout the series of four arrangements, i.e. the distance of the initial mask openings was chosen 1000, 400, 200 and 75 nm, respectively. Due to the fabrication process of the SiO_2 mask and the isotropic growth of the clusters the distance between the grown clusters is shortened by 80-100 nm compared to the designed distance leading to a merging of the clusters for the last arrangement.

In summary, this chapter proves that different arrangements of clusters and cluster chains can easily be generated by the controlled positioning of the openings in the SiO_2 layer.

3 Magnetic properties

As shown in the previous chapter, self-assembled growth of MnAs nanoclusters on pre-patterned substrates offers a great potential to build new planar spintronic and magnetoelectronic devices, because arrangements of ferromagnetic nanoclusters of different shapes with well defined crystal facets can easily be grown by controlling the position of the mask openings in SiO_2 layers. In order to realize spintronic and magnetoelectronic devices consisting of these nanoclusters, it is important to investigate and understand their magnetic properties, such as the domain structure and the magnetization orientation.

Different characterisation methods were used in order to determine the magnetic properties of the nanoclusters. The first part of this chapter deals with the superconducting quantum interference device (SQUID) measurements, which were performed in order to measure the temperature dependence of the magnetic susceptibility of the clusters. In the second part the results of the ferromagnetic resonance (FMR) measurements are presented, which were carried out investigate the magnetic anisotropy of the ferromagnetic MnAs nanoclusters. Finally, in the third part the results of magnetic force microscopy (MFM) measurements are discussed, which offer the possibility to investigate the structure and the formation of ferromagnetic domains.

3.1 SQUID measurements

Superconducting quantum interference devices (SQUIDs) are the most sensitive sensors for measuring the magnetic flux. Because they also offer the possibility to determine the magnetic moments directly SQUID measurements were used in order to measure the magnetization curve and to determine the Curie-temperature of the nanoclusters.

3.1.1 Operation mode of a SQUID magnetometer

A SQUID consists of a superconducting loop, which is interrupted by one or two normal-conducting or insulating barriers, so-called Josephson junctions. Such a loop with two junctions is schematically shown in figure 3.1 a). The current, which flows through the superconducting loop, is carried by Cooper-pairs, consisting of two electrons interacting with each other via the lattice deformation caused by the electrons [72, 73]. If the barriers are not too thick, the Cooper-pairs can tunnel through the junctions on both sides of the loop, which leads to a dc current even without an applied voltage. This effect is called
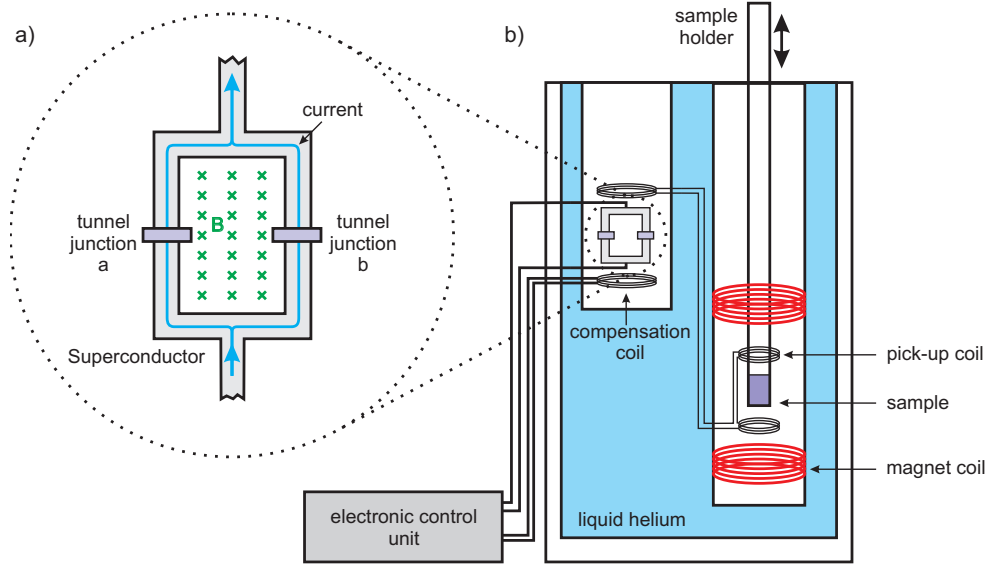
Figure 3.1: Schematic illustration of a SQUID consisting of a superconducting
loop with two Josephson-junctions a) and sketch of the set-up for a
SQUID magnetometer b).

dc-Josephson effect after B.D. Josephson, who predicted this effect in 1962 [74].
Due to the tunneling of the Cooper-pairs through the two barriers a and b a
phase shift in the total wavefunction of the Cooper-pairs occurs, which results in
interference of the two superpositioned currents. The superconducting current
through the SQUID depends on the phase shift difference δ and is given by:

$$I = I_0 \sin(\delta) = I_0 \sin(\delta_b - \delta_a), \tag{3.1}$$

where I_0 is a maximal critical current density, which can be carried by the
cooper-pairs, and δ_a and δ_b denotes the phase shifts caused by the tunneling
through barrier a and b, respectively.

Applying a magnetic field perpendicular to the loop causes an additional ef-
fect, which is used in SQUIDs. Due to the quasi-macroscopic character of the
total wavefunction of the Cooper-pairs, the phase difference of the wavefunc-
tion around a closed circuit has to be 2π, which leads to a quantization of the
magnetic flux Φ_{magn} in the loop:

$$\Phi_{\mathrm{magn}} = n \frac{h}{2e} \qquad n = 1, 2, 3, \ldots \tag{3.2}$$

where h is Planck's constant and Φ is the sum of the magnetic flux due to the
magnetic field and the currents in the circuit itself. Applying a magnetic field
to a SQUID therefore results in an additional phase difference:

$$\delta_b - \delta_a = \frac{2e}{\hbar} \Phi_{\mathrm{magn}} \tag{3.3}$$

and for the current follows:

$$I = 2 I_0 \sin(\delta) \cos\left(\frac{e}{\hbar} \Phi_{\mathrm{magn}}\right). \tag{3.4}$$

The superconducting current through the parallel circuit of the two Josephson junctions therefore oscillates with the magnetic flux passing through the loop and has maxima, when a flux quant ($\Phi_{\mathrm{magn}} = h/2e$) enters the loop.

The set-up of a common SQUID magnetometer is shown in figure 3.1 b). The sample, which is separated from the SQUID-detector in order to prevent a disturbtion of the detector due to the magnetic moment of the sample, is moved with a certain frequency between two superconducting coils. The magnetic moment induces a current in these so-called pick-up coils, which on the other hand induce a magnetic field crossing the SQUID. In order to measure the magnetic moment of the sample an additional magnetic field is generated in the compensation coil by an alternating current with the frequency of the moving sample to compensate the magnetic field crossing the SQUID. The electronic system regulates the current in such a way, that the magnetic field through the SQUID vanishes. With the current strength the magnetic moment of the sample can be calculated.
Additionally, superconducting coils are arranged at the sample position, in order to magnetize the sample before the measurement and to have the possibility to measure the magnetic susceptibility in applied magnetic fields.

3.1.2 Results of the SQUID measurements

In order to determine the temperature dependence of the magnetization of the nanoclusters, SQUID measurements were performed at the Lehrstuhl Experimentalphysik V of the University of Augsburg for the samples with random distributions of hexagon-shaped MnAs nanoclusters and for regularly arranged hexagon-shaped nanoclusters grown by selective-area MOVPE. During the measurements an external magnetic field of 1 T was applied. The results of the different measurements are shown in figure 3.2.
Because of the ferromagnetic MnAs nanoclusters, all samples show a decreasing magnetization with increasing temperature, which is typical for ferromagnetism. Additionally, for all four samples, a negative contribution to the magnetization is observed, which arises from the diamagnetic GaInAs and GaAs substrates. For each of the samples with randomly distributed nanoclusters this diamagnetic contribution is larger than the ferromagnetic one resulting in a negative total magnetization in the entire temperature range, while for the sample with the regular arranged nanoclusters a negative total magnetization can only be found at high temperatures. At temperatures above the Curie-temperature the ferromagnetic contribution vanishes and only the diamagnetism of the substrate is observable offering the possibility to determine the Curie-temperature of the MnAs nanoclusters.
The randomly distributed hexagon-shaped nanoclusters show ferromagnetism up to 330 K, while for the regular arranged hexagon-shaped nanoclusters a Curie-temperature of even 340 K can be found. Both kinds of MnAs nanoclusters therefore possess a slightly higher Curie-temperature than bulk MnAs or MnAs thin films with a Curie-temperature of 318 K [75, 76]. An increased
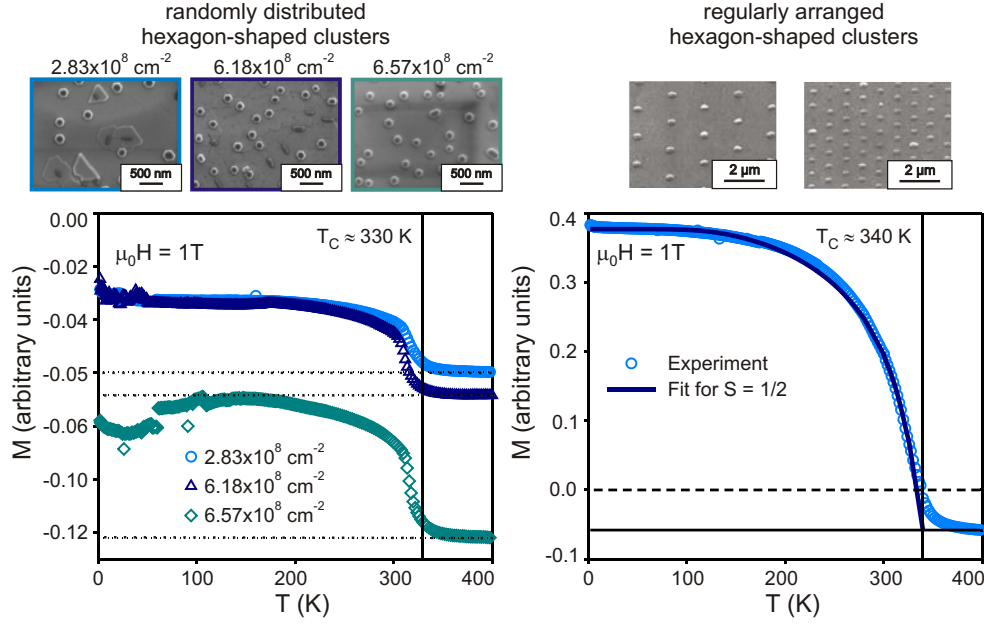
Figure 3.2: Magnetization curves of the randomly distributed and regularly arranged hexagon-shaped MnAs nanoclusters measured by SQUID in an applied magnetic field of 1 T. The randomly distributed clusters show ferromagnetism up to 330 K, while for the regularly arranged cluster a Curie-temperature of even 340 K is observable. Due to the diamagnetic substrates a negative contribution to the magnetization can be found for all samples.

T_C of 330 - 340 K is also observed for MnAs nanoclusters in conventionally synthesized GaMnAs/MnAs hybrid structures prepared by MOVPE at high growth temperatures [77, 9] or by implantation of Mn^+-ions in GaAs followed by thermal annealing [55]. This enhancement of T_C may originate from different sources, such as strain or a single domain character of the nanoclusters. Because GaMn precipitates in GaMnAs show Curie-temperatures up to 400 K [55, 54, 78] another possible explanation may be the diffusion of Ga into the MnAs nanocluster during the growth. As Lampalzer et al. have shown up to 13±4 at.% of Ga can be found in MnAs nanoclusters of GaMnAs/MnAs hybrids grown by MOVPE [79] and also the self-assembled hexagon-shaped nanoclusters on GaInAs substrates possess a small Ga amount of 0.6 at.% [63].

The magnetization curve of the regularly arranged hexagon-shaped nanoclusters was also fitted using equation (1.36), which is shown as solid line in figure 3.2. Because the ferromagnetic behaviour in the half-metallic MnAs is caused by itinerant exchange mediated by the delocalized $3d$ electrons [80, 81, 82, 83], the magnetization curve should exhibit a temperature dependent behaviour which is typical for a spin 1/2 system. As can be seen in figure 3.2, a very good agreement between experiment and theory can be achieved for $J = 1/2$, confirming that the delocalized $3d$ electrons are responsible for the ferromagnetic coupling in the MnAs nanoclusters.

3.2 Ferromagnetic resonance measurements

Ferromagnetic resonance (FMR) measurements are well suited for analysing the magnetic anisotropy, because with this method it is possible to obtain information about the anisotropy directly [21]. Since the magnetic anisotropy determines the orientation of the magnetization without an external magnetic field, it has a large influence on the magnetic and transport properties of the prepared samples. Therefore an improved understanding of the magnetic anisotropy of the nanoclusters is necessary in order to optimize the sample properties for magnetoelectronic devices. Like the SQUID measurements, the ferromagnetic resonance measurements for the investigation of the magnetic anisotropy of the MnAs clusters were performed at the Lehrstuhl Experimentalphysik V of the University of Augsburg.

3.2.1 Theortical description of electron paramagnetic resonance

Because the technique of FMR is related to standard electron paramagnetic resonance (EPR), a brief description of EPR is given first.

Applying a magnetic field to a paramagnetic solid leads to a splitting of the spin-degenerated energy levels of the total angular momentum as described in section 1.1.2. This effect is called Zeeman effect after P. Zeeman, who discovered this phenomenon in 1897 [84]. The energy difference ΔE_z between the different energy levels of the total angular momentum for an applied magnetic field in z-direction B_z is then given by:

$$\Delta E_z = g\mu_{\mathrm{B}}B_z, \tag{3.5}$$

where g is the Landé-factor as defined in equation 1.13. In solids, where the Landé-factor might be transformed into a tensor due to the anisotropy of the crystal field, g denotes the component of the Landé-tensor $\boldsymbol{g}$ parallel to the applied magnetic field.

An additional exposure of the solid to electromagnetic radiation in the microwave range of frequency ν may result in resonant absorption of the radiation due to the excitation of transitions between the two spin states, if the resonance condition

$$h\nu = \Delta E_z = g\mu_{\mathrm{B}}B_z \tag{3.6}$$

is fullfilled. Commonly the frequency of the microwave is constant in experiment and the magnetic field is varied leading to the rewritten resonance condition for the magnetic field B_{res}:

$$B_{\mathrm{res}} = \frac{h\nu}{g\mu_{\mathrm{B}}}. \tag{3.7}$$

The paramagnetic resonance, which was first discovered by Zavoisky in 1945 [85], can classically be interpreted as a precession of all magnetic moments, i.e. of the magnetization of the solid, about the direction of the external magnetic field $\vec{B}_0$. As F. Bloch showed in 1946 for nuclear magnetic resonance (NMR) [86, 87], the precession of the magnetic moments can be described with

a phenomenological theory, which is equivalent to the quantum-mechanical description. The classical equation of motion for the magnetization, which is also applicable to describe the EPR, is given by:

$$\frac{\partial \vec{M}}{\partial t} = \gamma \vec{M} \times \vec{B}_0, \tag{3.8}$$

where the gyromagnetic ratio is defined as:

$$\gamma = \frac{g\mu_{\mathrm{B}}}{\hbar}. \tag{3.9}$$

After the absorption of the electromagnetic radiation the precessing magnetization will relax towards its equilibrium value due to the spin-spin and spin-lattice interaction. For a magnetic field along the z-direction the relaxation of the magnetization towards its equilibrium value $\vec{M}_0 = (0, 0, M_0)$ can be described by the Bloch-equations:

$$\frac{\partial M_x}{\partial t} = \gamma(\vec{M} \times \vec{B}_0)_x - \frac{M_x}{T_2}, \tag{3.10}$$

$$\frac{\partial M_y}{\partial t} = \gamma(\vec{M} \times \vec{B}_0)_y - \frac{M_y}{T_2}, \tag{3.11}$$

$$\frac{\partial M_z}{\partial t} = \gamma(\vec{M} \times \vec{B}_0)_z - \frac{M_0 - M_z}{T_1}, \tag{3.12}$$

where T_1 is the longitudinal spin-lattice relaxation time , which describes the relaxation of M_z to the equilibrium magnetization M_0 [88], while the relaxation of M_x and M_y to zero is described by the transversal spin-spin relaxation time T_2 [86].

3.2.2 Principles of ferromagnetic resonance

In 1950 N. Bloembergen showed that the Bloch-equations can also be used for describing the resonance of ferromagnetic systems just by modifying the term of the magnetic field [88]. For a description of the ferromagnetic resonance the magnetic field $\vec{B}_0$ is replaced by the sum of the external magnetic field $\vec{B}_0$ and the additional internal fields $\vec{B}_{\mathrm{FM}}$ of a ferromagnetic solid. The equation of motion can then be written as:

$$\frac{\partial \vec{M}}{\partial t} = \gamma \vec{M} \times \vec{B}_{\mathrm{tot}}, \tag{3.13}$$

with

$$\vec{B}_{\mathrm{tot}} = \vec{B}_0 + \vec{B}_{\mathrm{FM}}. \tag{3.14}$$

The ferromagnetic resonance is therefore shifted compared to the paramagnetic resonance, depending on the properties of the ferromagnet along the direction of the external magnetic field. In general, the ferromagnetic properties, like the magnetic anisotropy, also have the effect, that the magnetization and the external magnetic field are not aligned in parallel. Thus, a determination of
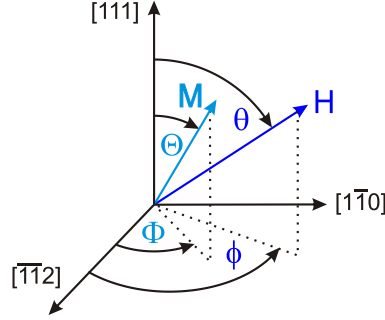
Figure 3.3: Definition of the used coordinate system with respect to the geometry of the (111)B GaAs substrate. The angles of the magnetization are denoted with capital letters Θ and Φ, while for the external magnetic field small letters θ and ϕ are used.

B_{tot} may become very complicated. In a different approach B_{tot} is determined by the total free energy density U_{tot} [89]:

$$\vec{B}_{\text{tot}} = -\vec{\nabla}_M U_{\text{tot}}, \tag{3.15}$$

which consists of three different contributions U_{Zee}, U_{demag} and U_{ani} due to the magnetostatic or Zeeman energy, the demagnetization energy and the anisotropy energy, respectively [90, 91]:

$$U_{\text{tot}} = \frac{F_{\text{tot}}}{V} = U_{\text{Zee}} + U_{\text{demag}} + U_{\text{ani}}. \tag{3.16}$$

It is often advantageous to choose an appropriate coordinate system in order to derive the resonance condition of the free energy density. The spherical coordinate system, which was used in this work for describing the ferromagnetic resonance measurements, is shown in figure 3.3. The angles are given by the orientation of the saturation magnetization $\vec{M}(\Theta, \Phi)$ and of the external magnetic field $\vec{B}_0(\theta, \phi)$. In the following the different contributions to the free energy density will also be presented in this coordinate system.

Magnetostatic or Zeeman energy
The magnetostatic or Zeeman energy contribution to the free energy density arises from the energy of the magnetization $\vec{M}$ in an external magnetic field. It is the only contribution, which depends directly on the external magnetic field $\vec{B}_0$ and is given by:

$$U_{\text{Zee}} = \frac{F_{\text{Zee}}}{V} = -\vec{M}\vec{B}_0. \tag{3.17}$$

In spherical coordinates as defined in figure 3.3 U_{Zee} can be written as [92]:

$$\begin{aligned} U_{\text{Zee}} \ = \ & -MB_0(\sin\Theta \sin\Phi \sin\theta \sin\phi + \\ & + \sin\Theta \cos\Phi \sin\theta \cos\phi + \cos\Theta \cos\theta). \end{aligned} \tag{3.18}$$

Demagnetization energy
The second contribution to the free energy density is caused by the dipole-dipole interaction. Because of the resulting magnetization in a ferromagnet
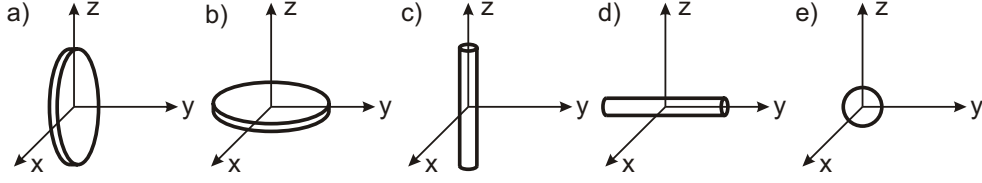
Figure 3.4: Schematic representation of the sample shape for different limiting
cases (after Ref. [95]).

the Maxwell equation $\vec{\nabla}\vec{B} = 0$ is only fulfilled, if a virtual polarization of the
sample surface is assumed, which generates a demagnetization field $\vec{B}_{\text{demag}}$.
The demagnetization field strongly depends on the shape of the sample [93, 94]
and can be written for a homogeneous magnetization as:

$$\vec{B}_{\text{demag}} = \mu_0 \boldsymbol{N}\vec{M}. \tag{3.19}$$

$\boldsymbol{N}$ denotes the demagnetization tensor which accounts for the shape of the
sample. The contribution of the demagnetization energy, which is also called
shape anisotropy, is therefore given by:

$$U_{\text{demag}} = \frac{\mu_0}{2}\vec{M}\boldsymbol{N}\vec{M}. \tag{3.20}$$

For ellipsoidal samples the demagnetization tensor $\boldsymbol{N}$ can be diagonalized, i.e.

$$N_{xx} = N_x, \quad N_{yy} = N_y \quad \text{and} \quad N_{zz} = N_z. \tag{3.21}$$

N_x, N_y and N_z are the demagnetization factors, which only depend on the
sample shape and which fulfill the normalization condition $N_x + N_y + N_z = 1$.
Figure 3.4 shows different limiting cases of the sample shape. The corresponding
demagnetization factors are listed in table 3.1.

Anisotropy energy
As described in section 1.2.1 the dipole-dipole as well as the spin-orbit inter-
action lead to a magnetic anisotropy in a ferromagnetic solid. Due to their

shape	magnetization orientation	see figure 3.4	demagnetization factors		
			N_x	N_y	N_z
infinitely thin plate	tangential	a)	0	1	0
	normal	b)	0	0	1
infinitely thin cylinder	tangential	c)	1/2	1/2	0
	normal	d)	1/2	0	1/2
sphere		e)	1/3	1/3	1/3

Table 3.1: Demagnetization factors for the different limiting cases of the sample
shape shown in figure 3.4 (after Ref. [95]).

hexagonal crystal structure the magnetic anisotropy contribution of the investigated MnAs nanoclusters to the free energy density can be written as [96]:

$$U_{\mathrm{ani}} = \frac{F_{\mathrm{ani}}}{V} \quad = \quad K_0 + K_1 \sin^2 \Theta + K_2 \sin^4 \Theta +$$
$$+ K_3 \sin^6 \Theta + K_3' \sin^6 \Theta \cos(6\Phi). \qquad (3.22)$$

The anisotropy constants K_1, K_2 and K_3 are responsible for an uniaxial anisotropy along the z-direction. Only the anisotropy constant K_3' describes the hexagonal symmetry of the crystal structure in the sample plane. Neglecting the last term, equation 3.22 can therefore be used in order to describe the magnetic anisotropy of all crystals with an uniaxial anisotropy.

Resonance condition
Using the Lagrange formalism the resonance condition for the FMR in a spherical coordinate system can be written as [97, 98, 99]:

$$\left(\frac{\omega}{\gamma}\right)^2 = \frac{1}{M^2 \sin^2(\Theta)} \left[\left(\frac{\partial^2 U_{\mathrm{tot}}}{\partial \Phi^2}\right) \left(\frac{\partial^2 U_{\mathrm{tot}}}{\partial \Theta^2}\right) - \left(\frac{\partial^2 U_{\mathrm{tot}}}{\partial \Theta \partial \Phi}\right)^2 \right]_{\Theta_0, \Phi_0}, \qquad (3.23)$$

with $\omega = 2\pi\nu$ is the Larmor frequency. The equilibrium orientation of the magnetization $M(\Theta_0, \Phi_0)$, i.e. the minimum of the free energy density for a given direction of the external magnetic field, has to be calculated from:

$$\left(\frac{U_{\mathrm{tot}}}{\partial \Theta}\right)_{\Theta = \Theta_0} = 0 \quad \text{and} \quad \left(\frac{U_{\mathrm{tot}}}{\partial \Phi}\right)_{\Phi = \Phi_0} = 0. \qquad (3.24)$$

Therefore, the equation system with the three equations 3.23 and 3.24 has to be solved in order to determine the magnetization orientation in equilibrium $M(\Theta_0, \Phi_0)$ and the resonance field $B_{\mathrm{res}} = \omega/\gamma$ for a given orientation of the external magnetic field. It can be shown, that a high resonance field indicates a hard axis of magnetization, while along an easy axis only a low B_{res} is observable [100].

3.2.3 Experimental setup for the FMR measurements

The FMR measurements were performed using a Bruker EPR-spectrometer. A schematic scetch of the experimental setup is shown in figure 3.5 a). The microwaves, which have a frequency of $\nu = 9.359$ GHz, are generated in a X-band Gunn-diode, split and send into two arms. One arm guides the microwave via a circulator into the resonantor, where the sample is mounted. The resonator is located in a flow cryostat, in order to cool the sample with liquid helium, and between two magnetic coils, which generate a homogeneous external magnetic field. The frequency of the microwave radiation has to match the resonance frequency of the resonator, which results in an absorption of the microwave. During the measurement the applied magnetic field is varied leading to a change of the resonance frequency of the sample. If the resonance condition is fulfilled,
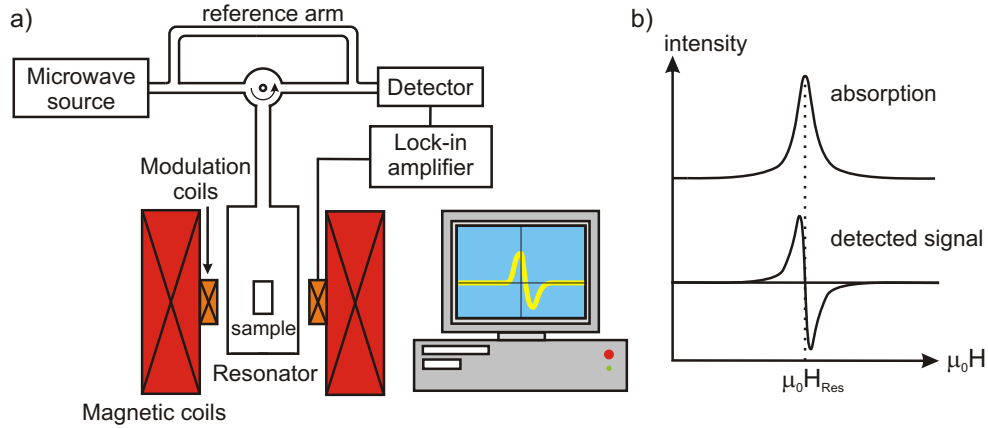
a)

b)

Figure 3.5: a) Experimental setup for the FMR measurements. The Gunn-diode generates microwave radiation, which is partly reflected by the sample in the resonator, if the resonance condition is fulfilled. The reflected signal is detected with a diode. b) Due to the lock-in amplifier the measured signal is the first derivative of the Lorentzian-shaped absorption curve.

i.e. if the sample's resonance frequency matches the frequency of the incoming radiation, also the sample absorbs microwave radiation leading to a slight detuning of the resonator. Therefore a part of the microwave is reflected and guided to the detection diode. The second arm works as a reference in order to adjust the diode to guarantee an optimal performance. With a phase shifter the phase of the transmitted microwave in the reference arm can be regulated to the phase in the resonator arm. Because a lock-in amplifier is used in order to achieve a better signal-to-noise ratio, additional small coils modulate the magnetic field with an alternating field of small amplitude. Due to the modulation not the Lorentzian-shaped curve of the absorption signal is detected, but its first derivative as shown in figure 3.5 b). The resonance field can then be determined as the zero crossing point of the signal.

Angle-dependent measurements were performed for the investigation of the anisotropy of the samples. For this purpose the samples were not mounted on a fixed sample holder, but could be rotated about an axis with a goniometer. For the investigation of the MnAs nanoclusters, measurements in two different geometries were performed, which are schematically shown in figure 3.6. In the first geometry, figure 3.6 a), the sample was rotated about the [111]-direction resulting in a rotation of the magnetic field in the sample plane. In this geometry, which is called in the following in-plane geometry, an angle of $\alpha = 0°$ corresponds to $\vec{H} \parallel [11\bar{2}]$. In the second geometry, figure 3.6 b), a rotation of the magnetic field out of the sample plane was achieved by a rotation of the sample about the [$\bar{1}$10]-direction. In the following this geometry is called out-of plane geometry. Here $\alpha = 0°$ denotes an orientation of the magnetic field parallel to the [$\bar{1}\bar{1}2$]-direction.

3.2.4 Results for the randomly distributed MnAs nanoclusters

For the samples with the randomly distributed hexagon-shaped MnAs nano-
clusters grown on (111)B GaInAs/InAs surfaces angle-dependent FMR mea-
surements were performed at 150 K in steps of 5°. Figure 3.7 a) and b) show
colour-plots of the intensity of the FMR signal in the out-of-plane geometry for
the samples with a cluster density of 2.83×10^8 and 6.57×10^8 nanoclusters per
cm^2, respectively.
For the sample with the lowest cluster density of 2.83×10^8 nanoclusters per
cm^2 the FMR measurements show a weak 180° anisotropy with a high reso-
nance field along the [111]- and the [$\bar{1}\bar{1}\bar{1}$]-direction, i.e. parallel to the c-axes of
the nanoclusters, while for an orientation of the external magnetic field in the
sample plane, the resonance field becomes minimal. This indicates a hard mag-
netic axes along the c-axes of the hexagon-shaped MnAs nanoclusters and an
easy axes perpendicular to it. The orientation of the magnetization in the clus-
ter plane was also observed by Hara et al. [63], who performed angle-dependent
measurements of the magnetization for the randomly distributed nanoclusters
on (111)B GaInAs/InP surfaces. The magnetization of the nanoclusters there-
fore shows the same behaviour as in single MnAs crystals [101] and MnAs thin
films [102, 103], where a hard magnetic axis along the c-axis is also found.
Also for the sample with the highest cluster density of 6.57×10^8 cm^{-2} a two-fold
anisotropy in the out-of-plane geometry can be observed with a hard magnetic
axis parallel to the c-axis of the nanoclusters. But in contrast to the sample
with the lowest cluster density, two strong resonances are observable. As Krug
von Nidda et al. have shown, the two resonances arise from two different clus-
ter shapes [9], i.e. the hexagon-shaped nanoclusters and the cluster complexes,
which were observed by SEM as described in section 2.2. Due to the larger
cluster density the two resonances are much stronger than for the sample with
the lowest cluster density. Therefore ferromagnetic resonance measurements
were also performed in the in-plane geometry for the sample with the high-
est cluster density, which are shown on the right in figure 3.8 a). In in-plane
geometry the magnetization of the ferromagnetic MnAs nanoclusters shows a
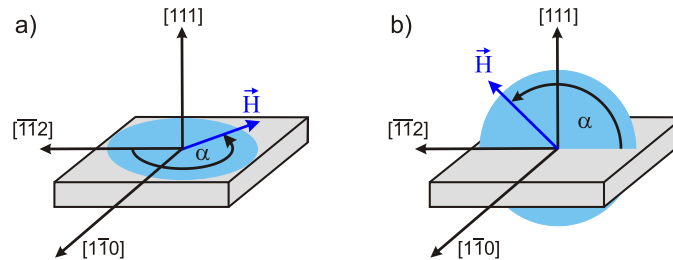weakly anisotropic behaviour exhibiting a sixfold symmetry due to the hexag-

Figure 3.6: Schematic representation of the two different sample geometries. a)
In the in-plane geometry the external magnetic field is rotated in
the (111)-plane. b) In the out-of-plane geometry the magnetic field
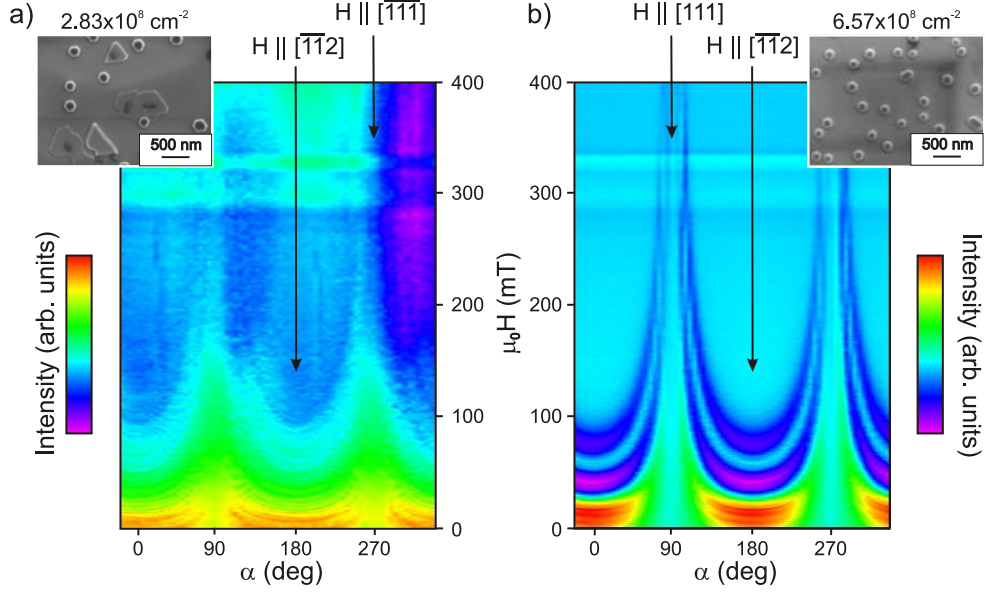is rotated in the (1$\bar{1}$0)-plane.

Figure 3.7: Colour-plot of the FMR measurements in out-of-plane geometry of the samples with a random cluster distribution. a) For the sample with a cluster density of 2.83×10^8 cm^{-2} only a weak 180° anisotropy can be found. b) A two-fold anisotropy with two strong resonances is observable for the sample with a cluster density of 6.57×10^8 cm^{-2} b).

onal crystal symmetry and the shape of the clusters.

For a determination of the different anisotropy parameters of the MnAs nanoclusters first the resonance field of the out-of-plane and in-plane measurements was determined by fitting the FMR signal with the first derivative of a Lorentzian lineshape. The fitting function is given by [104]:

$$\frac{dP}{dH} \propto \frac{d}{dH}\left(\frac{\Delta H + \alpha(H - H_{\mathrm{Res}})}{(H - H_{\mathrm{Res}})^2 + \Delta H^2} + \frac{\Delta H + \alpha(H + H_{\mathrm{Res}})}{(H + H_{\mathrm{Res}})^2 + \Delta H^2}\right), \qquad (3.25)$$

where P is the detected microwave power absorbed by the sample and ΔH is the full-width half maximum of the Lorentzian lineshape. The factor α is the dispersion to absorption ratio, which describes a partial mixing of the dispersion into the absorption signal arising from the Skin-effect in metallic samples. For large samples, with extensions much larger than the skin depth, absorption and dispersion are of equal strength resulting in an asymmetric line shape, i.e. $\alpha = 1$. For small samples, with extensions smaller than the skin depth, no mixture occurs and $\alpha = 0$. As the nanoclusters investigated are very small, a good agreement between equation 3.25 and the spectra measured can be achieved for $\alpha = 0$, despite their metallic conductivity [105]. The resonance fields obtained for both geometries are shown in figure 3.8 b) as open circles.

As described above, the cluster shape of the nanoclusters strongly influences the resonance field. For the theoretical description of the resonance the shape of the two types of nanoclusters was approximated by an ellipsoid, so that the de-
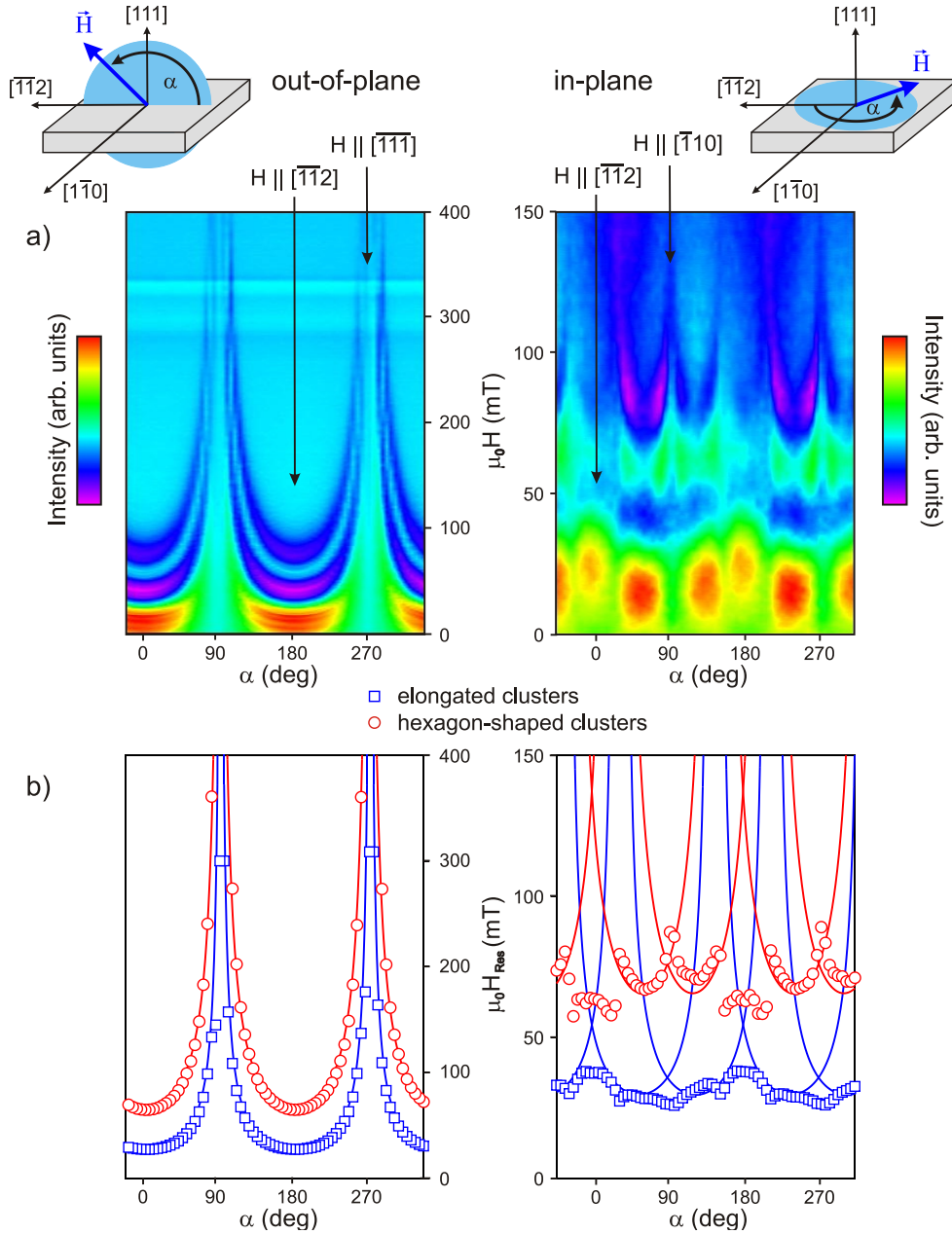
Figure 3.8: a) FMR measurements at 150 K in out-of-plane (left) and in-plane (right) geometry of the sample with the highest density of the randomly distributed nanoclusters. b) The solid lines represent the fit of the resonance fields for the elongated (blue squares) and the hexagon-shaped nanoclusters (red circles).

magnetization tensor can be diagonalized. In order to obtain the corresponding demagnetization factors the size of the clusters was determined from the SEM and AFM images shown in section 2.2. The hexagon-shaped nanoclusters have a diameter of about 150 nm and a height of approximately 70 nm, resulting in

the demagnetization factors $N_x = N_y = 0.24$ and $N_z = 0.52$. For the elongated cluster complexes, which consist of two hexagon-shaped nanoclusters, a length of 300 nm and a width of 150 nm was assumed. The corresponding demagnetization factors are $N_x = 0.273$, $N_y = 0.135$ and $N_z = 0.592$. For the determination of the anisotropy parameters the resonance fields in out-of-plane and in-plane geometry were fitted by solving equations 3.23 and 3.24. The results for both geometries are plotted as solid lines in figure 3.8 b). A very good agreement between theory and experiment can be achieved for the anisotropy parameters $K_1 = -1.1 \text{ J/m}^3$, $K_2 = 0.35 \text{ J/m}^3$, $K_3 = -0.25 \text{ J/m}^3$ and $K_3' = 0.0129 \text{ J/m}^3$. Just a variation of the cluster shape and therefore of the corresponding demagnetization factors is necessary to describe both observed resonances in the out-of-plane as well as in the in-plane geometry very well. It turns out, that the asymmetric shape of the elongated nanoclusters (blue squares) shifts their resonance to lower fields compared to the resonance of the hexagon-shaped nanoclusters (red circles), while the magnetization and its anisotropy are found to be independent on the cluster shape and size [9].

The obtained anisotropy parameters are also in good agreement with the parameters of bulk MnAs, which were determined from MnAs single crystals by R.W. de Blois and D.S. Rodbell in 1963 [106]. They determined the temperature-dependence of the sum of the anisotropy parameters $K_1 + 2K_2 + 3K_3$ and found a value of approximately -1.10 J/m^3 at 150 K, which is only a little bit larger than the value of -1.15 J/m^3 determined from the randomly distributed nanoclusters. However, de Blois and Rodbell neglected the anisotropy constant K_3', which is essential for a description of the hexagonal anisotropy in the sample plane and also slightly influences the resonance field in the out-of-plane geometry. Therefore the neglection of the parameter K_3' might be the reason for the small difference between the anisotropy parameters determined by de Blois and Rodbell and the values obtained for the randomly distributed nanoclusters.

3.2.5 Results for regularly arranged hexagon-shaped nanoclusters

FMR measurements for the sample with regularly arranged hexagon-shaped nanoclusters were performed at 300 K. Measurements at much lower temperatures were not possible due to the weak resonance signal, especially for the in-plane geometry.

Figure 3.9 shows the angular dependence of the resonance fields determined for the out-of-plane (left) and in-plane (right) geometry of the sample with regularly arranged hexagon-shaped nanoclusters. As for the randomly distributed hexagon-shaped nanoclusters a two-fold anisotropy is observed in the out-of-plane geometry, with a magnetization direction oriented in the sample plane and a hard magnetic axes parallel to the c-axes of the clusters, i.e. parallel to the $\langle 111 \rangle$-direction of the (111)B GaAs substrate. Although the diameter of the clusters on the sample varies between 255 nm and 1.8 μm as described in section 2.3.5, only one resonance feature is observed. The cluster size does not influence the resonance field, which is only determined by the cluster shape.

In the in-plane geometry only one weak resonance signal can be found, which
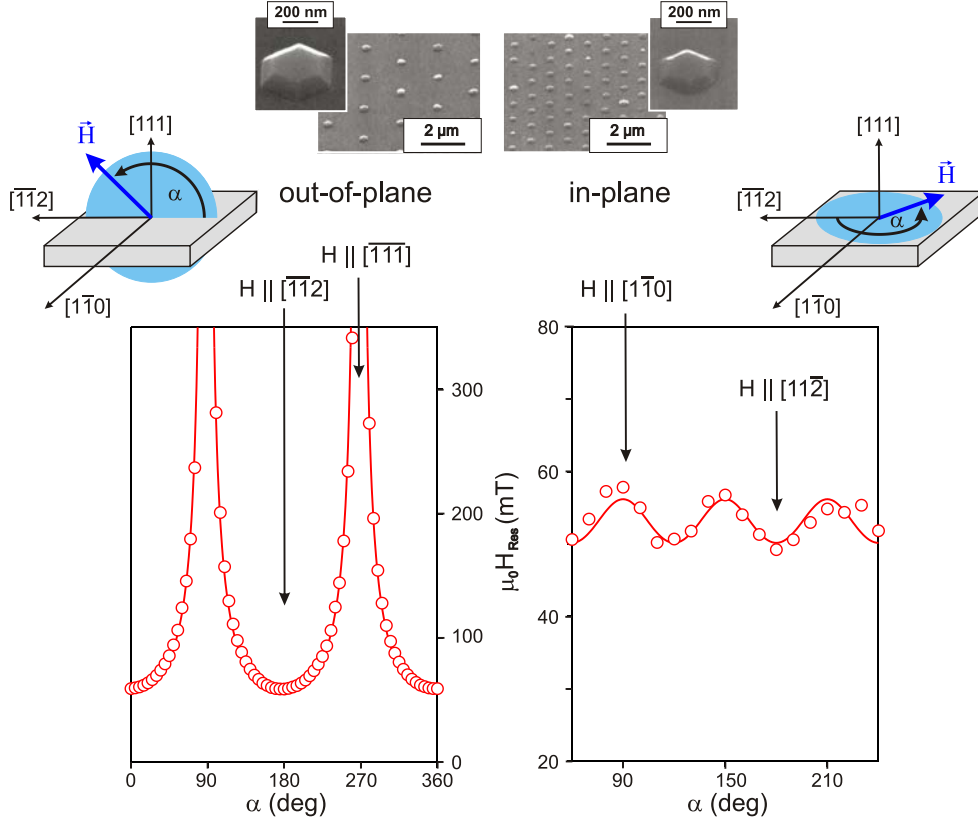
Figure 3.9: Angular dependence of the resonance fields at $300\,\mathrm{K}$ in out-of-plane (left) and in-plane (right) geometry of the sample with the regularly arranged hexagon-shaped nanoclusters on (111)B GaAs substrate. The calculated resonances are shown as solid lines.

shows a clear six-fold symmetry arising from the hexagonal crystal structure of the nanoclusters. In contrast to the sample with randomly distributed nanoclusters, the resonance field in the in-plane geometry exhibits a clear sine-dependence with a $60°$ periodicity. The minimas occur for an orientation of the magnetic field along the $\langle \bar{2}11 \rangle$-direction and equivalent directions, indicating an easy axis of magnetization between the a-axes of the nanoclusters, in accordance with the results by Hara et al. [63] and Friedland et al. [107].

The resonance fields for the regularly arranged hexagon-shaped MnAs nanoclusters were also calculated solving equations 3.23 and 3.24. Because of the different diameters of the clusters an average cluster diameter of $720\,\mathrm{nm}$ was assumed for the description of the single resonance. The cluster thickness of $50\,\mathrm{nm}$ was estimated from the SEM images. The resulting demagnetization factors used for the calculations are then given by $N_x = N_y = 0.06$ and $N_z = 0.88$. As can be seen in figure 3.9 as solid lines a good agreement between theory and experiment is achieved for the anisotropy parameters $K_1 = -0.575\,\mathrm{J/m^3}$, $K_2 = 0.15\,\mathrm{J/m^3}$, $K_3 = -0.12\,\mathrm{J/m^3}$ and $K_3' = 0.0001\,\mathrm{J/m^3}$. As for the randomly distributed hexagon-shaped nanoclusters the parameters obtained are in good agreement with the parameters determined by de Blois and Rodbell [106].

For bulk MnAs they found the values $K_1 = -0.575\,\text{J/m}^3$, $K_2 = 0.15\,\text{J/m}^3$, $K_3 = -0.115\,\text{J/m}^3$ at 308 K. Only the value for K_3 is slightly decreased compared to the value obtained from the regularly arranged nanoclusters. This small difference might again result from the neglection of the in-plane contribution by de Blois and Rodbell as described in the previous section. Due to the strong temperature dependence of the anisotropy parameters at temperatures below T_C [106, 9] another possible explanation might also be the little lower measurement temperature of 300 K. The strong temperature dependence is also observed for the anisotropy parameter K_3', which decreases from a value of 0.0129 J/m^3 at 150 K to a value of only $0.0001\,\text{J/m}^3$ at 300 K. Although the obtained value for K_3' at 300 K is very small, a correct description of the hexagonal symmetry in the in-plane geometry cannot be achieved, if the parameter K_3' is completely neglected.

3.2.6 Results for regularly arranged elongated nanoclusters and cluster chains

For the samples with regularly arranged elongated nanoclusters and cluster chains FMR measurements were performed at a temperature of 280 K, where the resonance signal was most pronounced.

Figure 3.10 shows the angular dependence of the resonance fields in out-of-plane and in-plane geometry of the first sample prepared with elongated nanoclusters. As described in section 2.3.5, the sample consists of four different arrangements of nanoclusters, whose major axis is oriented along the $\langle \bar{1}10 \rangle$-direction. The SEM images of the corresponding arrangements are shown on top of figure 3.10. In out-of-plane geometry the elongated nanoclusters exhibit the same behaviour as the nanoclusters with a hexagonal shape. The clearly observable two-fold anisotropy confirms that the magnetization of the elongated nanoclusters is orientated in the sample plane and perpendicular to the c-axis of the nanoclusters. But in contrast to the hexagon-shaped nanoclusters two resonance features can be found in the in-plane geometry.

The first resonance line is very weak and occurs at low resonance fields in the range between 36 and 42 mT. It shows a hexagonal symmetry with minimas for a magnetic field direction parallel to the $\langle \bar{1}\bar{1}2 \rangle$-direction and maximas along the $\langle \bar{1}10 \rangle$-direction of the substrate. Like for the hexagon-shaped nanoclusters the preferred axes of magnetization direction are oriented between the three a-axes of the MnAs nanoclusters in the sample plane. However, two global minimas of the resonance signal can be observed for a magnetic field direction parallel to the $[\bar{1}2\bar{1}]$-direction, i.e. in an angle of 30° and thus almost parallel to the major axes of the elongated nanoclusters. These minimas indicate a small additional two-fold symmetry with an easy axis along this direction leading to a preferred orientation of the magnetization parallel to the elongation direction of the clusters. This 180° anisotropy is caused by the asymmetric shape of the nanoclusters, which forces the magnetization to be oriented along the major axes of the cluster.

The second resonance line shows a stronger resonance signal and can be ob-
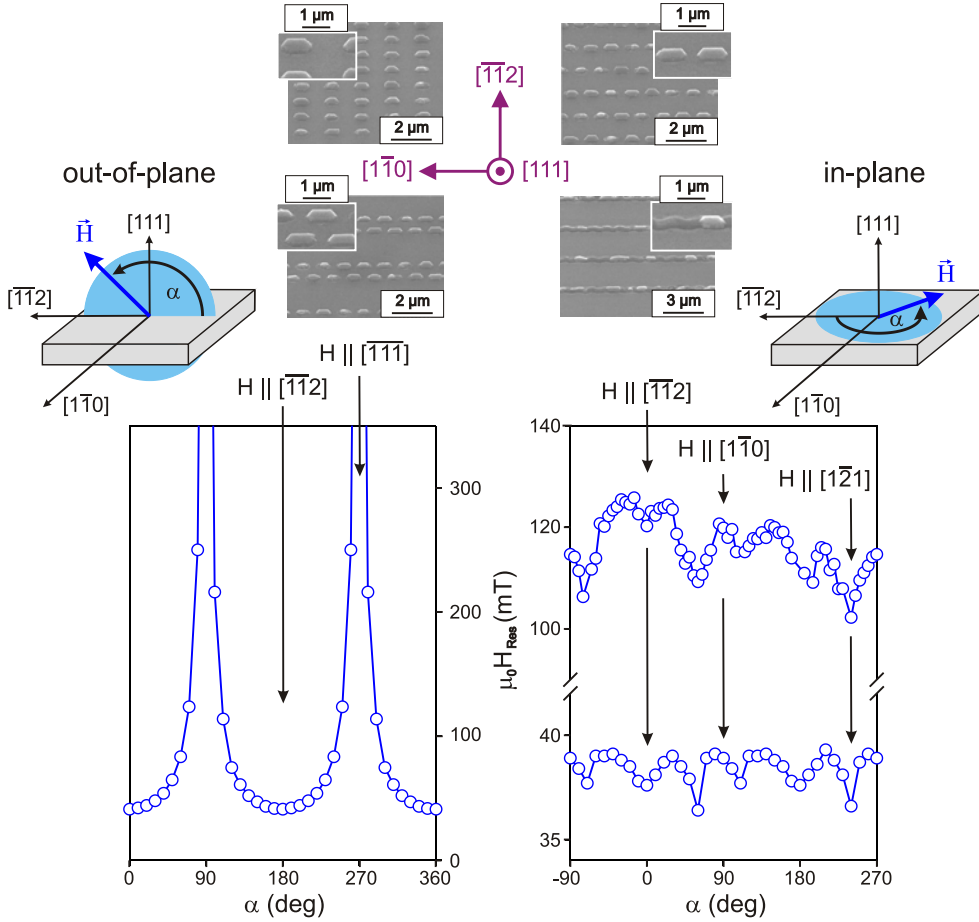
Figure 3.10: Angular dependence of the resonance fields at 280 K in out-of-plane (left) and in-plane (right) geometry of the first prepared sample with regularly arranged elongated nanoclusters on (111)B GaAs substrate. In the in-plane geometry two resonance features are observed, which arise from the single elongated nanoclusters and the cluster chains, respectively.

served at resonance fields between 100 and 120 mT. Like the first resonance feature the second one shows a hexagonal symmetry with local maximas along the a-axes of the nanoclusters. Also the additional two-fold symmetry with an easy axes parallel to the $[\bar{1}2\bar{1}]$-direction can be found. But in contrast to the first resonance line the additional 180° symmetry of the second one is more pronounced exhibiting global maximas along the $[10\bar{1}]$-direction, i.e. perpendicular to the major axis of the elongated clusters. Because of this feature the second resonance line can be attributed to the cluster chains grown along the $[1\bar{1}0]$-direction. The larger aspect ratio of the cluster chains leads to a stronger two-fold anisotropy compared to the 180° anisotropy of the single elongated nanoclusters and therefore their magnetization experiences only one hard magnetic axes perpendicular to the direction of elongation.
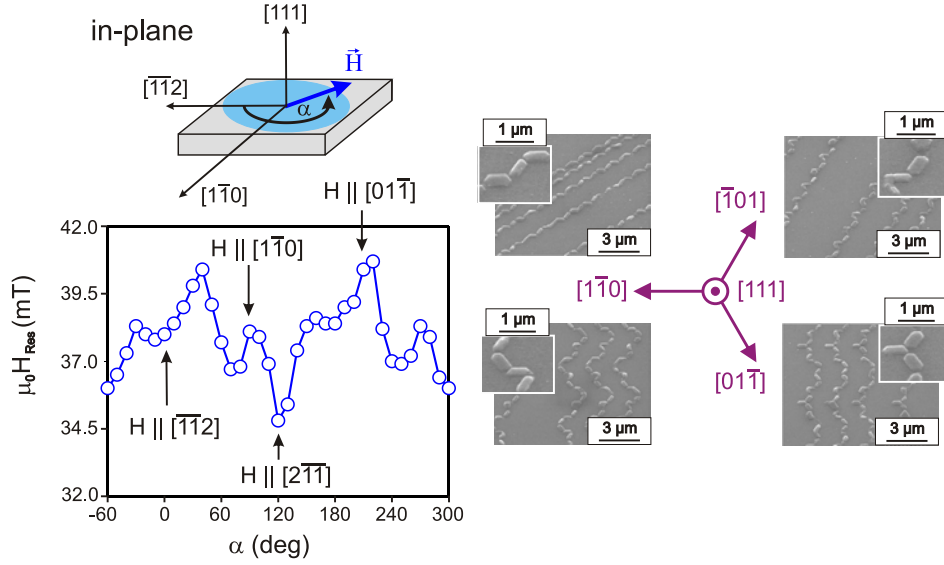
Figure 3.11: Angular dependence of the resonance field at 280 K in in-plane
geometry (left) of the sample with the regularly arranged cluster
chains on (111)B GaAs substrate.

In order to investigate the influence of the cluster arrangement on the magneti-
zation orientation of the elongated nanoclusters in more detail, FMR measure-
ments in in-plane geometry were also performed for the sample with different
cluster chains. The cluster chains on this sample consists of elongated nan-
oclusters whose major axes are oriented along one of the three $\langle 1\bar{1}0 \rangle$-directions.
For the first two arrangements, the major orientation of the cluster chains is
approximately along the $[\bar{1}01]$-direction, while for the other two arrangements,
the cluster chains are oriented parallel to the $[\bar{1}\bar{1}2]$-direction.

The angular dependence of the resonance field obtained as well as the SEM
images of the corresponding cluster arrangements are shown in figure 3.11. The
four different cluster chains show one weak resonance feature, which occurs at
low resonance fields in the range between 34 and 40 mT. Again the chains ex-
hibit a sixfold symmetry with maximas parallel to the a-axes of the nanoclusters
due to their hexagonal crystal structure. But in contrast to the cluster chains
oriented along the $[1\bar{1}0]$-direction the additional two-fold symmetry of the four
different cluster chains shows an easy magnetic axis along the $[2\bar{1}\bar{1}]$-direction.
The hard axis of magnetization is oriented perpendicular to it, i.e. along the
$[01\bar{1}]$-direction.

Although the elongated clusters did not merge during the growth process as
can be seen on the SEM images the small distance between the clusters enables
the cluster's magnetizations to couple. This coupling between the single elon-
gated nanoclusters results in an orientation of the magnetization along along
the $[2\bar{1}\bar{1}]$-direction, i.e. almost along the main direction of the cluster chains.
Therefore the easy and hard axis of magnetization are oriented parallel and
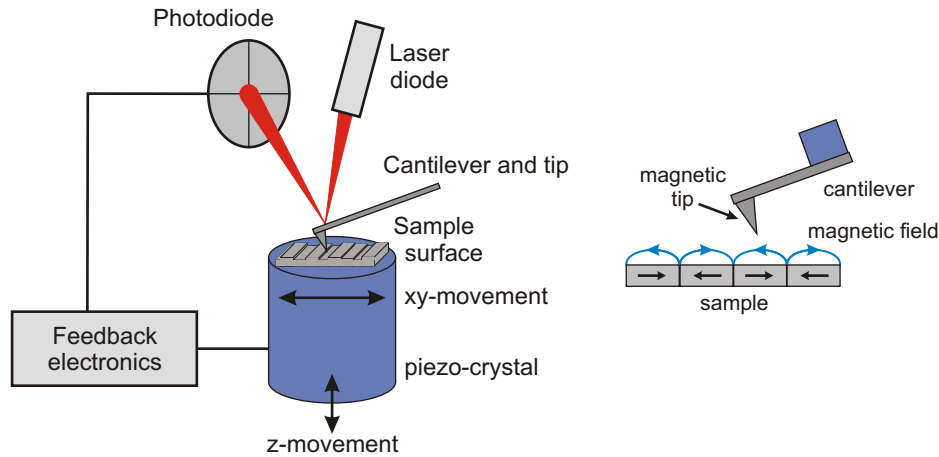perpendicular to this direction, respectively.

Figure 3.12: Schematic scetch of an atomic force microscope (left). The deflection of the tip, which scans over the sample surface, is detected with a photodiode and serves as feedback signal for the piezo crystal. The height information is obtained from the piezo element's z-position. For a magnetic force microcope a magnetic tip is used, which interacts with the magnetic forces of the sample surface (right).

3.3 Atomic and magnetic force microscopy investigations

Atomic force microscopy (AFM) as well as magnetic force microscopy (MFM) are two types of scanning microscopy techniques, which offer the possibility to investigate a sample surface on a microscopic scale [108]. While atomic force microscopy measurements yield information about the height and the shape of the nanoclusters, the MFM measurements are well suitable for the investigation of the magnetic domain structure.

3.3.1 Principle of atomic force and magnetic force microscopy

Shortly after the development of the scanning tunneling microscope (STM) by G. Binning and H. Rohrer in 1982 [109], Binning et al. realized the first atomic force microscope (AFM) [110]. While only conductive surfaces can be imaged by STM, AFM can also be used for the investigation of insulating samples. The main principle of AFM like for all scanning probe microscopy techniques is the scanning over the sample surface with a small tip. The operation principle of an AFM is schematically shown in figure 3.12. In the case of an AFM the tip is mounted on the end of a cantilever and positioned close to the sample surface. The forces, like for example electrostatic forces, van der Waals forces and mechanical forces, which act between the tip and the surface, result in a bending of the cantilever. The bending and therefore the forces acting on the tip are measured by the displacement of the reflection of a laser beam, which is focused on the back of the cantilever [111]. The bending of the cantilever leads

to the displacement of the reflected beam and is detected by a position-sensitive photodetector. The signal obtained is then converted into height information. The sample is mounted on a piezo-crystal, which moves the sample in the xy-plane and also controls the distance in z-direction between sample and tip. The height information obtained from the photodetector serves as feedback signal for a precise movement of the piezo-crystal in z-direction to keep a constant distance between sample surface and tip. Thus, the scanning of the tip over the sample and the changing magnitude of the interactions result in an image of the surface topography. The most important modes of operation are shortly described in the following:

Contact mode
In contact mode the tip and the sample are in direct contact with each other. The forces acting between them are repulsive and lead to a bending of the cantilever, which is detected as feedback signal. The contact mode may be carried out in two different ways. In constant force mode the position of the tip is controlled to achieve a constant force acting on the cantilever in order to obtain the height information, while in constant height mode the tip scans in a constant average distance between sample surface and tip over the surface and detects the deflection of the cantilever.
In general in the contact mode the highest resolution is obtainable. However, due to the direct contact between sample and tip the risk of damaging cannot be eliminated.

Non-contact or dynamic mode
In non-contact mode the tip scans over the sample in a distance of 2 to 200 nm. The tip is mounted on a stiff cantilever, which oscillates near its resonance frequency with an amplitude < 10 nm. The long-range van der Waals forces interact with the tip [112] and therefore influence the oscillation frequency. The changes of the oscillation frequency or the amplitude due to a varying distance between sample surface and tip during the scan are detected and serve as feedback signal for the piezo-crystal. As the attractive forces are typically smaller than the repulsive forces in contact mode, the signal is weaker resulting in a lower sensitivity compared to contact mode.

Semi-contact mode
Semi-contact mode, also called tapping mode, is carried out to avoid damage of the sample and to improve the resolution of the scan compared to non-contact mode. Like in non-contact mode the cantilever oscillates near its resonance frequency, but with a larger amplitude (typically larger than 20 nm). The tip oscillates close to the sample surface, so that the tip lightly touches and lifts off the surface in each oscillation cycle. The tapping on the surface changes the amplitude and the frequency of the oscillation, which are measured to obtain the height information.

Magnetic force microscopy is a variation of atomic force microscopy. For measuring the magnetic properties of the sample, a ferromagnetic tip is used, which interacts with the magnetic forces of the sample surface as schematically shown on the right in figure 3.12. The magnetic interactions, like for example the

atomic force microscopy
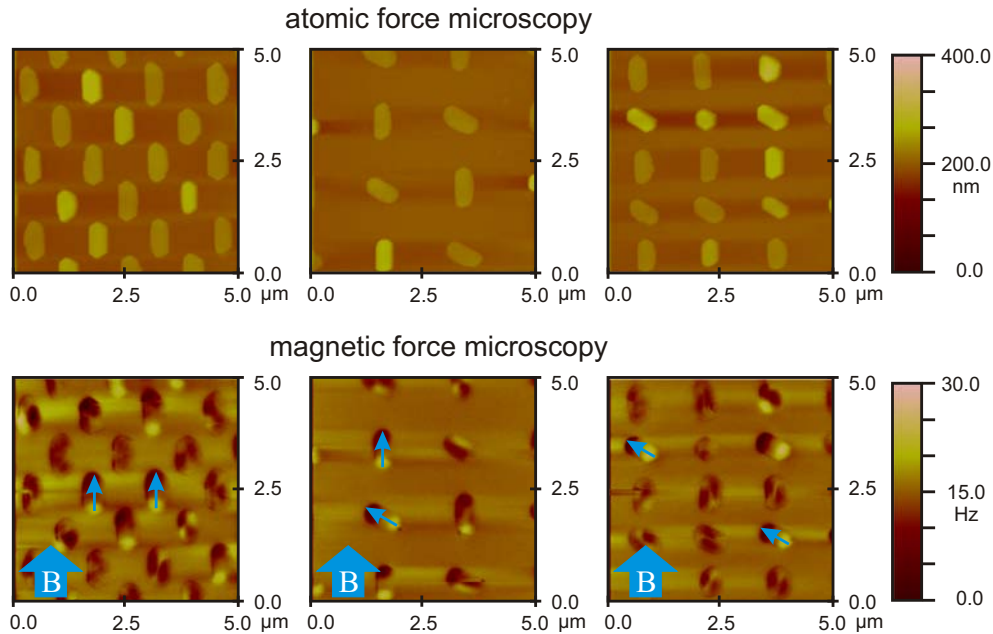

magnetic force microscopy

Figure 3.13: AFM (top) and MFM (bottom) images of arrangements of single elongated nanoclusters. The AFM images show, that MnAs nanoclusters can only be found in the SiO_2 openings. At low fields the magnetization direction of the clusters with a single magnetic domain is nearly always oriented along the major axis of elongation and therefore determined by the shape of the nanocluster.

dipole-dipole interaction, between sample and tip are detected and used in order to obtain an image of the magnetic structure of the surface. Because the tip not only acts on the magnetic forces but also on the atomic and electrostatic forces, at first the topographic profile of the sample surface is measured. This is done by atomic force measurements in tapping mode, where the tip touches the surface of the sample. In the second step the tip is lifted to a larger distance and the sample surface is scanned a second time. Because during this second scan the distance between surface and tip is kept constant the information about the magnetic structures can be extracted from the forces acting on the tip.

AFM and MFM measurements were performed for the samples with single elongated nanoclusters as well as for the sample with arrangements of coupled nanoclusters. Prior to the MFM measurements the samples were exposed to an external magnetic field of 0.35 T in order to align the magnetization of the nanoclusters. During the actual measurements no magnetic field was applied.

3.3.2 AFM and MFM measurements of regularly arranged elongated nanoclusters

Figure 3.13 shows the results of the AFM and MFM measurements for the sample with regular arrangements of single elongated nanoclusters. The large blue

arrow denotes the direction of the external magnetic field, which was applied along the $[1\bar{1}0]$-direction.

The AFM images for the three arrangements investigated confirm, that the clusters are formed by self-assembly only in the SiO_2 openings. On the SiO_2 mask no evidence for the deposition of Mn compounds or the formation of MnAs clusters can be found. The nanoclusters show well-defined crystal facets and a height of around 50 to 100 nm.

On the MFM images one finds, that some nanoclusters exhibit one single magnetic domain. For these clusters the orientation of the cluster's magnetization is denoted with a small blue arrow. The left MFM image shows an arrangement of elongated nanoclusters whose axis of elongation is always oriented along the $[1\bar{1}0]$-direction, i.e. parallel to the external magnetic field of 0.35 T. The magnetization of the nanoclusters with one single magnetic domain is always oriented along the direction of elongation and therefore parallel to the external magnetic field direction.

The MFM images in the center and on the right show arrangements with nanoclusters whose axis of elongation is oriented either along the $[1\bar{1}0]$- or the $[\bar{1}01]$-direction. For the nanoclusters whose direction of elongation is parallel to the $[\bar{1}01]$-direction, a magnetization orientation along the direction of elongation can be found for nearly all clusters with a single magnetic domain, although the magnetic field was applied along the $[1\bar{1}0]$-direction. Therefore at low magnetic fields the orientation of the cluster magnetization seems to be determined by the shape of the nanoclusters and not by the direction of the external magnetic field. These findings confirm the results of the FMR measurements in section 3.2.6, that the asymmetric cluster shape forces the magnetization to be oriented along the major axes of the nanoclusters and that the clusters possess an easy axis of magnetization along this direction.

3.3.3 AFM and MFM measurements of different arrangements of coupled nanoclusters

The AFM and MFM images of three different arrangements of coupled nanoclusters are shown in figure 3.14. The external magnetic field of 0.35 T was applied along the $[\bar{1}\bar{1}2]$-direction.

The left images in figure 3.14 show the AFM and MFM images of the cluster chains oriented along the $[1\bar{1}0]$-direction. As can be seen on the AFM images, not all nanoclusters exhibit well-defined crystal facets. Furthermore the MFM images reveal, that the nanoclusters do not grow entirely regularly in the SiO_2 openings. While the chains seem to be continuous on the AFM image, several discontinuities in the cluster chains can be found on the MFM image. However, the nanoclusters, which merged during the cluster growth, exhibit only one single magnetic domain. The resulting cluster chains show a clear magnetization orientation along the chain direction and perpendicular to the applied magnetic field direction. Like for the single elongated nanoclusters the asymmetric shape of the cluster chains forces the magnetization to be oriented along their direction of elongation.
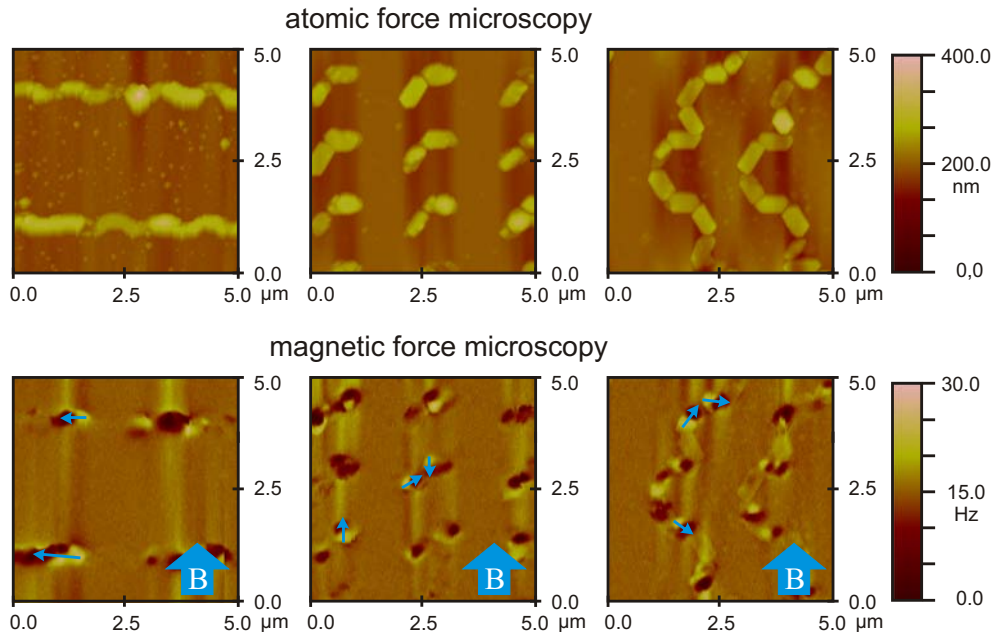
Figure 3.14: AFM (top) and MFM (bottom) images of different arrangements of coupled nanoclusters. The AFM images show, that there are still small gaps between some of the nanoclusters and that the clusters do not grow entirely regularly in the openings.

Also for the coupled nanoclusters of different orientations in the center of figure 3.14, the AFM images show that the nanoclusters are not formed with crystal facets of high quality. Additionally most of the nanoclusters did not merge during the growth. There are still small gaps between the single nanoclusters observable. Most of these single nanoclusters exhibit a single magnetic domain, whose magnetization is again determined by the asymmetric shape of the elongated nanocluster.

On the right images of figure 3.14 the results for the cluster chains oriented along the $[\bar{1}\bar{1}2]$-direction are shown. In contrast to the other two arrangements the single nanoclusters of these chains exhibit well-defined crystal facets. But like for the coupled nanoclusters most of the clusters did not merge during the growth and small gaps between them are clearly visible on the AFM image. Again most of the nanoclusters show a single magnetic domain with a magnetization oriented along the major axes of elongation. Furthermore some single magnetic domain clusters show a magnetization orientation antiparallel to the direction of the external magnetic field. This behaviour indicates a coupling between the clusters' magnetizations due to the small distance between the single nanoclusters in accordance with the FMR measurements as described in section 3.2.6.

Finally, AFM and MFM measurements were performed for the cluster arrangements consisting of one hexagon-shaped and two elongated nanoclusters. The results for the arrangements with a distance of the initial mask openings of 400
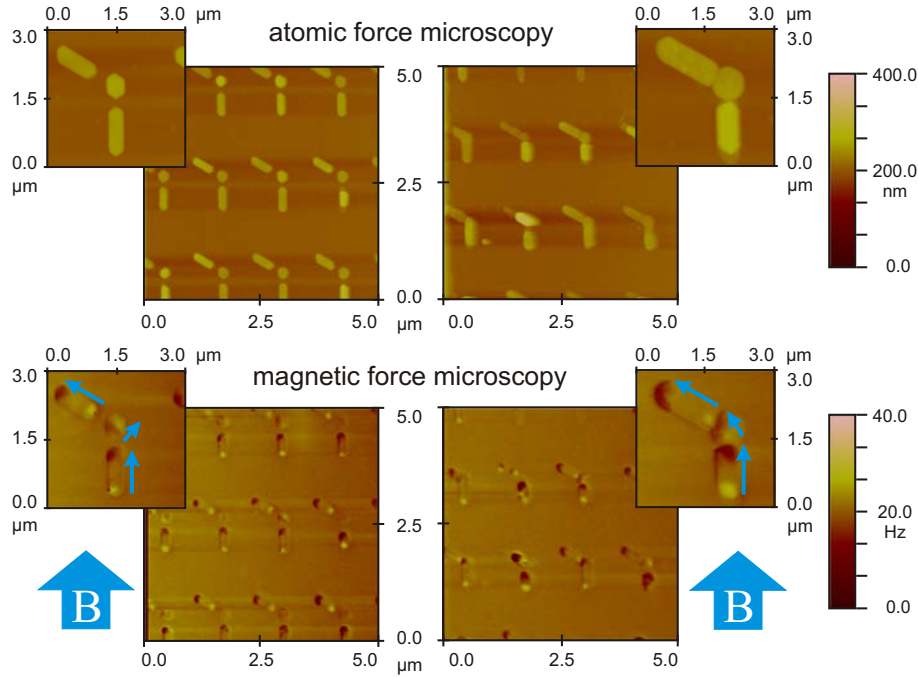
Figure 3.15: AFM (top) and MFM (bottom) images for the structure consisting of two elongated and one hexagon-shaped nanocluster. The distance of the initial mask openings was 400 nm (left) and 75 nm (right), respectively. Nanoclusters of high crystal quality can be found on both arrangements. With decreasing distance between the clusters a magnetic coupling of the clusters' magnetizations can be observed.

and 75 nm are shown in figure 3.15. On both arrangements nanoclusters of high crystal quality with well defined crystal facets are observed. The height of the clusters is about 50 to 100 nm as for all investigated nanoclusters. A merging of the nanoclusters for the arrangement with initial mask openings of 75 nm cannot be observed for all the clusters. Like for the cluster chains consisting of elongated nanoclusters for some of the structures small gaps between the hexagon-shaped nanocluster and the two elongated nanoclusters are still visible.

All elongated nanoclusters on both arrangements exhibit a single magnetic domain with a magnetization orientation along the major axis of elongation. For the arrangement with a distance between the initial mask openings of 400 nm the magnetization of the hexagon-shaped nanoclusters is randomly oriented along one of the three a-axes of the cluster. Reducing the distance between the nanoclusters results in a coupling between the clusters' magnetizations, which can be clearly observed for the arrangement with a distance between the initial mask openings of 75 nm. Although not all clusters merged during the growth, the coupling between the nanoclusters is strong enough to align the magnetization of the hexagon-shaped nanocluster in such a way, that the magnetizations of all three clusters form a chain.

4 Magnetotransport measurements

While ferromagnetic GaMnAs alloys usually exhibit only negative magnetoresistance effects [113, 114, 115, 116], the formation of ferromagnetic MnAs nanoclusters may change the transport properties completely. For example, GaMnAs/MnAs hybrid structures with ferromagnetic nanoscale MnAs clusters prepared by thermal annealing of $Ga_xMn_{1-x}As$ show negative magnetoresistance effects only, whose magnitude strongly depends on the cluster size and their concentration in the matrix [56, 117]. In contrast, for GaMnAs/MnAs hybrids prepared by Mn-ion implantation into GaAs followed by thermal annealing or for hybrids grown by standard MOVPE negative as well as large positive magnetoresistance effects can be observed [8, 118, 119, 120, 121]. In addition, theoretical calculations by Michel et al. have shown, that not only the cluster size and density but also the arrangement of the nanoclusters in the paramagnetic matrix influences the transport properties [11]. Due to these large effects of the nanoclusters on the transport behaviour it is essentiell to investigate the transport properties of ordered cluster arrangements to assess the potential of these structures as possible magnetoelectronic devices.

In the first part of this chapter the experimental set-up used for the investigation of the transport properties is described, while the second part deals with the sample preparation for the measurements. Finally, in the third and the fourth part the results of the transport measurements of the samples with randomly distributed nanoclusters and with different arrangements of regularly arranged nanoclusters, respectively, are discussed.

4.1 Experimental set-up for magnetotransport measurements

The magnetotransport measurements were performed using an Oxford Instruments magnet system. A schematic drawing of the experimental setup is shown in figure 4.1. The sample is mounted on a sample holder which is positioned in a cryostat. Superconducting coils, which are cooled with liquid helium, generate a magnetic field up to 10 T. The helium is also used for cooling the sample. At the same time the sample may be heated with a heater located in the sample space in order to adjust a certain measurement temperature. The heater and therefore the sample temperature is controlled with a temperature controller Oxford ITC 4. This allows a variation of the measurement temperature in the range from $1.6\,\mathrm{K}$ to $290\,\mathrm{K}$. For an accurate determination of the sample temperature a calibrated temperature sensor is placed directly below the sample. The
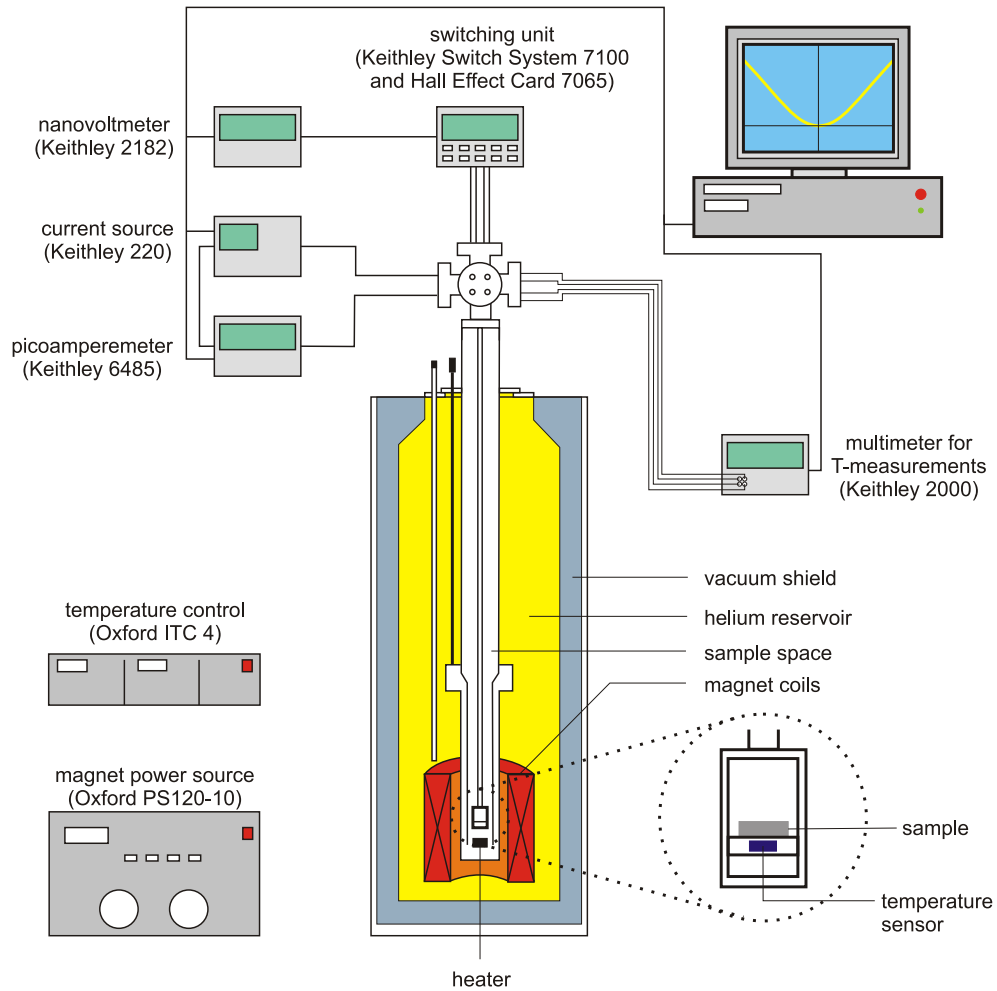
Figure 4.1: Schematic scetch of the setup used for magnetotransport measurements.

resistance of the sensor is measured with the multimeter Keithley DMM 2000 and finally converted into the value of the temperature.

For the measurements Keithley triaxial cables are used in the so-called guarded circuit technique [122] to prevent leackage currents and to guarantee a high signal to noise ratio. The measurements cables are connected to the switching unit Keithley Hall-Card 7065, which possesses excellent signal to noise characteristics. The current for the measurements is generated by the stabilized DC current source Keithley 220. For measuring the current and the voltage the picoammeter Keithley 6485 and the nanovoltmeter Keithley 2182 are used, respectively.

The whole measurement procedure is almost fully automated. A special measurement software controls and monitors all devices. Especially for the magnetic field dependent measurements at a constant temperature, which takes typically up to 3 hours, the software is able to achieve a precise control of the measurement temperature with temperature fluctuations of only $\pm 0.1\,\mathrm{K}$ at

low temperatures. In order to minimize measuring errors due to, for example, thermoelectric effects, the resistance of every measurement point is measured for positive as well as negative current direction. Additionally, the values are averaged for positive and negative fields.

4.2 Sample preparation

In order to perform the transport measurements the various samples prepared were structured by photolithography. For measuring magneto and Hall resistances Hall-bar structures were transferred on to the samples with randomly distributed hexagon-shaped nanoclusters grown on (111)B GaInAs/InP surfaces. Because the squares with regular arrangements of nanoclusters grown on (111)B GaAs surfaces were too small for a Hall-bar geometry, contact pads were prepared on two opposite sides of the squares. The structuring process for both kinds of samples is described in detail in the following.

4.2.1 Hall-bar structuring of the samples with randomly distributed nanoclusters

Prior to the transfer of the Hall-bar structure on to the sample, the surface was cleaned thoroughly with acetone and isopropanol. Positive photoresist was deposited on to the surface using a spin coater, which rotated with $3000\,\mathrm{rpm}$ for $30\,\mathrm{s}$. A pre-bake step on a hot plate at $100\,^{\circ}\mathrm{C}$ was carried out for $90\,\mathrm{s}$. Under a photo mask with the desired Hall-bar structure the resist was exposed to UV light for $12\,\mathrm{s}$ using photolithography. In the following developing step the resist was removed at the unexposed areas on the surface. A hard bake in an oven at $100\,^{\circ}\mathrm{C}$ was carried out for $45\,\mathrm{min}$ in order to stabilize the remaining resist for the transfer of the pattern into the sample, which was done by wet-chemical etching. The complete GaInAs layer was etched off at the bare areas using an etching solution consisting of H_2O, H_3PO_4 and H_2O_2 in parts of 38:1:1 by volume. Finally, in a lift-off step, the remaining resist was removed with acetone. For the preparation of metallic contacts a second photolithography step was carried out, where the resist was removed only at the contact areas. The samples were then evaporated with a $10\,\mathrm{nm}$ thick titanium layer followed by a $100\,\mathrm{nm}$ thick gold layer in order to obtain ohmic contacts. Electrical contact between contact pad and sample socket was achieved by a gold wire attached with a ball-bonder. An optical microscopy image of the prepared Hall-bar structure is shown in figure 4.2.
The large advantage of the Hall-bar geometry is, that due to the structuring the sample geometry is well-known, which is necessary in order to determine the resistivity as well as the carrier concentration of the sample. Additionally, the Hall-bar guarantees, that the Hall voltage is measured always perpendicular to the applied current direction.
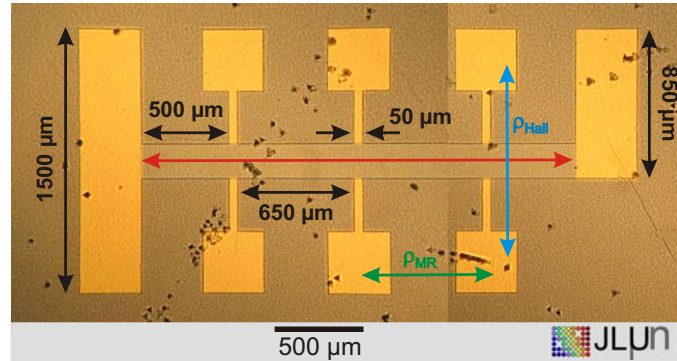
Figure 4.2: Optical microscopy image of the Hall-bar structure used for measuring the transport properties of the samples with randomly distributed nanoclusters. The magnetoresistance is measured between two neighbouring contact pads (green), while the Hall resistance is measured between two opposed pads (blue) perpendicular to the direction of the applied current (red).

4.2.2 Preparation of the contact pads for the samples with regularly arranged nanoclusters

As mentioned above, the $100 \times 100 \,\mu m^2$ large squares with regular arrangements of nanoclusters grown on (111)B GaAs substrates were too small for a Hall-bar geometry. Therefore only two contact pads on opposite sites of a square were prepared in order to apply electrical contact to the squares with different cluster arrangements. The structuring process for transferring the contact pads on to the sample surface was identical to the structuring process of the Hall-bars. The structure prepared is shown in figure 4.3.

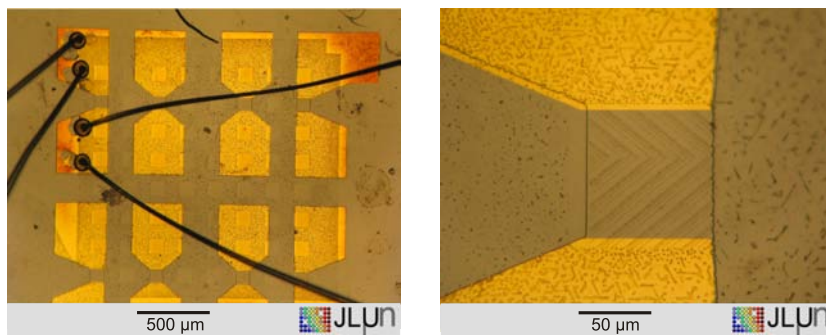Figure 4.3: Optical microscopy image of the contact pads prepared for measuring the transport properties of the single squares with regular arrangements of nanoclusters. The left image shows several squares with contact pads on opposite sides. The cluster arrangement in the left upper corner is contacted using bonded gold wires. The right image shows a magnified imaged of the arrangements with cluster chains.

For the determination of the magnetoresistance a four point probe measurement was carried out, in order to reduce effects of contact resistance. For this purpose each contact pad was connected with two separate gold wires, as can be seen in the left image of figure 4.3. During the measurement, the current was applied between two wires, while the other two wires were used for measuring the voltage drop.

4.3 Influence of a random cluster distribution on the transport properties

The combination of semiconducting and magnetic properties results in a high complexity of the material system. Due to this complexity even fundamental questions like the dominant transport mechanism or the interaction between the clusters and the semiconducting matrix are still under discussion or entirely open. In order to shed some light on the influence of random cluster distributions on the transport properties of the matrix, the transport through the semiconducting GaInAs matrix of all three samples prepared with different densities of randomly arranged, hexagon-shaped nanoclusters was investigated. For this purpose the magnetoresistance behaviour as well as the Hall-resistance were determined for a magnetic field applied perpendicular to the sample surface. Although an undoped GaInAs layer was grown on the InP(111)B wafer, the GaInAs matrices of all three samples show p-type conductivity with almost the same carrier concentration of about $1.7 \times 10^{18} \, \mathrm{cm}^{-3}$ at $280 \, \mathrm{K}$. The reason is, that the Mn provided during the growth process not only leads to the formation of the nanoclusters on the sample surface. It also diffuses into the undoped GaInAs surface, where, in the ideal case, the Mn is incooporated on group III lattice sites as an acceptor [123, 124, 125] resulting in the observed p-conductivity of the matrix. Due to their half-filled inner $3d$ shell the Mn atoms possess a maximal localized magnetic moment of spin $S = 5/2$ [126, 127]. Besides the p-type doping the diffusion of the Mn therefore also leads to a paramagnetic behaviour of the GaInAs:Mn matrix. As will be shown in the following the resulting magnetic interaction between the magnetic moments and the carriers strongly affects the transport properties.

4.3.1 Interaction with an external magnetic field

Applying an external magnetic field to a paramagnetic dilute magnetic semiconductor leads to a Landau quantization and a normal Zeeman splitting of the electronic states, as described in section 1.1.1 and 1.1.2. Additionally, the magnetic field also affects the magnetic interaction between the carriers and the localized magnetic moments of the magnetic ions as well as the interaction between the magnetic ions themselves. The Hamiltonian for describing the complex magnetic interactions in a single-particle picture consisting of a free carrier with spin $\vec{s}$ and magnetic ions with spins $\vec{S}_i$ in an external magnetic

field $\vec{B}$ is usually written as [128]:

$$
\begin{aligned}
\hat{H}_{\text{magn}} \quad = \quad & \hat{H}_{\text{Landau}} + g_0 \mu_{\text{B}} \vec{B} \vec{s} - \sum_i J_{\text{s,p-d}} \vec{S}_i \vec{s} - \\
& - \frac{1}{2} \sum_{i \neq j} J_{\text{d-d}} \vec{S}_i \vec{S}_j + \sum_i g \mu_{\text{B}} \vec{B} \vec{S}_i.
\end{aligned}
\tag{4.1}
$$

The first and the second term of the Hamiltonian describe the diamagnetic Landau quantization and the paramagnetic Zeeman splitting, respectively. The third term denotes the so-called s,p-d-interaction, which describes the exchange interaction between the spin of the free carrier $\vec{s}$ in the s- or p-like energy band with the spins of the localized magnetic moments $\vec{S}_i$ of the d shells. The fourth term considers the magnetic interaction among the localized magnetic moments via direct exchange or superexchange coupling, the so-called d-d-interaction. Finally, the interaction of the magnetic moments with the external magnetic field is described by the last term.

In a paramagnetic dilute magnetic semiconductor the s,p-d interaction may completely dominate the other contributions of the Hamiltonian leading to the so-called giant Zeeman splitting of the corresponding energy levels [128]. Assuming a carrier wave function, which is extended over several Mn lattice site, one may use the mean-field approximation, where the individual spins of the magnetic moments S_i are replaced by the thermal average of the Mn-ion spin $\langle S_z \rangle$ parallel to the magnetic field direction. $\langle S_z \rangle$ is then given by a modified Brillouin function [129, 130, 131]:

$$
\langle S_z \rangle = a S B_S \left(\frac{g \mu_{\text{B}} S B}{k_{\text{B}} (T - \Theta)} \right),
\tag{4.2}
$$

where the Brillouin function $B_S(x)$ is defined according to equation 1.19. The Brillouin function basically depends on the ratio B/T. At low temperatures $\langle S_z \rangle$ increases almost linearly with increasing magnetic field until it reaches its saturation value at $\langle S_z \rangle = 5/2$ (for $a = 1$). With increasing temperature $\langle S_z \rangle$ saturates at higher fields, so that at high temperatures only a linear increase can be found up to large values of B. The dependence of $\langle S_z \rangle$ on the magnetic field for various temperatures is shown in figure 4.4. The Curie-Weiss parameter Θ in equation (4.2) accounts for the exchange coupling between the Mn-ions according to the d-d interaction term in equation (4.1), so that the latter can be discarded in the following. $\Theta < 0$ represents an antiferromagnetic coupling, while for $\Theta > 0$ a ferromagnetic ordering is preferred. Because the Mn ions couple antiferromagnetically due to a strong superexchange interaction [129, 124, 115], the parameter a describes the net reduction of the spin per magnetic ion and one defines an effective concentration of magnetic ions $x_{\text{eff}} = ax$ with $0 < x < a$.

Within the virtual crystal approximation, where the exchange integral is assumed to be independent of the spatial coordinate i, the summation over all lattice sites occupied with Mn-ions can be replaced by the average Mn concentration x_{eff}. Using perturbation theory, the giant Zeeman splitting of the
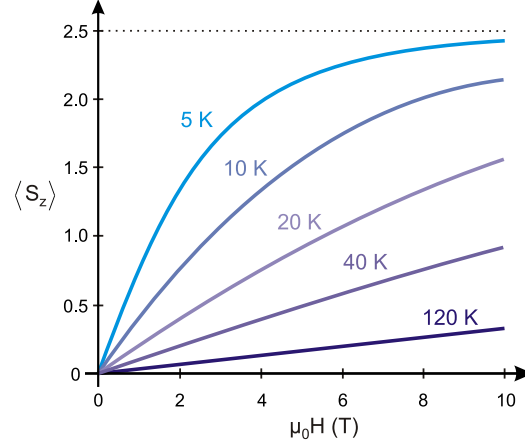
Figure 4.4: Behaviour of the thermal average orientation of the Mn-ion spins $\langle S_z \rangle$ depending on an external magnetic field for different temperatures.

energy bands in a dilute magnetic semiconductor due to the s,p-d interaction at the Γ-point is then given by [128, 132]:

$$\Delta E_{\mathrm{C}} = -N_0 \alpha\, x_{\mathrm{eff}} s_z \langle S_z \rangle, \quad s_z = \pm\frac{1}{2} \tag{4.3}$$

$$\Delta E_{\mathrm{V}} = -\frac{1}{3} N_0 \beta\, x_{\mathrm{eff}} j_z \langle S_z \rangle, \quad j_z = \pm\frac{3}{2}, \pm\frac{1}{2} \tag{4.4}$$

for the conduction band and the valence band, respectively. N_0 is the number of cations per cm^3 and $\alpha = \langle \psi_s | J_{\mathrm{s,p\text{-}d}} | \psi_s \rangle$ and $\beta = \langle \psi_p | J_{\mathrm{s,p\text{-}d}} | \psi_p \rangle$ are the exchange interaction parameters, which give the strength of the magnetic interaction of the Mn-ions with a s-like conduction $|\psi_s\rangle$ and a p-like valence band state $|\psi_p\rangle$, respectively. The giant Zeeman splitting of the heavy and light hole valence bands of a p-type dilute magnetic semiconductor is schematically shown in figure 4.5.

4.3.2 Magnetoresistance behaviour of the samples with a random cluster distribution

The magnetoresistance behaviour of the three samples with randomly distributed hexagon-shaped nanoclusters was determined in the temperature range between 20 K and 280 K. An investigation of the transport behaviour at lower temperatures was not possible due to the strongly increasing resistance of the matrix at low temperatures. The magnetoresistance of all three samples in an external magnetic field applied perpendicular to the sample surface is shown in figure 4.6. All three samples exhibit the same qualitative magnetoresistance behaviour with negative as well as positive magnetoresistance effects.
Figure 4.6 a) shows the magnetoresistance behaviour of the sample with the lowest cluster density of 2.83×10^8 nanoclusters per cm^2. At 10 K, a negative magnetoresistance effect can be observed, which increases up to -20% with
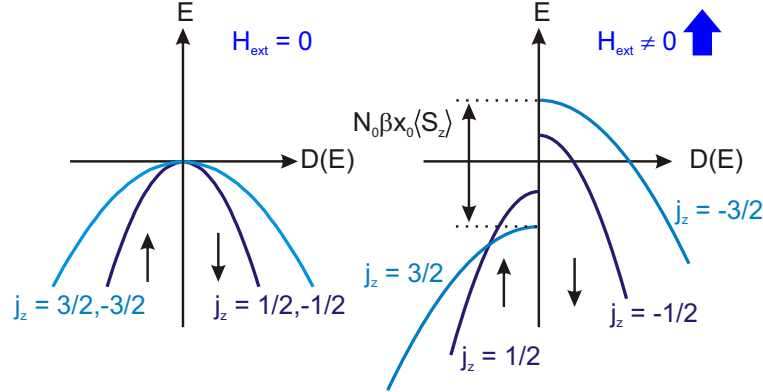
Figure 4.5: Schematic representation of the band structure of a p-type diluted
magnetic semiconductor with (left) and without (right) an external
magnetic field. The two sides in the energy diagram correspond to
different spin orientations.

increasing magnetic field up to 6 T. At higher magnetic fields an additional
positive magnetoresistance contribution occurs which changes the slope of the
magnetoresistance curve resulting in a decrease of the negative magnetoresis-
tance. Increasing the temperature reduces the contribution of the negative
magnetoresistance effect. Therefore, at temperatures above 20 K, only a posi-
tive magnetoresistance effect can be observed, which then dominates the mag-
netoresistance behaviour. The positive magnetoresistance reaches a maximum
of 20% at around 50 K and decreases again for increasing temperatures, but
remains positive up to 280 K.

With increasing cluster density the negative as well as the positive contribution
to the magnetoresistance becomes more pronounced, as can be seen in figure 4.6
b) for the sample with a cluster density of 6.18×10^8 nanoclusters per cm^2. At
20 K the negative magnetoresistance reaches nearly -10% at $\mu_0 H = 10$ T, while
for the sample with the lowest cluster density the positive contribution already
dominates the magnetoresistance behaviour at this temperature. Again the
maximum of the positive magnetoresistance occurs at around 50 K, but com-
pared to the sample with the lowest cluster density the contribution of the
positive magnetoresistance is much stronger and reaches a value of 85%.

For the sample with the highest cluster density of 6.57×10^8 nanoclusters per
cm^2, which is shown in figure 4.6 c), a further increase of the negative mag-
netoresistance effect can be observed, especially at low temperatures. At 20 K
a negative magnetoresistance effect of nearly -40% can be found without any
additional positive contribution even at high magnetic fields. For higher tem-
peratures the sample also exhibits a positive magnetoresistance effect with a
maximum at around 60 K, but compared to the sample with a little lower clus-
ter density of 6.18×10^8 nanoclusters per cm^2, the positive contribution is much
weaker with a maximum magnetoresistance value of 45% at 60 K.
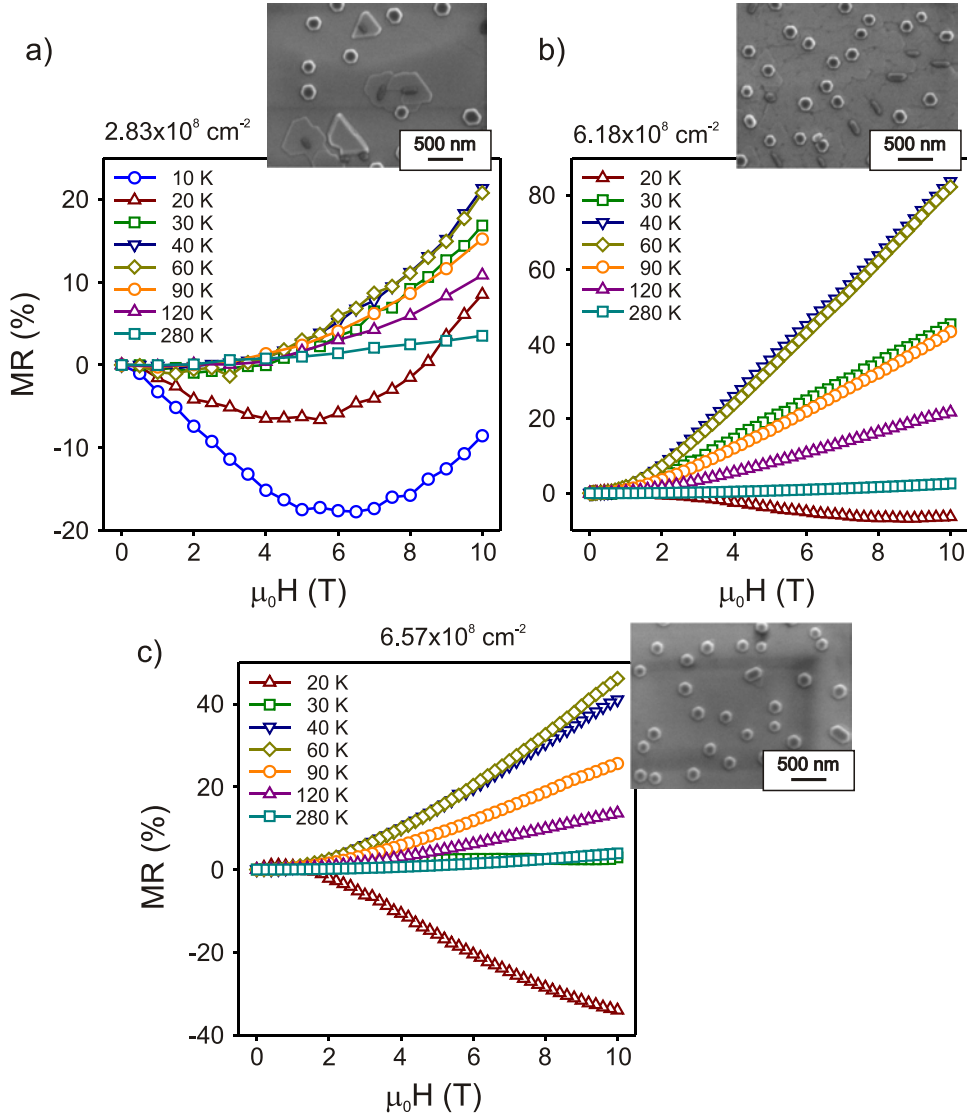
Figure 4.6: Measured magnetoresistance for the three samples with randomly distributed hexagon-shaped nanoclusters in a magnetic field applied perpendicular to the sample surface. The cluster densities are a) 2.83×10^8, b) 6.18×10^8 and c) 6.57×10^8 nanoclusters per cm^2, respectively. All three samples show the same qualitative magnetoresistance behaviour with a negative magnetoresistance effect at low temperatures. With increasing temperature a positive magnetoresistance effect dominates the magnetoresistance and shows a maximum at around 60 K. At high temperatures both effects vanish.

The coexistence and competition of positive and negative magnetoresistance effects are typical and unique for granular paramagnetic-ferromagnetic hybrids [133, 8, 134, 135, 118, 119, 120]. In contrast to the always negative magnetoresistance, which can be found in granular alloys with ferromagnetic

nanoclusters embedded in a diamagnetic matrix [136, 7, 50], the observed effects cannot be explained in the framework of the GMR effect. As described in section 1.3.5, the GMR effect in diamagnetic-ferromagnetic hybrid structures arises from spin-dependent scattering at the interface of the ferromagnetic clusters assuming, that no spin-flip occurs in the diamagnetic matrix. This assumption is not fulfilled for the GaInAs:Mn/MnAs hybrid structures investigated for at least two reasons. Firstly, the scattering at impurities with a large magnetic moment, like the Mn dopands in the matrix, strongly increases the probability of spin-flip [134, 137]. And secondly, the spin relaxation time of a hole in the valence band of a p-type semiconductor is much smaller compared to the spin relaxation time of an electron in the conduction band due to the stronger spin-orbit coupling [138, 139, 140]. Although p-type doping with Mn of the GaInAs:Mn matrix destroys the spin conservation, the resulting paramagnetism plays an important role in the description of the transport mechanisms through the matrix. As will be shown in the following, the observed negative and positive magnetoresistance effects can be explained qualitatively taking into account the magnetic field induced tuning of the band structure of the GaInAs:Mn matrix caused by the giant Zeeman splitting, especially in the vicinity of the ferromagnetic MnAs clusters.

Negative magnetoresistance

The negative magnetoresistance observed at low temperatures for all three samples with randomly distributed nanoclusters can be explained by a trapping of the carriers in the vicinity of the nanoclusters [141, 134, 142, 143]. Even without an external magnetic field the paramagnetic matrix near the clusters is affected by the dipolar field of the ferromagnetic MnAs nanoclusters. This inhomogeneous stray magnetic field leads to a local splitting of the valence bands in the vicinity of the clusters due to the giant Zeeman effect. As schematically shown in figure 4.7 a), this local valence band splitting of the paramagnetic GaInAs:Mn matrix results in a trapping of the carriers at the cluster interface at low temperatures [144] and thus to a depletion of carriers in the matrix.
If an external magnetic field is applied to the hybrid, the valence band splitting due to the giant Zeeman effect occurs globally in the entire paramagnetic matrix, as schematically shown in figure 4.7 b). Because of the cluster field, the Brillouin function almost reaches its saturation value in the vicinity of the clusters while in the other regions of the matrix the band splitting increases at first linearly with increasing external magnetic field. Therefore the depth of the trapping potential at the cluster interface decreases, which leads to a release of the carriers into the GaInAs:Mn matrix. Applying an external magnetic field therefore increases the carrier density in the matrix yielding the observed negative magnetoresistance at low temperatures.
With increasing temperature the giant Zeeman splitting of the valence bands decreases following the Brillouin function, shown in figure 4.4, and the depth of the trapping potential at the cluster interface decreases. Additionally, due to their increasing thermal energy, the holes are released more easily from the trap than at low temperatures. The increase in temperature therefore reduces
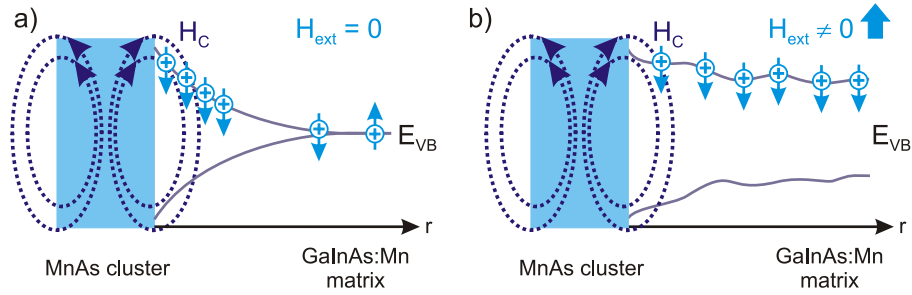
Figure 4.7: Possible origin of the observed negative magnetoresistance effect. a) Even without an external magnetic field the paramagnetic matrix experiences the dipolar field H_C in the vicinity of the ferromagnetic cluster. The resulting local band splitting yields a trapping of the carriers. b) Applying an external magnetic field leads to a splitting of the bands in the entire paramagnetic matrix. The carriers are released resulting in a negative magnetoresistance.

the trapping effects at the cluster interface and results in a break down of the respective negative magnetoresistance effect with increasing temperature.

Not only the external magnetic field, but also a possible formation of a Schottky barrier due to the half-metallic character of the MnAs clusters [80, 145] may lead to a localization of the carriers at the cluster interface [56, 142, 143]. A Schottky barrier, named after W. Schottky, who investigated metal-semiconductor contacts [146], may be formed, if a metal and a semiconductor with different Fermi energies are brought into contact. This is schematically shown in figure 4.8 for a half-metallic cluster and a p-type semiconductor matrix for the ideal case, e.g. in the absence of surface/interface states. In order to equalize the different Fermi levels of the two materials, electrons diffuse from the semiconducting matrix into the cluster, which leads to a band bending at the cluster-matrix interface and to a trapping of the holes in the vicinity of the cluster. Applying a magnetic field results in a giant Zeeman effect-induced valence band splitting in the matrix, as described above. This splitting may be larger than the value of the Schottky-barrier, resulting in a release of the carriers and therefore in a negative contribution to the magnetoresistance.

Because the negative magnetoresistance arises from the influence of the cluster on the band structure of the matrix, an increase of the cluster density results in an increase of the negative contribution to the magnetoresistance. This is observed in the magnetoresistance behaviour of the three samples investigated, where the sample with the highest cluster density shows the largest negative magnetoresistance effect.

Positive magnetoresistance

The positive contribution to the magnetoresistance can be explained qualitatively, if different majority and minority carriers for the half-metallic clusters and the paramagnetic matrix are assumed [71, 134, 147]. The corresponding
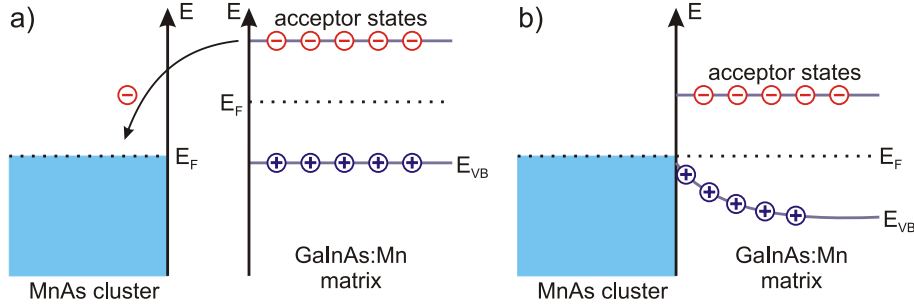
Figure 4.8: Schematic illustration of the formation of a Schottky barrier at the cluster-matrix interface. a) Due to the different Fermi levels it comes to a charge flow, if the two materials are brought into contact. b) After the equilization of the Fermi energy, a Schottky barrier is formed, which leads to a trapping of the carriers in the vicinity of the cluster.

band structure of a MnAs cluster embedded in the p-type doped GaInAs:Mn matrix is schematically shown in figure 4.9. Due to the ferromagnetism of the cluster, its spontaneous magnetization results in a splitting of the cluster's band structure even in the absence of an external magnetic field. The Fermi energy E_F is energetically located in one spin subband because of the half-metallic character of the cluster.

In the absence of an external magnetic field, the occupation numbers for both spin orientations in the matrix are equal. Therefore, only one spin orientation of the carriers can pass the MnAs cluster via the majority band due to the high spin polarization of the cluster at the Fermi energy, while the carriers with the opposite spin orientation have to avoid it. This means, that without an external magnetic field, there is a preferential spin orientation for the carriers passing through the ferromagnetic cluster. In the matrix the spin-flip scattering at the randomly oriented Mn spins destroys the information about the spin orientation because the mean distance between the clusters is much larger than the mean spin-flip length.

Applying an external magnetic field completely changes the situation, as shown in figure 4.9 b). Due to the giant Zeeman splitting of the valence bands, the hole spins are aligned in the entire matrix causing different occupation numbers for the two spin orientations. Therefore the transport through the matrix is mainly carried by holes of one spin orientation. Additionally, the magnetization of the cluster will be oriented along the magnetic field direction. If the cluster and the matrix exhibit majority carriers of different spin orientation, the alignment of the cluster favours the hole-spin orientation which is opposite to the spin orientation of the majority carriers in the GaInAs:Mn matrix. The holes in the matrix now have to pass the cluster via its minority band or they have to avoid it and stay in the majority band of the matrix, which increases the length of the current path. Applying a magnetic field therefore suppresses the carrier transport through the cluster, resulting in a positive magnetoresistance effect.
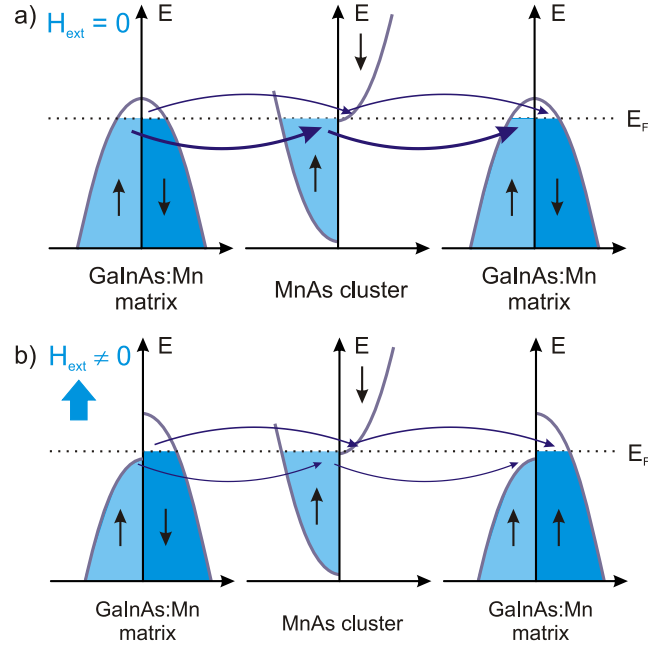
Figure 4.9: Schematic representation of the band structure of a ferromagnetic MnAs cluster embedded in the paramagnetic GaInAs:Mn matrix. a) In the absence of an external magnetic field, one spin orientation of the holes in the matrix can pass through the majority band of the ferromagnetic cluster. b) In an external magnetic field, the degeneracy of the valence bands of the matrix is lifted. Because of different majority spins of cluster and matrix, the majority holes of the matrix cannot pass the majority bands of the cluster anymore yielding a positive magnetoresistance effect.

With increasing temperature the giant Zeeman effect-induced splitting of the valence bands and therefore the preferential alignment of the hole spins in the paramagnetic matrix breaks down, because thermal disorder destroys the orientation of the Mn-spins along the external magnetic field direction. The positive contribution to the magnetoresistance therefore vanishes with increasing temperature in accordance with the results for all three samples investigated. The linear dependence of the positive magnetoresistance, which can be observed especially for the two samples with a higher cluster density at around 60 K, arises from the linear behaviour of the Brillouin function and therefore of the linear increase of the valence band splitting at these temperatures.

The maximum in the temperature-dependence of the magnetoresistance at $\mu_0 H = 10\,\text{T}$, which occurs between 50 and 60 K for all three samples, results from the competition between the negative and the positive contribution to the magnetoresistance. At low temperatures the negative contribution dominates the transport behaviour due to the local valence band splitting even without an external magnetic field, while with increasing temperature the positive magnetoresistance becomes dominant. At high temperatures both effects vanish as

the giant Zeeman splitting in the matrix breaks down, yielding the observable maximum in the magnetoresistance behaviour.

4.3.3 Anisotropy of the magnetoresistance effects

Angle-dependent measurements of the magnetoresistance were performed for different orientations of the external magnetic field. For this purpose a sample holder was used, which can be rotated in steps of $15°$ with respect to the direction of the applied magnetic field. The magnetoresistance was measured for two different geometries, which are schematically shown in figure 4.10 d). In the first geometry, the sample was rotated about the $[\bar{1}\bar{1}2]$-direction resulting in a rotation of the magnetic field in the $(\bar{1}\bar{1}2)$-plane. In this geometry, an angle of $\alpha = 0°$ corresponds to $\vec{H}||[1\bar{1}0]$. Because for $\alpha = 0°$ the magnetic field is oriented parallel to the current direction, measurements in this geometry will be called in the following measurements for a magnetic field orientation parallel to the current direction. In the second geometry, the magnetic field was rotated perpendicular to the current direction in the $(1\bar{1}0)$-plane and for an angle $\alpha = 0°$ the magnetic field is oriented parallel to the $[\bar{1}\bar{1}2]$-direction. In both geometries $\alpha = 90°$ denotes the direction of the magnetic field perpendicular to the sample plane.

The results of the angle-dependent magnetoresistance measurements for all three samples with a random cluster distribution are presented in figure 4.10, where the magnetoresistance at $\mu_0 H = 10\,\text{T}$ is plotted versus the angle α between the magnetic field direction and the sample plane. The solid lines with the open symbols denote the measurements for a magnetic field rotation parallel to the current direction and the dashed lines with filled symbols represent the results for a rotation of the magnetic field perpendicular to the current direction.

Figure 4.10 a) shows the angle-dependent measurements of the sample with the lowest cluster density of 2.83×10^8 nanoclusters per cm^2 for a magnetic field direction parallel to the current direction. For all temperatures the magnetoresistance exhibits no clear angular dependence, i.e. the magnetoresistance effects are almost isotropic. For the other two samples with larger cluster densities of 6.18×10^8 and 6.57×10^8 nanoclusters per cm^2, which are shown in figure 4.10 b) and c), respectively, a clear angular dependence of the magnetoresistance is observable. For both samples, the positive contribution to the magnetoresistance in the intermediate temperature range is largest, if the magnetic field is oriented perpendicular to the sample plane and decreases with decreasing angle α. For an orientation of the magnetic field in the sample plane, i.e. $\alpha = 0°$, the positive magnetoresistance reaches its minimum value. A different behaviour of the negative magnetoresistance effect at low temperatures can be found for the two samples with the higher cluster densities. For the sample with the cluster density of $6.18 \times 10^8\,\text{cm}^{-2}$, the negative magnetoresistance increases with decreasing α. In contrast, the sample with the highest cluster density of $6.57 \times 10^8\,\text{cm}^{-2}$ shows the largest negative magnetoresistance for a magnetic field oriented perpendicular to the sample plane, which decreases with decreasing α. For both
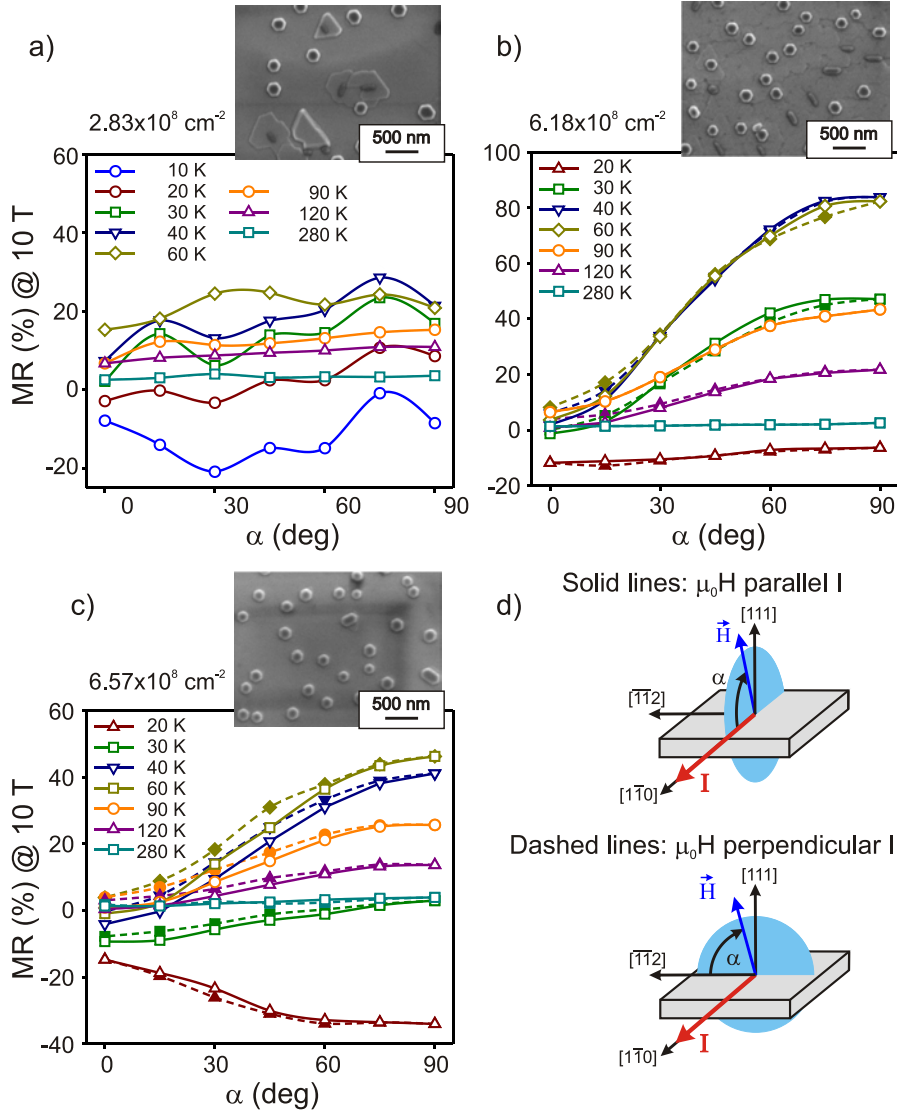
Figure 4.10: Angular dependence of the magnetoresistance for the samples with randomly distributed nanoclusters. Solid lines and dashed lines denote the rotation of the magnetic field in the $[\bar{1}\bar{1}2]$- and $[1\bar{1}0]$-direction, respectively, as schematically shown in d). A nearly isotropic behaviour can be found for the sample with the lowest cluster density a), while the samples with a higher cluster density b) and c) exhibit a strong out-of-plane anisotropy of the magnetoresistance behaviour.

samples the magnetoresistance behaviour is found to be independent of the rotation of the magnetic field parallel or perpendicular to the current direction. Only very small differences in the magnetoresistance can be observed for these two rotation directions. The magnetoresistance therefore shows an isotropic behaviour in the sample plane, but a large anisotropic behaviour in out-of-plane geometry.

The observed anisotropy of the magnetoresistance effects may arise from the
strain in the GaInAs:Mn matrix, which results from the different lattice con-
stants of the matrix and the InP substrate. The lattice constant of the matrix
with an In content of around 30 % [63] can be estimated using Vegard's law [148].
The matrix therefore has a larger lattice constant of approximately 5.9368 Å
[149] compared to the InP substrate with a lattice contstant of 5.8687 Å [150],
leading to biaxial tensile strain in the GaInAs matrix along the growth direc-
tion [151]. The biaxial strain in the matrix results in a quantization direction
of the light and heavy holes parallel to the growth direction and perpendicular
to the sample plane. As a consequence the degeneracy of the light and heavy
hole valence bands at the Γ-point is lifted even in the absence of an external
magnetic field.

If an external magnetic field is applied along the [111]-direction, i.e. perpendicu-
lar to the sample plane, the quantization direction due to the magnetic field
coincide with the quantization direction caused by the biaxial strain in the ma-
trix. Choosing the z-direction parallel to the [111]-direction, the corresponding
Hamiltonian for describing the magnetic-field induced splitting of the four va-
lence band subbands in the $|j, j_z\rangle$ representation after Ref. [152] can be written
as [153, 154]:

$$H_{\vec{H}||z} = \begin{pmatrix} E_{\mathrm{hh}} + 3\Omega & 0 & 0 & 0 \\ 0 & E_{\mathrm{lh}} + \Omega & 0 & 0 \\ 0 & 0 & E_{\mathrm{lh}} - \Omega & 0 \\ 0 & 0 & 0 & E_{\mathrm{hh}} - 3\Omega \end{pmatrix}, \qquad (4.5)$$

where E_{hh} and E_{lh} are the energies of the heavy and light hole band at
the Γ-point in the absence of an external magnetic field, respectively, and
$\Omega = |\frac{1}{6} N_0 \beta x \langle S_z \rangle|$ denotes the contribution of the giant Zeeman splitting.

If the magnetic field is applied in the sample plane, i.e. perpendicular to the
growth direction, it comes to a competition between the perturbations due
to the strain and the magnetic field. Strain alone would yield a quantization
perpendicular to the sample plane, while the sole presence of the magnetic
field results in a quantization direction in the sample plane, e.g. along the
x-direction. Because of the different quantization directions, the matrix rep-
resentation of the corresponding Hamiltonian has off-diagonal elements and is
given by [153, 154]:

$$H_{\vec{H}\perp z} = \begin{pmatrix} E_{\mathrm{hh}} & \sqrt{3}\Omega & 0 & 0 \\ \sqrt{3}\Omega & E_{\mathrm{lh}} & 2\Omega & 0 \\ 0 & 2\Omega & E_{\mathrm{lh}} & \sqrt{3}\Omega \\ 0 & 0 & \sqrt{3}\Omega & E_{\mathrm{hh}} \end{pmatrix}. \qquad (4.6)$$

The competition between the two quantization directions leads to a mixing of
the light and heavy hole valence bands with increasing magnetic field [153]. As
a consequence the magnetic-field induced splitting of the valence band subbands
is reduced. Additionally the eigenstates of the Hamiltonian are linear combi-
nations of both spin orientations. Therefore the electronic states of the carriers
in the matrix exhibit contributions of both spin orientations, so that they can

partly pass the MnAs nanoclusters for a magnetic field orientation in sample plane. In this case the influence of the nanoclusters on the transport path is less pronounced, compared to a magnetic field orientation perpendicular to the sample plane, where the carriers in the majority band cannot pass the clusters. The reduced giant Zeeman splitting as well as the mixing of the valence band subbands therefore results in a reduction of the magnetoresistance effects for a rotation of the external magnetic field direction into the sample plane. The anisotropy of the magnetoresistance can only be observed for the samples with a high cluster density, where the clusters have a strong influence on the transport path. Because the current path is hardly affected by the clusters in the case of the sample with the lowest cluster density, only a weak and nearly isotropic magnetoresistance behaviour can be observed.

4.3.4 Comparison with theoretical calculations

Based on the considerations described above to explain the negative and positive magnetoresistance effects, C. Michel at al. developed a network model for simulating the magnetoresistance behaviour of paramagnetic-ferromagnetic hybrid structures. The basic idea of the network model is to divide the crystal into several cells described by a local resistance. The total resitivity of the crystal is calculated using Kirchhoff's equations. The main advantage of this approach is, that the network model allows one to account for the spatial disorder and the local magnetic field induced tuning of the bandstructure caused by the Zeeman splitting. The MnAs nanoclusters can be inserted into the network model just by adjusting the resistance of the corresponding cells. A detailed description of the network model can be found in Refs. [117, 155, 147].

The experimental results of the magnetoresistance at $\mu_0 H = 10\,\mathrm{T}$ plotted versus temperature for the three samples with the randomly distributed hexagon-shaped nanoclusters are shown on the left of figure 4.11. In order to compare the experiment with theory, several calculations of the magnetoresistance were performed for different cluster densities and various cluster distributions. Representative results of the calculated magnetoresistance behaviour at $10\,\mathrm{T}$ plotted versus temperature are depicted on the right image of figure 4.11. All calculations were carried out for an external magnetic field applied perpendicular to the sample plane. Comparison between theory and experiment shows, that under the assumptions made in order to explain the observed behaviour, a good qualitative agreement between calculations and measurements can be achieved. Like in the experiment the calculations show a negative magnetoresistance at low temperatures and a large positive magnetoresistance in the intermediate temperature range, which vanishes with increasing temperature.

Furthermore, the theoretical calculations reveal, that the magnetoresistance effects are strongly influenced by the cluster distribution and the cluster density. The dependence of the magnetoresistance effects on the cluster distribution is reflected in the curves (a) and (b) of figure 4.11, which show the magnetoresistance of two different cluster arrangements in a model system of 50×50 cells with a cluster density of $x_C = 22\,\%$ and six randomly distributed nanoclusters. For
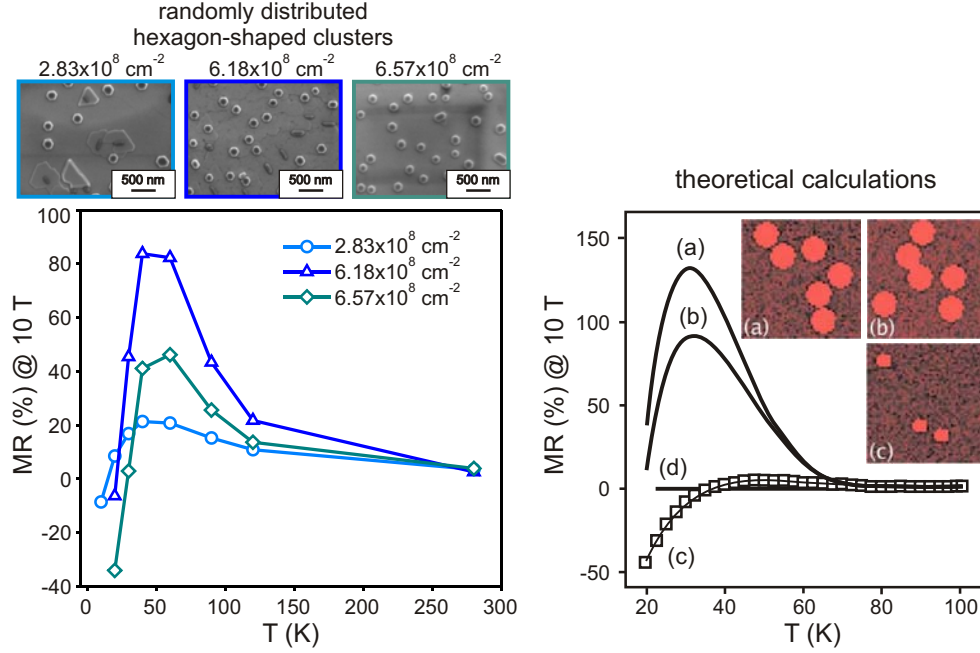
Figure 4.11: Experimental results for the three samples with randomly distributed hexagon-shaped nanoclusters (left) and theoretical calculations (right) from Ref. [11] of the magnetoresistance at $\mu_0 H = 10\,$T plotted versus temperature. The calculations show, that the magnetoresistance strongly depends on the cluster distribution (a),(b) and the cluster density (c), which is in qualitative agreement with the measurements. Curve (d) shows the calculations for a GaMnAs alloy without clusters.

the calculations only the spatial arrangement of the clusters was varied, while all other material parameters were kept constant. The corresponding arrangements of the clusters are shown in the inset of the left image in figure 4.11. The two random cluster distributions show a large difference of the maximum values of the positive magnetoresistance due to the different transport paths through the structure. While arrangement (a) shows a positive magnetoresistance of about 130 % in the intermediate temperature regime, the magnetoresistance of arrangement (b) only reaches a maxmimum value of about 90 % at the same temperature. Therefore, already a minor rearrangement of the nanoclusters can result in significant variations of the magnitude of the magnetoresistance. This strong dependence of the cluster distribution on the transport path and therefore on the magnetoresistance behaviour may explain the lower positive magnetoresistance of the sample with the highest cluster density of $6.57{\times}10^8$ nanoclusters per cm^2 compared to the sample with a lower cluster density of $6.18{\times}10^8$ nanoclusters per cm^2.

Decreasing the cluster density also strongly influences the magnetoresistance behaviour of the hybrid structures. Curve (c) in figure 4.11 shows the calculated magnetoresistance for a cluster density of $x_C = 3.5\,\%$ and three randomly
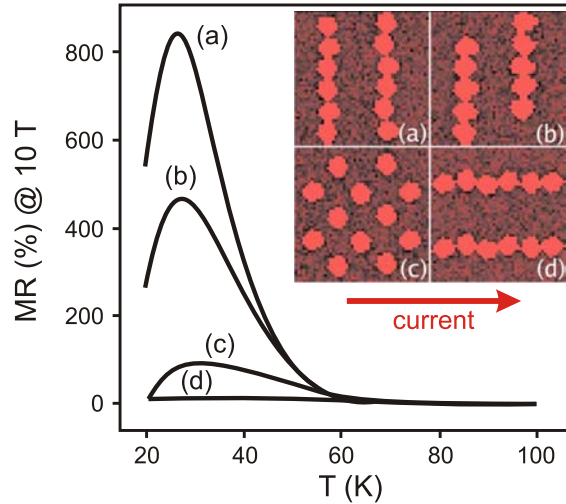
Figure 4.12: Theoretical calculations from Ref. [11] of the magnetoresistance at $\mu_0 H = 10\,\text{T}$ versus the temperature for four regular arrangements of nanoclusters, shown in the inset. Blocking the current path by cluster rows perpendicular to the current direction results in large positive magnetoresistance effects (arrangement (a)). For cluster rows arranged parallel to the current direction, the main current path is not affected by the clusters (arrangement (d)).

distributed nanoclusters. At low cluster densities the dependence of the cluster arrangements on the magnetoresistance behaviour is less pronounced, because the main current path through the hybrid is usually not affected by the clusters. Therefore only a negative contribution to the magnetoresistance can be found due to the trapping effects at the interface between cluster and matrix, which is also in agreement with experimental results [56, 117].

4.3.5 Theoretical predictions for regular arrangements of nanoclusters

Michel at al. not only investigated the magnetotransport properties of hybrids with randomly distributed nanoclusters, but also calculated the magnetoresistance for different regular arrangements of the ferromagnetic nanoclusters in the paramagnetic matrix [11]. The results for the magnetoresistance at $\mu_0 H = 10\,\text{T}$ plotted versus temperature for four different regular arrangements of the ferromagnetic nanoclusters in the paramagnetic matrix are shown in figure 4.12. For all four cluster arrangements the cluster density was $x_\text{C} = 22\,\%$ and the current was applied from left to right, as indicated in the figure. Arrangement (a), where the clusters are arranged in two lines perpendicular to the current direction, shows the largest positive magnetoresistance effect, which reaches a value of nearly 850\,%. The magnetoresistance is about a factor of 8 larger than for a typical random cluster distribution represented by arrangement (c), which

shows a maximum value of the positive magnetoresistance of about 100 %. The arrangement of the clusters in two rows perpendicular to the current direction, which are extended over the entire matrix, nearly completely blocks the current path through the hybrid yielding the large increase of the positive magnetoresistance. Just by removing one clusters of each row at opposite sites results in a decrease of the magnetoresistance to a value of 500 % due to a resulting current path through the matrix. For the opposite arrangement, where the clusters are arranged in two rows parallel to the current direction as shown in (c), nearly no positive magnetoresistance is observable. In this case the main current path, which passes through the matrix, is not affected by the ferromagnetic nanoclusters. The scaling of the magnetoresistance therefore arises solely from the different cluster arrangements as all other parameters were kept constant in the calculations.

4.4 Influence of regularly arranged elongated MnAs clusters and chains on the transport properties

As shown by the theoretical calculations, the large influence of the cluster arrangement on the transport paths leads to significant variations in the magnitude of the magnetoresistance effects. This offers the possibility to actively tune the magnetoresistance by a controlled positioning of the cluster in the matrix. Therefore the new method of self-assembled growth of MnAs nanoclusters on pre-patterned (111)B GaAs substrate may have the potential to optimize the transport properties of the paramagnetic-ferromagnetic hybrids for possible magnetoelectronic applications.

In order to test the theoretical predictions magnetotransport measurements were performed for different arrangements of nanoclusters prepared. Unfortunately, a determination of the Hall-resistance and therefore of the carrier density in the matrix was not possible due to the preparation of only two contact pads for each cluster arrangement. However, like in the case of the samples with randomly distributed nanoclusters, the transport through the matrix is probably carried by holes provided by Mn atoms acting as acceptors, which diffuse into the semi-insulating (111)B GaAs substrate during the growth of the MnAs clusters in the SiO_2 openings.

4.4.1 Magnetotransport measurements of regular arrangements of elongated nanoclusters and cluster chains

The magnetoresistance of the samples with regular arranged nanoclusters and cluster chains was investigated for three different arrangements, one arrangement with regularly arranged isolated elongated nanoclusters and two different arrangements with cluster chains. The measurements were performed in the temperature range from 15 K to 280 K. Like in the case of the samples with randomly distributed nanoclusters a determination of the transport properties

at lower temperatures was not possible due to the increasing resistivity of the matrix, which was even one order of magnitude larger than for the samples with randomly distributed nanoclusters. This strong increase of the resistivity is likely due to the different fabrication processes of the two sample series. In the case of the samples with randomly distributed hexagon-shaped nanoclusters, the clusters grow self-assembled on the untreated GaInAs surface. During their growth, Mn can diffuse into the GaInAs matrix on the entire surface. For the samples with regular arrangements of nanoclusters and cluster chains the SiO_2 mask layer inhibits a diffusion of Mn into the GaAs matrix. During the growth of the MnAs nanoclusters, Mn can only diffuse into the GaAs substrate at the openings, leading overall to a much lower Mn concentration in the matrix and therefore to a larger resistivity than for the samples with randomly distributed nanoclusters.

Figure 4.13 a) shows the results of the magnetoresistance measurements of the sample with regularly arranged elongated nanoclusters, while the magnetoresistance for the samples with cluster chains oriented along the $[\bar{1}10]$-direction and the $[\bar{1}01]$-direction can be found in figure 4.13 b) and c), respectively. The direction of the current applied along the $[\bar{1}\bar{1}2]$-direction is represented by a red arrow next to the SEM image of the corresponding cluster arrangement.

All three cluster arrangements exhibit a positive magnetoresistance at low temperatures. As shown in figure 4.13 a), for the sample with regularly arranged elongated nanoclusters a strong positive magnetoresistance effect can be observed at 15 K, which increases up to 3.5 T to a value of 600 %. At 3.5 T an additional negative magnetoresistance contribution occurs, which changes the slope of the magnetoresistance curve. However, the positive magnetoresistance dominates in the entire magnetic field range and shows a further increase with increasing field reaching a value of 1400 % at $\mu_0 H = 10$ T. The same qualitative behaviour can be found for the arrangement with cluster chains oriented along the $[\bar{1}10]$-direction, i.e. perpendicular to the direction of the applied current, as shown in figure 4.13 b). For this arrangement, which is called in the following cluster chains I, the magnetoresistance reaches a value of 400 % at 3.5 T and of nearly 900 % at $\mu_0 H = 10$ T. A similar bending of the slope at 3.5 T can also be observed in the magnetoresistance behaviour of the second arrangement with cluster chains, shown in figure 4.13 c). However, for this arrangement, where the cluster chains are oriented along the $[\bar{1}01]$-direcion, the magnetoresistance only reaches a value of 70 % at 3 T and remains nearly constant for higher magnetic fields. Only a small increase to 85 % at 10 T can be observed. This arrangement is called in the following cluster chains II.

At a slightly increased temperature of 20 K the bending in the slope and therefore the negative contribution to the magnetoresistance completely vanishes for all three arrangements. Only a large linear positive magnetoresistance can be observed, which reaches values of 600 %, 400 % and 300 % at $\mu_0 H = 10$ T for the arrangement with elongated nanoclusters and the cluster chains I and II, respectively. With further increasing temperature, the positive magnetoresistance rapidly decreases resulting in a value of just 5 % to 30 % at 30 K, depending on the cluster arrangement. Above 30 K, the magnetoresistance of all three arrangements investigated exhibits the same qualitative behaviour as the samples
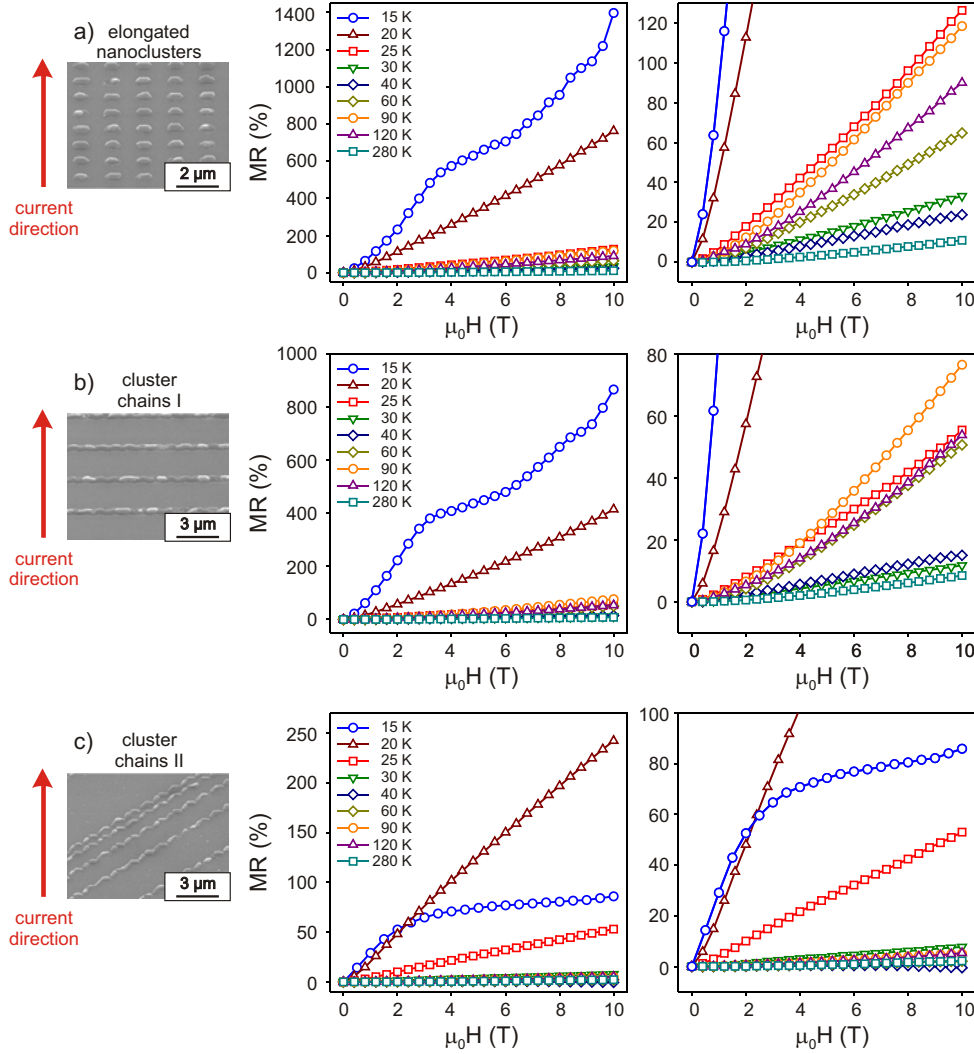
Figure 4.13: Measured magnetoresistance of regularly arranged elongated nano-
clusters a), and two different arrangements with cluster chains b)
and c) in a magnetic field applied perpendicular to the sample
plane. The direction of the applied current is shown as red arrow.
In contrast to the samples with randomly distributed nanoclusters,
the samples with regularly arranged nanoclusters and chains show
large positive magnetoresistace effects at low temperatures.

with random cluster distributions. This can be seen in figure 4.14, which shows
the temperature dependence of the magnetoresistance at $\mu_0 H = 10\,\mathrm{T}$ of the
three samples with ordered cluster arrangements as well as of the sample with
randomly distributed nanoclusters and a cluster density of $6.18 \times 10^8\,\mathrm{cm}^{-2}$.
Above $30\,\mathrm{K}$, the positive magnetoresistance at $\mu_0 H = 10\,\mathrm{T}$ of the cluster ar-
rangements rises again with increasing temperature, reaching a maximum, and
finally vanishes at high temperatures similar to the samples with randomly dis-
tributed nanoclusters. But in contrast to the samples with a random cluster
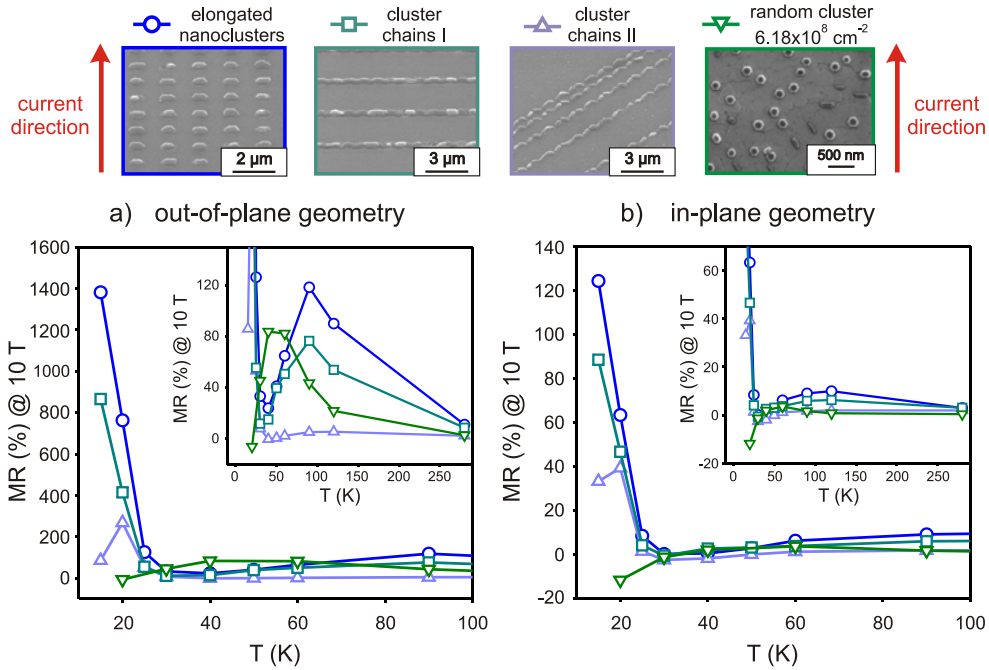
Figure 4.14: Comparison of the magnetoresistance effects at 10 T between the three samples with regular arrangements of nanoclusters and the sample with a random cluster distribution for a magnetic field orientation perpendicular to the sample plane a) and in the sample plane b).

distribution, the maximum in the positive magnetoresistance occurs at a higher temperature of about 90 K. Applying the magnetic field in in-plane geometry, only leads to a reduction of the positive magnetoresistance effects in the whole temperature range measured as shown in figure 4.14 b).

4.4.2 Magnetoresistance behaviour at temperatures above 30 K

As for the samples with randomly distributed nanoclusters, the Mn atoms diffusing into the (111)B GaAs-substrate lead to p-type conductivity of the matrix of the samples with regular arrangements of nanoclusters. Above 30 K, regular band transport dominates. The magnetoresistance effects, occuring above 30 K, can therefore be explained making the same assumptions as for describing the magnetoresistance effects of the samples with random distributions of hexagon-shaped nanoclusters. As discussed in section 4.3.2, at low temperatures a negative magnetoresistance caused by trapping effects in the vicinity of the clusters determines the magnetoresistance behaviour. At higher temperatures a positive magnetoresistance dominates, which arises from a suppression of the carrier transport through the nanocluster due to magnetic field induced changes of the band structure in the matrix. As a consequence, the current has to avoid the clusters, resulting in a change of the current path through the

matrix. The differences in the magnitude of the magnetoresistance effects can therefore directly be attributed to the different arrangements of the nanoclusters on the sample surface.

The smallest magnetoresistance effects with a maximum value of only 5% at $90\,\mathrm{K}$ occur for the cluster chains II, where the chains are oriented along the $[\bar{1}01]$-direction. Because of the orientation of the cluster chains rotated by $30°$ with respect to the direction of the applied current, the clusters do not have a large influence on the current path. In a magnetic field, where the carrier transport through the cluster chains is supressed, the cluster chains cannot block the transport through the matrix, but lead to a deflection of the current path by an angle of $30°$ compared to the current path along the $[\bar{1}\bar{1}2]$-direction in the absence of a magnetic field. For this arrangement there always exists a dominant current path through the entire matrix, which is parallel to the cluster chains. Due to the large distances between the cluster chains, which are between 1 and $5\,\mu\mathrm{m}$, this arrangement also provides wide current paths through the matrix, where the carrier transport is unaffected by the nanoclusters. Therefore the influence of these cluster chains on the transport behaviour is relatively weak.

The contrary situation can be found for the arrangement with the cluster chains I, where the cluster chains are oriented perpendicular to the current direction. For this arrangement, the cluster chains mainly suppress the transport through the matrix, if a magnetic field is applied perpendicular to the sample plane, leading to a much larger positive magnetoresistance effect of 80% compared to 5% of the arrangement with the cluster chains II. However, as can be seen on the MFM images shown in figure 3.14, the single cluster chains exhibit gaps, where the nanoclusters did not grow regularly in the openings. These gaps, which are up to $1\,\mu\mathrm{m}$ in size, provide a possible transport path for the current through the matrix, without being blocked by the clusters, and probably reduce the magnetoresistance effects compared to the corresponding ideal arrangement with continuous cluster chains.

The largest positive magnetoresistance effect with a value of 120% at $90\,\mathrm{K}$ can be observed for the regular arrangement of elongated nanoclusters, although this cluster arrangement may provide several transport pathes for the current around the single nanoclusters. From the theoretical calculations described in section 4.3.5, one would therefore expect a magnetoresistance effect, which is smaller than the one observed for the arrangement with the cluster chains I, in contradiction to the experimental results. However, for the arrangement with the cluster chains I, the increase of the total resistivity caused by the magnetic field is larger than for the arrangement with elongated nanoclusters. But due to the increased resistivity of the cluster chains I in the absence of a magnetic field, the relative change of the resistivity in a magnetic field is weaker, leading to the smaller positive magnetoresistance effect observed. The differences in the total resistivity of the two arrangements, which consist of the same number of nanoclusters, may originate from the two different cluster arrangements.

Furthermore, because Mn can only diffuse into the matrix at the openings, it may not be distributed homogeneously in the matrix. For example, for the arrangement with elongated nanoclusters a more or less homogeneous distribution of the Mn can be assumed, due to the regular arrangement of nanoclusters.

For the arrangement with the cluster chains I the Mn content in the matrix be-
tween two cluster chains is probably much lower than in the vicinity of the
clusters due to the large distance between the single cluster chains, leading to
an increase of the total resistivity.

The inhomogeneous Mn distribution in the GaAs matrix was not taken into ac-
count in the theoretical calculation described in section 4.3.5, which may be the
main reason, why the calculations cannot explain, that the arrangements with
elongated nanoclusters show a larger magnetoresistance effect than the cluster
chains I. Due to the fabrication process of the MnAs nanocluster arrangements,
a homogeneous distribution of the Mn in the matrix, as it was assumed for the
calculations, is difficult to realize because the growth of the clusters influences
the local Mn content of the matrix. In order to clarify, if the inhomogeneous
Mn distribution is responsible for the observed discrepancies between theory
and experiment, it would be necessary to expand the theory for inhomogeneous
Mn distributions in the matrix.

However, comparing the two different cluster chain arrangements, a good agree-
ment between theory and experiment is found. As predicted by the theoretical
calculations shown in figure 4.12, for the arrangement with the cluster chains I,
where the chains are arranged perpendicular to the applied current direction,
the carrier transport along the current direction is suppressed by the cluster
chains leading to strong positive magnetoresistance effects. A rotation of the
cluster chains along the direction of the applied current, as somewhat corre-
sponding to the cluster chains II, results in a vanishing of the positive magne-
toresistance, which is also in accordance with experiment. The experimental
results therefore confirm the theoretical predictions by Michel at al. [11], that
the magnetoresistance effects can be tuned in a controlled way by changing the
nanocluster arrangement.

4.4.3 Transport behaviour at low temperatures

While the magnetoresistance at temperatures above 30 K shows the same quali-
tative behaviour as for the samples with a random distribution of hexagon-
shaped nanoclusters, a totally different behaviour is found at temperatures
below 30 K. For the different regular arrangements of nanoclusters no domi-
nant negative magnetoresistance effect is observable, which is in contrast to the
samples with random cluster distributions. Instead, the arrangements exhibit
a large positive magnetoresistance with a maximum at about 20 K.

The strong differences in the magnetoresistance effects at low temperatures are
likely to arise due to a different transport regime. Due to the much lower Mn
content in the samples with regular nanocluster arrangements, most of the carri-
ers may not be activated into the valence bands at low temperatures. Therefore,
hopping conductivity is the dominating transport mechanism in this tempera-
ture range. Increasing the temperature or increasing the impurity concentra-
tion, like in the case of the samples with randomly distributed nanoclusters,
leads to a regime of extended band transport, which results in the magnetore-
sistance behaviour as discussed above.

Hopping conductivity

Hopping conductivity, which was theoretically predicted by B. Gudden and W. Schottky in 1935 [156], occurs at temperatures, where the thermal energy $k_\mathrm{B}T$ is smaller or of the order of the ionization energy E_0 of the impurities. In the hopping regime the transport is not carried by the extended band states, but is mainly determined by carriers hopping directly between the impurity sites, i.e. from occupied to empty ones. The probability of such a hop Γ_{ij} between two impurity states i and j is given by [157]:

$$\Gamma_{ij} = \Gamma_{ij}^0 \exp\left(-\frac{2r_{ij}}{a_\mathrm{B}} - \frac{\epsilon_{ij}}{k_\mathrm{B}T}\right),\tag{4.7}$$

where r_{ij} is the distance between the two impurity sites, a_B their effective Bohr radius and $\epsilon_{ij} = \frac{1}{2}(|\epsilon_i - \epsilon_j| + |\epsilon_i - E_\mathrm{F}| + |\epsilon_j - E_\mathrm{F}|)$ denotes the energetic distance between the occupied and empty impurity sites. For hopping conductivity the presence of empty impurity sites is a necessary condition, which can be fulfilled at low temperatures by compensation only. In the case of the regular arrangements of nanoclusters the compensating impurities may be manganese interstitials (Mn_i) in the GaMnAs matrix, which act as double donors [158].

One distinguishes between two different hopping mechanisms. The first one is the nearest-neighbour hopping, where the activation energy for hopping between neighbouring impurity sites ϵ_3 is assumed to be constant and the average hopping length is of the order of the mean distance between the impurities and not varying with temperature. In this scenario, the carrier has to emit or absorb phonons while hopping between the impurities, in order to overcome the energetic difference between neighbouring impurity states. The contribution to the conductivity therefore exhibits an exponential dependence on the temperature. The overall conductivity is then given by [157]:

$$\rho^{-1}(T) = \rho_1^{-1}e^{-\epsilon_1/k_\mathrm{B}T} + \rho_3^{-1}e^{-\epsilon_3/k_\mathrm{B}T},\tag{4.8}$$

where the first term corresponds to the band conductivity with the activation energy $\epsilon_1 \approx E_0$ and the second one describes the contribution due to the nearest neighbour hopping.

The second hopping mechanism, which may determine the transport at low temperatures in systems with localized states near the Fermi energy, is the so-called variable range hopping. Due to the exponential dependence of the hopping probability on the difference in energy of the two impurity states involved, only states in a small, narrow band around the Fermi energy can contribute to the transport at low temperatures. Hopping between two sites, which are widely spacially separated but very close to the Fermi energy, can therefore be more likely than hopping between neighbouring sites with a large energetic difference. In this case, the hopping length increases with decreasing temperature in contrast to nearest neighbour hopping. In 1968 N.F. Mott showed, that the contribution of variable range hopping to the temperature dependence of the resistivity is given by [159]:

$$\rho(T) = \rho_0 \exp\left[\left(\frac{T_0}{T}\right)^{\frac{1}{4}}\right],\tag{4.9}$$

with

$$T_0 = \frac{\beta}{k_{\mathrm{B}} D(E_{\mathrm{F}}) a^3},\qquad(4.10)$$

where β is a numerical coefficient, $D(E_{\mathrm{F}})$ is the density of states at the Fermi energy and a denotes the localization radius of states near the Fermi energy. Today, equation (4.9) is known as Mott's law, which shows excellent agreement with temperature-dependent resistivity measurements of amorphous semiconductors. In crystalline materials the exponential factor 1/4 has to be replaced by 1/2, due to the Coloumb interaction, which leads to diminishing of the density of localized states at the Fermi energy, the so-called Coulomb gap [157].

Origin of the positive magnetoresistance effects in the hopping regime

Assuming hopping conductivity for the samples with regular arrangements of nanoclusters and cluster chains at low temperatures, the large positive magnetoresistance effects can be explained with a transport mechanism motivated by the work of H. Kamimura [160], who considered spin effects in the case of hopping conductivity. The principle idea of Kamimura will be described in the following.

The Pauli principle allows, that each impurity site can be occupied by two carriers with different spin orientation. However, due to the Coulomb repulsion between the two carriers, impurity states occupied by two carriers have a larger energy compared to singly occupied ones. As a consequence, there exist two impurity bands, which are well separated by the so-called Coulomb gap. Therefore at low temperatures only singly occupied states can be found below the Fermi energy, which is located between the two impurity bands. Transport occurs in the impurity band by hopping from a occupied state to an empty one generated either by ionization or compensation.

However, in the case of the samples with regular arrangements of nanoclusters, both impurity bands can be assumed to be broadened, due to the fluctuations of the Mn content and disorder in the GaMnAs matrix. This broadening results in an overlap of the two different impurity bands, so that, at low temperatures, also doubly occupied impurity states exist below the Fermi energy. Due to the existance of doubly occupied impurity sites, hopping is not only possible between singly occupied and empty impurity sites, but also from doubly occupied to singly occupied or empty ones as well as between two singly occupied impurity sites.

If a magnetic field is applied, the p-d interaction leads to a splitting of the impurity states with different spin orientation similar to the giant Zeeman splitting of the extended band states described in section 4.3.1. The resulting impurity band structure is schematically shown in figure 4.15. The alignment of the spins in a magnetic field reduces the overlap of the two impurity bands with different spin orientation. As a consequence, the probability of finding a doubly occupied impurity site below the Fermi energy decreases with increasing field and hopping into empty states is the only possibility. Applying a magnetic field
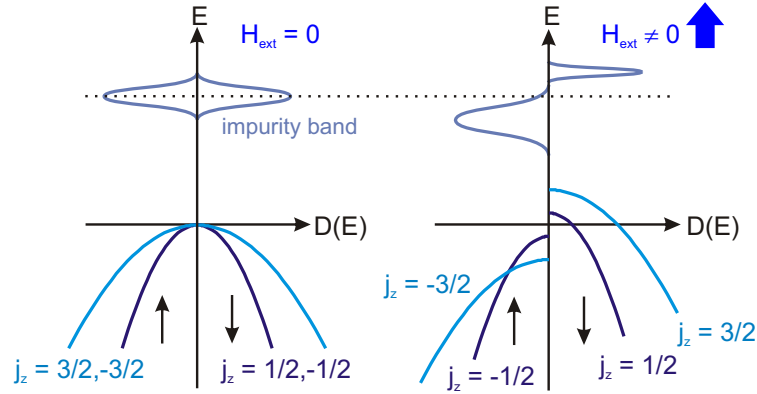
Figure 4.15: Schematic illustration of the influence of an applied magnetic field
            on broadened impurity bands in a p-type paramagnetic semicon-
            ductor. Without a magnetic field the impurity bands are spin-
            degenerate (left). Applying a magnetic field not only results in a
            splitting of the impurity bands due to the p-d interaction, but also
            influences their width (right).

therefore drastically reduces the number of possible hopping sites leading to a
positive magnetoresistance effect.

A comparison of the positive magnetoresistance effects also shows, that their
magnitude at low temperatures correlates with the magnitude of the positive
magnetoresistance in the temperature regime of extended band transport. The
largest positive magnetoresistance in the hopping regime can again be found
for the sample with regularly arranged elongated nanoclusters, while the lowest
effect is observable for the arrangement with the cluster chains II. This means,
that also in the hopping regime, the cluster arrangement strongly influences
the transport properties, resulting in an additional positive contribution to the
magnetoresistance. The basic idea for explaining this additional contribution is
based on similar assumptions than those made for describing the positive mag-
netoresistance in the case of extended band transport. As described above, in
the absence of a magnetic field the hopping conductivity in the matrix is carried
by holes from both impurity spin subbands at the Fermi energy and the carri-
ers with a spin orientation parallel to the spin polarization of the ferromagnetic
nanoclusters can pass through the clusters. Applying a magnetic field, leads
to a splitting of the impurity spin subbands due to the p-d exchange interac-
tion. In this case, the hopping conductivity is carried by one spin orientation
only due to the alignment of the carrier spins in the impurity band. Therefore
the transport through the clusters, whose spin orientation is opposite to those
of the majority carriers in the matrix, is suppressed leading to the additional
positive contribution to the magnetoresistance.

Also the negative contribution to the magnetoresistance, which occurs at
around $3.5\,\mathrm{T}$ and leads to a bending in the slope of the magnetoresistance,
can be explained by assuming hopping conductivity as dominating transport
mechanism. The p-d exchange interaction not only leads to a splitting of the

broadened impurity bands, but also influences their energetic width. Because
the spin-splitting of the impurity bands depends linearly on the effective Mn
concentration, it is larger for higher Mn concentrations. Thus, in the impurity
subband of lower energy, where the hopping takes place, the higher energy
impurity levels get closer to those with lower energy with increasing magnetic
field.   The width of the lower impurity subband therefore shrinks slightly
increasing the number of possible hopping sites at the same energy. Therefore
more impurity sites can contribute to the hopping transport resulting in a
negative contribution to the magnetoresistance. For the impurity subband at
higher energy the contrary situation is found. Because the p-d interaction acts
in the opposite direction due to the opposite spin orientation, the magnetic
field results in a further broadening of the impurity subband. The influence of
the magnetic field on the shape of the impurity subbands is also schematically
shown in figure 4.15.

Increasing the temperature, increases the probability of hopping, because more
carriers can overcome the energetic distance between neighbouring impurity
sites, i.e. the band around the Fermi energy, in which the impurity states
contribute to the transport, is broadened.   The decrease of the energetic
distance between the impurity sites due to the shrinking of the impurity band
in a magnetic field therefore becomes less important, shifting the onset of the
negative magnetoresistance to higher fields.   At a temperature of $20\,\mathrm{K}$, the
negative contribution to the magnetoresistance finally vanishes completely
for all regular arrangements of nanoclusters investigated and only the strong
positive magnetoresistance remains.

**Influence of the nanocluster arrangements on the current-voltage
characteristics in the hopping regime**

Besides the large positive magnetoresistance effects, the samples with regular
arrangements of nanoclusters and cluster chains also show a strong dependence
of the magnitude of the magnetoresistance effects on the magnitude of the cur-
rent applied to the samples. In order to investigate this behaviour further,
measurements of the current-voltage characteristics at various magnetic fields
were performed at $15\,\mathrm{K}$. The results of the these measurements as well as the
magnetoresistance for different applied current densities are shown in figure 4.16
a) and b) for the two arrangements with cluster chains I and II, respectively.

For both arrangements the magnitude of the positive magnetoresistance de-
creases with increasing current, while the qualitative behaviour of the magne-
toresistance effect remains unaffected by the applied current density. For the
arrangement with the cluster chains I the magnitude of the positive magnetore-
sistance is drastically reduced with increasing current. Applying a current of
$500\,\mathrm{pA}$ the positive magnetoresistance reaches a value of $900\,\%$ at a magnetic
field of $\mu_0 H = 10\,\mathrm{T}$, but shows only a value of around $180\,\%$ at $10\,\mathrm{T}$, if the
current stength is increased to $2\,\mathrm{nA}$. For the arrangement with cluster chains II,
the magnetoresistance at $10\,\mathrm{T}$ decreases from $85\,\%$ to $42\,\%$ in the same current
range. For both arrangements, the decrease of the magnetoresistance effect does
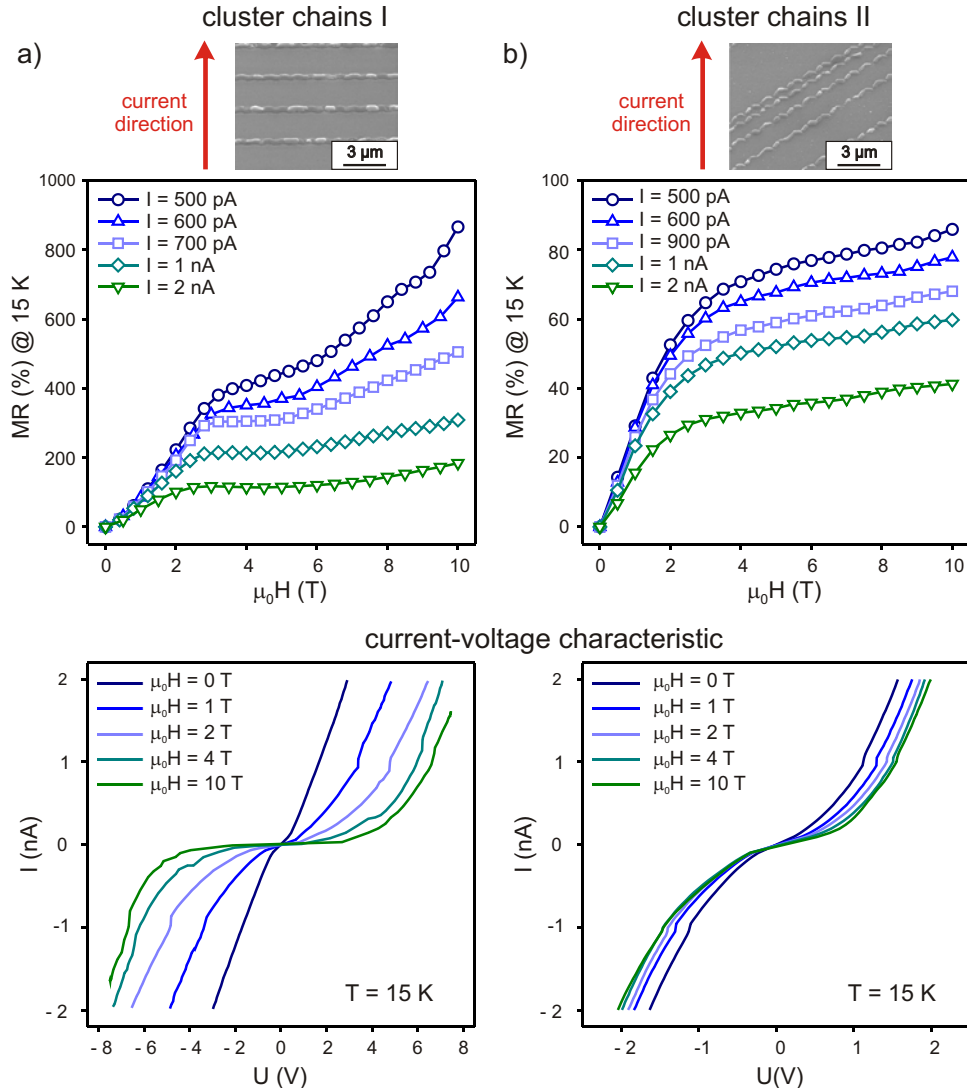not depend linearly on the applied current, but becomes weaker with increasing

Figure 4.16: Dependence of the magnetoresistance on the applied current density and current-voltage characteristics of the arrangements with cluster chains I and cluster chains II at 15 K. Increasing the applied current strongly reduces the magnetoresistance effects.

current and finally saturates for high currents.

Figure 4.16 also shows the corresponding current-voltage characteristics. For both arrangements a nearly ohmic behaviour can be found in the absence of an external magnetic field. Only a small rectifying behaviour is observable, which may originate from the formation of a Schottky barrier at the cluster-matrix interface as described in section 4.3.2. With increasing field, the rectifying behaviour of the arrangement with cluster chains I gets strongly pronounced leading to the observed strong dependence of the magnitude of the magnetoresistance effects on the applied current strength. For the arrangements with cluster chains II, the influence of the magnetic field on the current-voltage char-
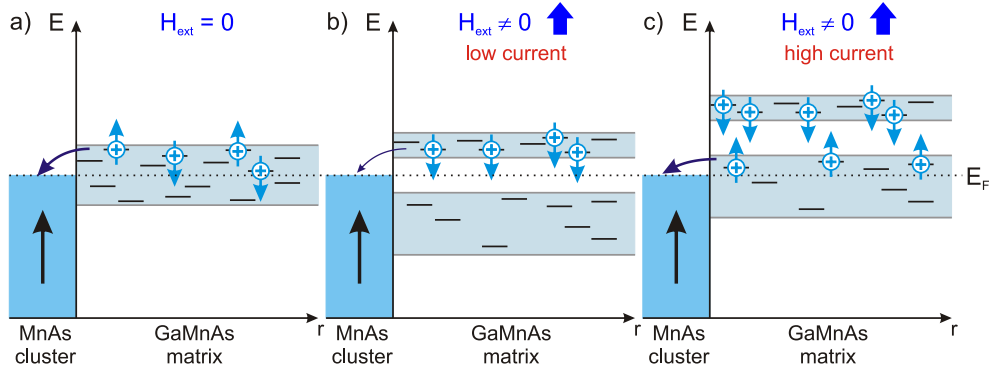
Figure 4.17: Possible origin of the rectifying current-voltage characteristic in a magnetic field. a) In the absence of a magnetic field, the carriers with a spin orientation parallel to the cluster polarization can pass the cluster. b) Due to the alignment of the carrier spins in a magnetic field, the transport through the clusters is suppressed. c) Increasing the applied current, increases the number of minority carriers in the matrix, which can pass the clusters even in the presence of a magnetic field.

acteristic is much weaker, which is also reflected in the measurements of the magnetoresistance for different applied currents. With increasing temperature the rectifying behaviour disappears and at temperatures above $30\,\mathrm{K}$ an ohmic behaviour can be found for all arrangements of nanoclusters investigated.

A possible explanation for the rectifying current-voltage characteristics in an external magnetic field is schematically shown in figure 4.17. As discussed above, in a magnetic field the transport through the clusters is suppressed due to the opposite spin orientation of the majority carriers in the matrix and the clusters. This results in an additional positive contribution to the magnetoresistance, as schematically shown in figure 4.17 a) and b). However, if the current applied to the cluster arrangement is increased, more carriers are injected by the current source into the GaMnAs matrix and the number of holes in the impurity band increases. As a consequence, the Fermi energy is shifted to higher energies and also impurity sites of the second spin subband will be occupied as schematically shown in figure 4.17. Because the minority carriers in the second impurity band possess the same spin orientation as the ferromagnetic nanoclusters, they may pass the clusters, leading to a decrease of the positive magnetoresistance effect. The assumption, that the nanoclusters are responsible for the rectifying behaviour, is also supported by the measurements of the current-voltage characteristic for the two different cluster chain arrangements. For the arrangement with cluster chains I, where the cluster chains strongly influence the transport path through the matrix, a strong increase of the rectifying behaviour in a magnetic field is observed. The arrangement with cluster chains II, where the transport through the matrix is mainly unaffected by the cluster chains, shows only a weak influence of the magnetic field on the current-voltage characteristics.
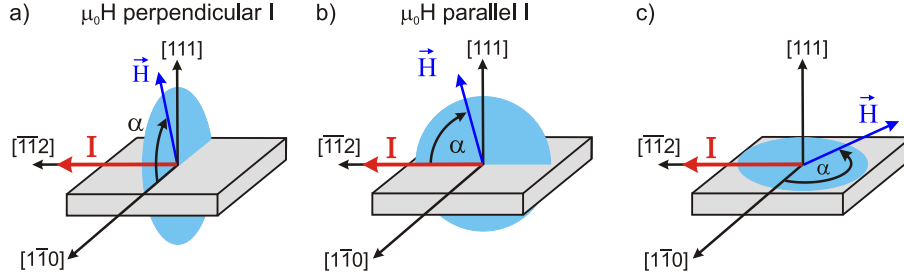
Figure 4.18: Schematic representation of the three different sample geometries for the angle-dependent transport measurements. a) For a rotation in the $(\bar{1}\bar{1}2)$-plane, the magnetic field is oriented perpendicular to the current direction for $\alpha = 0°$. b) An orientation of the magnetic field parallel to the current direction for $\alpha = 0°$ is obtained for a rotation in the $(1\bar{1}0)$-plane. c) In the in-plane geometry the magnetic field is rotated in the (111)-plane, where $\alpha = 0°$ denotes an orientation of the external field along the $[1\bar{1}0]$-direction.

4.4.4 Angle-dependent transport measurements

In order to investigate the influence of the ferromagnetic nanoclusters on the transport through the matrix in more detail, also angle-dependent transport measurements were performed. As shown by several groups [161, 162, 163], angle-dependent transport measurements are a powerful tool to probe the magnetic anisotropy as well as the switching behaviour of the magnetization in ferromagnetic (Ga,Mn)As alloys. In the case of the arrangements with nanoclusters not only the transport through the ferromagnetic clusters but mainly the transport through the paramagnetic matrix is measured. Nevertheless, in the case of the nanocluster arrangements the magnetization orientation of the nanoclusters also affects the transport properties, due to its influence on the electronic states in the matrix caused by the clusters' dipolar field. As will be shown in the follwing, the results obtained can only be understood by taking into account the transport properties of the paramagnetic matrix as well as an average magnetization orientation of the nanoclusters.

The angle-dependent measurements were performed at $15\,\mathrm{K}$ in three different geometries, which are schematically shown in figure 4.18. The first and second geometry are the two out-of-plane geometries already introduced in section 4.3.3, where the magnetic field is rotated in the $(\bar{1}\bar{1}2)$-plane and the $(1\bar{1}0)$-plane, respectively. Because the current is applied along the $[\bar{1}\bar{1}2]$-direction in the first geometry, the magnetic field is oriented perpendicular to the current direction for $\alpha = 0°$, i.e. along the $[1\bar{1}0]$-direction. For the second geometry, where the magnetic field is applied parallel to the current direction in the sample plane, an angle of $\alpha = 0°$ corresponds to $\vec{H}||[\bar{1}\bar{1}2]$. For the third geometry the magnetic field is rotated in the (111)-plane. In this in-plane geometry an angle of $\alpha = 0°$ corresponds to a magnetic field orientation parallel to the $[1\bar{1}0]$-direction. For the measurements a sample holder was used, which can be rotated continously in out-of-plane and in-plane geometries. Unfortunately, for the out-of-plane

measurements, the sample holder can only be rotated between $\alpha = -15°$ and $175°$, while for the in-plane measurements only a rotation between $\alpha = 20°$ and $300°$ is possible.

Theoretical description of the magnetic field dependence of the resistivity

For a theoretical description of the transport measurements, at first three unit vectors $\vec{k}$, $\vec{n}$ and $\vec{t}$ are introduced, which are parallel to the current direction, the surface normal and defined by $\vec{t} = \vec{k} \times \vec{n}$, respectively. With these definitions and using Ohm's law

$$\vec{E} = \boldsymbol{\rho}(B)\vec{j} \tag{4.11}$$

as defined in equation (1.65) the magneto resistivity ρ_{MR} and the Hall resistivity ρ_{Hall} can be written as [161, 163]:

$$\rho_{\mathrm{MR}} = \frac{E_{\mathrm{long}}}{j} = \vec{k} \cdot \boldsymbol{\rho}(B) \cdot \vec{k} \tag{4.12}$$

and

$$\rho_{\mathrm{Hall}} = \frac{E_{\mathrm{trans}}}{j} = \vec{t} \cdot \boldsymbol{\rho}(B) \cdot \vec{k}, \tag{4.13}$$

where $E_{\mathrm{long}} = \vec{k} \cdot \vec{E}$ and $E_{\mathrm{trans}} = \vec{t} \cdot \vec{E}$ are the components of the electric field along and perpendicular to the applied current direction $\vec{j} = j \cdot \vec{k}$, respectively. Following the ansatz of Birss [164] and Muduli [165] the resistivity tensor, which depends on the direction of the magnetic field, can be written in a series expansion in powers of B_i:

$$\rho_{ij}(B) = a_{ij} + a_{ijk}B_k + a_{ijkl}B_kB_l + ..., \tag{4.14}$$

where the Einstein summation convention is used.
For ferromagnetic materials at low external magnetic fields, where $|\vec{M}| \gg |\mu_0\vec{H}|$, the magnetic flux density $\vec{B} = \mu_0(\vec{H} + \vec{M})$ in equation (4.14) can be replaced by only the contribution of the magnetization [161, 163]. However, in the case of the nanocluster arrangements investigated, the influence of the external magnetic field $\mu_0\vec{H}$ on the paramagnetic matrix cannot be neglected, because the transport properties are mainly determined by the behaviour of the matrix and only a small contribution arises from the magnetization of the nanoclusters.
Depending on the symmetry of the material system, most of the elements of the resistivity tensor vanish. For zincblende (Ga,Mn)As one would assume at first sight, that a theoretical describtion of the angular dependence of the resistivity can be achieved with cubic symmetry T_{d}. However, in the case of ferromagnetic (Ga,Mn)As grown on (001)- and (311)A-substrate the angular dependence of the resistivity can be described very successfully only by using cubic symmetry with a tetragonal distortion along the [001]-direction, which very likely arises from compressive strain in the (Ga,Mn)As layer [163, 166]. Also in the case of the three arrangements with nanoclusters and cluster chains
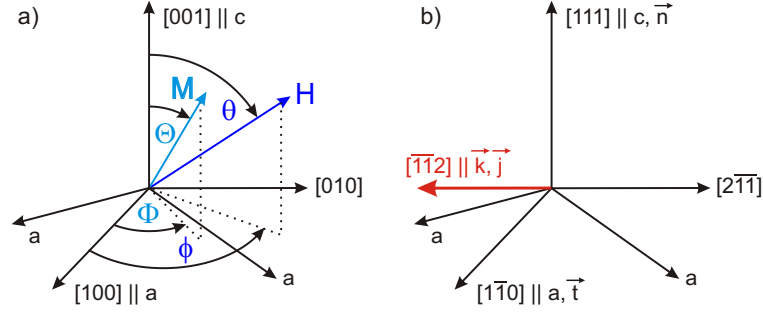
Figure 4.19: a) Definition of the cubic coordinate system with respect to the a- and c-axes of the hexagonal crystal structure. b) Orientation of the unit vectors $\vec{k}$, $\vec{n}$ and $\vec{t}$ with respect to the crystal directions of the (111)B-GaAs substrate.

investigated, which were grown on (111)B-substrates, the angular dependence of the resistivity could not be described correctly assuming cubic symmetry. A satisfying describtion was only possible for hexagonal symmetry C_{6h}, which may arise due to a distortion of the lattice along the growth direction, i.e. along the [111]-direction, caused by the diffusion of Mn into the substrate.

Following the definition of the cubic coordinate system used by Smith et al., the resitivity tensor representing the hexagonal symmetry of the system can be written up to the second order as [167]:

$$
\rho_{ij}(B) = a_{11} \begin{pmatrix} 1 & 0 & 0 \\ 0 & 1 & 0 \\ 0 & 0 & 0 \end{pmatrix} + a_{33} \begin{pmatrix} 0 & 0 & 0 \\ 0 & 0 & 0 \\ 0 & 0 & 1 \end{pmatrix} + a_{123} \begin{pmatrix} 0 & B_z & 0 \\ -B_z & 0 & 0 \\ 0 & 0 & 0 \end{pmatrix} +
$$

$$
+ \quad a_{1111} \begin{pmatrix} B_x^2 & 0 & 0 \\ 0 & B_y^2 & 0 \\ 0 & 0 & 0 \end{pmatrix} + a_{3333} \begin{pmatrix} 0 & 0 & 0 \\ 0 & 0 & 0 \\ 0 & 0 & B_z^2 \end{pmatrix} +
$$

$$
+ \quad a_{2211} \begin{pmatrix} B_y^2 & 0 & 0 \\ 0 & B_x^2 & 0 \\ 0 & 0 & 0 \end{pmatrix} + a_{3311} \begin{pmatrix} 0 & 0 & 0 \\ 0 & 0 & 0 \\ 0 & 0 & B_x^2 + B_y^2 \end{pmatrix} +
$$

$$
+ \quad a_{1133} \begin{pmatrix} B_z^2 & 0 & 0 \\ 0 & B_z^2 & 0 \\ 0 & 0 & 0 \end{pmatrix} + a_{1112} \begin{pmatrix} B_x B_y & 0 & 0 \\ 0 & -B_x B_y & 0 \\ 0 & 0 & 0 \end{pmatrix} +
$$

$$
+ \quad a_{1212} \begin{pmatrix} 0 & B_x B_y & 0 \\ B_x B_y & 0 & 0 \\ 0 & 0 & 0 \end{pmatrix}. \tag{4.15}
$$

The orientation of the coordinate system with respect to the a- and c-axes of the hexagonal system is schematically shown in figure 4.19 a). Figure 4.19 b) also shows the direction of the unit vectors $\vec{k}$, $\vec{n}$ and $\vec{t}$ as well as the crystal directions of the corresponding (111)B-GaAs substrate.

For the transport measurements the current was applied along the $[\bar{1}\bar{1}2]$-direction, which corresponds to the $[0\bar{1}0]$-direction in the new coordinate system. The expressions for the magneto and Hall resistivities are then given

by:

$$\rho_{\text{MR}} = a_{11} + a_{2211}B_x^2 + a_{1111}B_y^2 + a_{1133}B_z^2 - a_{1112}B_xB_y, \quad (4.16)$$
$$\rho_{\text{Hall}} = a_{123}B_z + a_{1212}B_xB_y. \quad (4.17)$$

As can be seen from equation (4.16) it is necessary to determine the orientation of the magnetic flux density $\vec{B} = \mu_0(\vec{H} + \vec{M})$, in order to calculate the magnetoresistivity for the different geometries measured. For this purpose, the magnetization $\vec{M}(\Theta, \Phi)$ as well as the external magnetic field $\vec{H}(\theta, \phi)$ are expressed in spherical coordinates using the defintion of angles defined in figure 4.19 a).

The orientation of the external magnetic field is determined by the corresponding measurement geometry. In order to obtain the orientation of the magnetization the free energy density U is minimized. It is given by:

$$U = -\mu_0\vec{M}\vec{H} + \frac{\mu_0}{2}\vec{M}\boldsymbol{N}\vec{M} \quad +$$
$$+K_0 + K_1\sin^2\Theta \quad + \quad K_2\sin^4\Theta +$$
$$+ \quad K_3\sin^6\Theta + K_3'\sin^6\Theta\cos(6\Phi), \quad (4.18)$$

as described in section 3.2.2.

Results in out-of-plane geometry

The angular dependence of the magnetoresistance was measured at $15\,\text{K}$ for external magnetic fields of $0.5\,\text{T}$, $1\,\text{T}$ and $10\,\text{T}$, respectively. The measurements were performed for an applied current of $2\,\text{nA}$. For both out-of-plane geometries, i.e. for a rotation of the magnetic field in the $(\bar{1}\bar{1}2)$- and the $(1\bar{1}0)$-plane, all three arrangements of nanoclusters investigated show the same qualitative behaviour at the same external magnetic field. The three samples only exhibit different magnitudes of the magnetoresistance effects. Therefore figure 4.20 shows the results of the angle-dependent resistivity measurements for the arrangement with cluster chains I only, where the cluster chains are oriented perpendicular to the current direction.

At a low magnetic field of $0.5\,\text{T}$, the measurements of the angle-dependent magnetoresistance for a rotation of the magnetic field in the $(\bar{1}\bar{1}2)$- and the $(1\bar{1}0)$-plane exhibits the same sine-dependence with a $180°$ periodicity. The sine-dependence of the magnetoresistance solely arises from the paramagnetic matrix and no influence of the ferromagnetic nanoclusters can be observed. Applying an external magnetic field of $1\,\text{T}$, the measurements for a rotation in the $(1\bar{1}0)$-plane still shows the expected sine-dependence. For a rotation in the $(\bar{1}\bar{1}2)$-plane, the measurements show an additional sharp decrease in the magnetoresistance in the vicinity of $\alpha = 0°$, where the magnetic field is oriented parallel to the nanoclusters' axes of elongation. At a large field of $\mu_0H = 10\,\text{T}$ also for a rotation of the magnetic field in the $(\bar{1}\bar{1}2)$-plane, where the magnetic field is oriented parallel to the current direction at $\alpha = 0°$, the magnetoresistance shows a deviation of the sine-dependence, if the magnetic field is oriented in the sample plane.
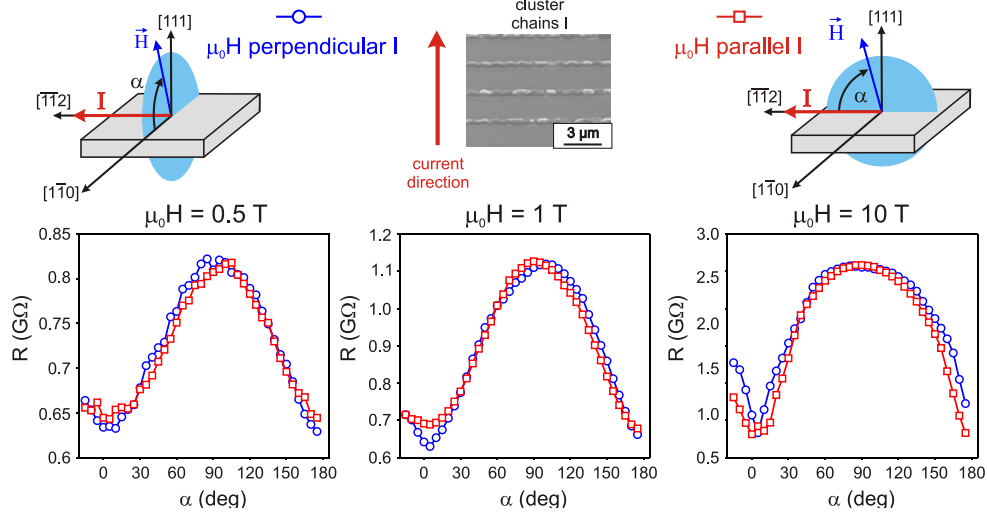
Figure 4.20: Results of the angle-dependent measurements of the magnetore-
sistance for a rotation of the magnetic field in the $(\bar{1}\bar{1}2)$- and the
$(1\bar{1}0)$-plane, shown as blue circles and red squares, respectively.
The magnetic field was increased from left to right from $0.5\,\mathrm{T}$ to
$1\,\mathrm{T}$ and finally to $10\,\mathrm{T}$.

In order to simulate and explain these results, the influence of the external
magnetic field on the average orientation of the magnetization of the nano-
clusters was taken into account. For the determination of the magnetization
orientation, equation (4.18) was minimized for the corresponding direction of
the external magnetic field. Figure 4.21 a) and b) shows the angles of the
magnetization Θ and Φ for a rotation of the external magnetic field in the
$(1\bar{1}0)$- and the $(\bar{1}\bar{1}2)$-plane, respectively, for which a good qualitative agreement
between theory and experiment was achieved for an external magnetic field
of $1\,\mathrm{T}$. The results of the corresponding calculated magnetoresistance using
equation (4.16) are presented in figure 4.21 c).

As shown in section 3.2.6, the nanoclusters exhibit an easy axes of magne-
tization along the $[11\bar{2}]$-direction. Thus, for $\alpha = 0°$ the external magnetic
field is oriented parallel to this easy axes, if the magnetic field is rotated in
the $(1\bar{1}0)$-plane. The magnetization is therefore always aligned parallel to the
external magnetic field direction, as shown in figure 4.21 a). As a consequence,
the contribution of the magnetization only increases the effective magnetic
field influencing the paramagnetic matrix and the typical sine-dependence of
the magnetoresistance is observed.

For a rotation of the magnetic field in the $(\bar{1}\bar{1}2)$-plane, the situation is different.
For $\alpha = 0°$ the external magnetic field is oriented along the $[1\bar{1}0]$-direction,
while due to the elongation of the nanocluster the main easy axes of mag-
netization is oriented along the $[\bar{1}2\bar{1}]$-direction as discussed in section 3.2.6.
As presented in figure 4.21 b) for a magnetic field orientation in the sample
plane, the magnetic anisotropy of the nanocluster may force the magnetization
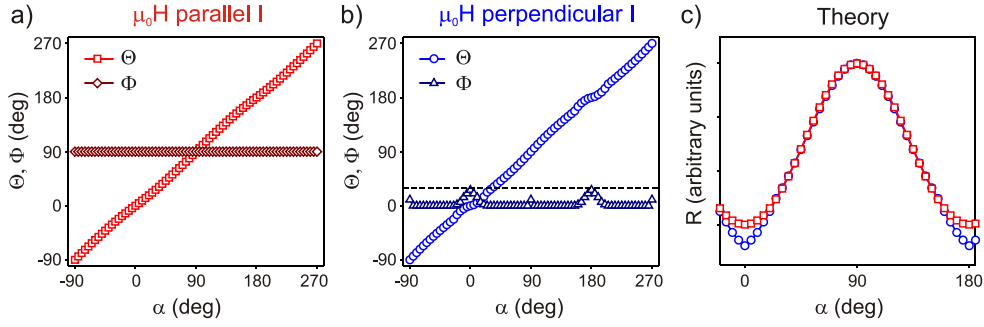to rotate into this direction. In this case, the magnetization's orientation

Figure 4.21: Calculations of the magnetization angles Θ and Φ for a rotation of
the magnetic field in the $(\bar{1}\bar{1}2)$-plane a) and the $(1\bar{1}0)$-plane b). c)
The calculated angle-dependence of the magnetoresistance shows
a good qualitative agreement with the experimental results for a
magnetic field of $1\,T$.

deviates from the one of the external magnetic field, leading not only to an
increase of the magnetic flux density but also to a change of its direction. As
shown in figure 4.21 c) this behaviour results in the observed decrease of the
resistance for an external magnetic field orientation along the $[1\bar{1}0]$-direction.
If the magnetization is neglected in the calculations, the same behaviour of
the magnetoresistance is found as for a rotation of the magnetic field in the
$[\bar{1}\bar{1}2]$-direction.

A comparison of the experimental results for the three different magnetic
field strengths shows, that with increasing magnetic field, also the influ-
ence of the magnetization increases. At a large field of $\mu_0 H = 10\,T$, even
for the out-of-plane geometry, where the magnetic field is rotated in the
$(1\bar{1}0)$-plane, deviations from the sine-behaviour in the angular dependence
of the magnetoresistance are observed. This behaviour very likely originates
from the magnetic field-induced changes of the impurity band states in the
paramagnetic matrix. Due to the giant Zeeman splitting the majority carriers
of the paramagnetic matrix possess the opposite spin orientation than the
carriers of the ferromagnetic nanoclusters, if the clusters' magnetizations
are aligned along the magnetic field direction. A rotation of the cluster
magnetization antiparallel to the field therefore reduces the magnetoresistance
effects. Because with increasing magnetic field, also the giant Zeeman splitting
in the matrix increases, the largest influence of the magnetization orientation
of the nanoclusters on the transport properties is observed at high fields.

Results in in-plane geometry

The angle-dependent measurements of the magnetoresistance in in-plane
geometry were also carried out at $15\,K$ for magnetic fields of $0.5\,T$, $1\,T$ and
$10\,T$, respectively. The applied current was $2\,nA$. For all measurements the
angle was rotated from $20°$ to $300°$ and finally back to $20°$ again. Similar to the
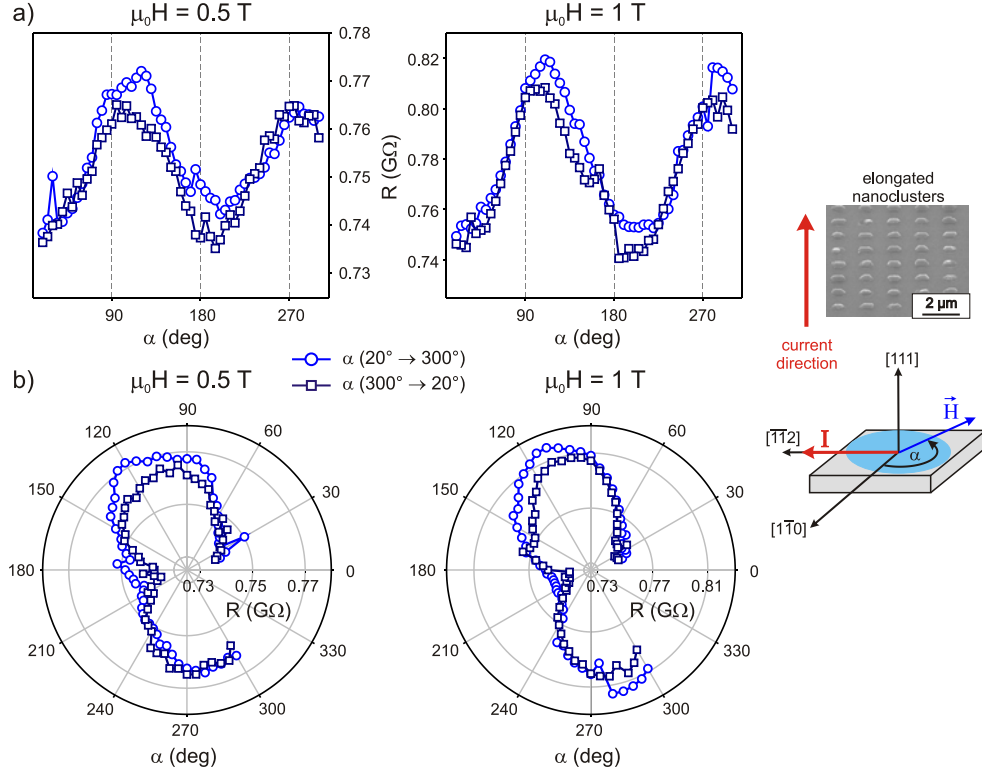measurements in out-of-plane geometry, all three cluster arrangements show

Figure 4.22: a) Plot and b) polarplot of the angle-dependent magnetoresistance in in-plane geometry for the arrangement with elongated nanoclusters. At both magnetic fields a sine-depedence of the magnetoresistance can be observed with a maximal magnetoresistance at $\alpha = 120°$.

the same qualitative behaviour of the magnetoresistance at a magnetic field of 0.5 T and 1 T. Figure 4.22 therefore shows exemplarily the results for the arrangement with isolated elongated nanoclusters at a magnetic field of 0.5 T and 1 T for the in-plane measurements. At both magnetic fields the in-plane measurements show a sine-dependence of the magnetoresistance, which is mainly caused by the transport behaviour of the paramagnetic matrix. Also the rotation direction, i.e. clockwise or anticlockwise, does not change the overall magnetoresistance behaviour. Only at about $\alpha = 180°$, where the magnetic field is oriented along the main axes of elongation of the nanoclusters, a peak in the magnetoresistance at 0.5 T can be observed for an anticlockwise rotation of the field. A similar peak at about $\alpha = 165°$ is observable for a clockwise rotation of the field at 1 T. Additionally, for clockwise rotation the magnetoresistance is smaller than for anticlockwise rotation for an angle of rotation between the peak and 90°. The occurance of this peak as well as the smaller magnetoresistance may be caused by the magnetization, which shortly remains oriented along the easy axes of magnetization parallel to the $[\bar{1}2\bar{1}]$-direction.

At a high magnetic field of $\mu_0 H = 10\,\mathrm{T}$ the influence of the nanoclusters' mag-
netization on the transport properties of the paramagnetic matrix is again much
more pronounced. For all three nanocluster arrangements the maximum of the
sine-dependence of the magnetoresistance is shifted to a higher angle of rotation
compared to lower magnetic fields and occurs at about $\alpha = 140°$. In addition,
also differences in the angle-dependent magnetoresistance behaviour can be ob-
served for the three different arrangements of nanoclusters, as presented in
figure 4.23. For the arrangement with isolated elongated nanoclusters, shown
in figure 4.23 a), the magnetoresistance is slightly decreased between $\alpha = 150°$
and $180°$, if the magnetic field is rotated from $\alpha = 20°$ to $300°$. This decrease
is even more pronounced for an clockwise rotation of the magnetic field, i.e.
from $\alpha = 300°$ to $20°$, resulting in a second local maximum of the magnetore-
sistance along the $[\bar{1}10]$-direction. Furthermore, for a clockwise rotation the
magnetoresistance is smaller compared to an anticlockwise rotation, especially
between $\alpha = 240°$ to $120°$. A similar behaviour can be observed for the ar-
rangement with cluster chains I, which is shown in figure 4.23 b). Compared
to the arrangement with elongated nanocluster, the maxmimum value of the
magnetoresistance is shifted slightly to a lower angle of rotation, while the sec-
ond maximum at $\alpha = 180°$ is much more pronounced. Again, for a clockwise
rotation of the magnetic field the magnetoresistance is decreased between $240°$
and $120°$, but shows the same qualitative behaviour as for an anticlockwise ro-
tation. The occurance of a second local maximum in the angular dependence
of the magnetoresistance along the $[\bar{1}10]$-direction cannot be observed for the
arrangement with cluster chains II. This cluster arrangement only exihibts a
sine-dependence of the magnetoresistance with a maximum at $\alpha = 140°$, as
shown in figure 4.23 c).

In order to describe the experimental results qualitatively, the magnetoresis-
tance for a rotation of the magnetic field in the sample plane was simulated
using equation (4.16). Figure 4.24 a) and b) show a comparison between the
theoretical calculations and the measurements for the arrangement with iso-
lated elongated nanoclusters as well as for the arrangement with cluster chains I,
respectively. The corresponding behaviour of the in-plane angle Φ of the mag-
netization is presented in figure 4.24 c).
Assuming an orientation of the magnetization always aligned parallel to the
external magnetic field direction, a clear sine-dependence also in in-plane ge-
ometry is observed, which is shown in figure 4.24 as black, dashed line. This
behaviour represents the contribution of the paramagnetic matrix without the
influence of the ferromagnetic nanoclusters. Similar to the out-of-plane mea-
surements, it is therefore necessary to consider the orientation of the nanoclus-
ters' magnetization for a given applied magnetic field, in order to obtain a sat-
isfying agreement between experiment and theory. For the arrangements with
elongated nanoclusters the magnetoresistance behaviour can be described very
well, if the orientation of the magnetization sometimes deviates from the exter-
nal magnetic field orientation. If the magnetic field reaches the $[11\bar{2}]$-direction,
i.e. for $\alpha = 90°$, the magnetization angle Φ remains at around $50°$. Because
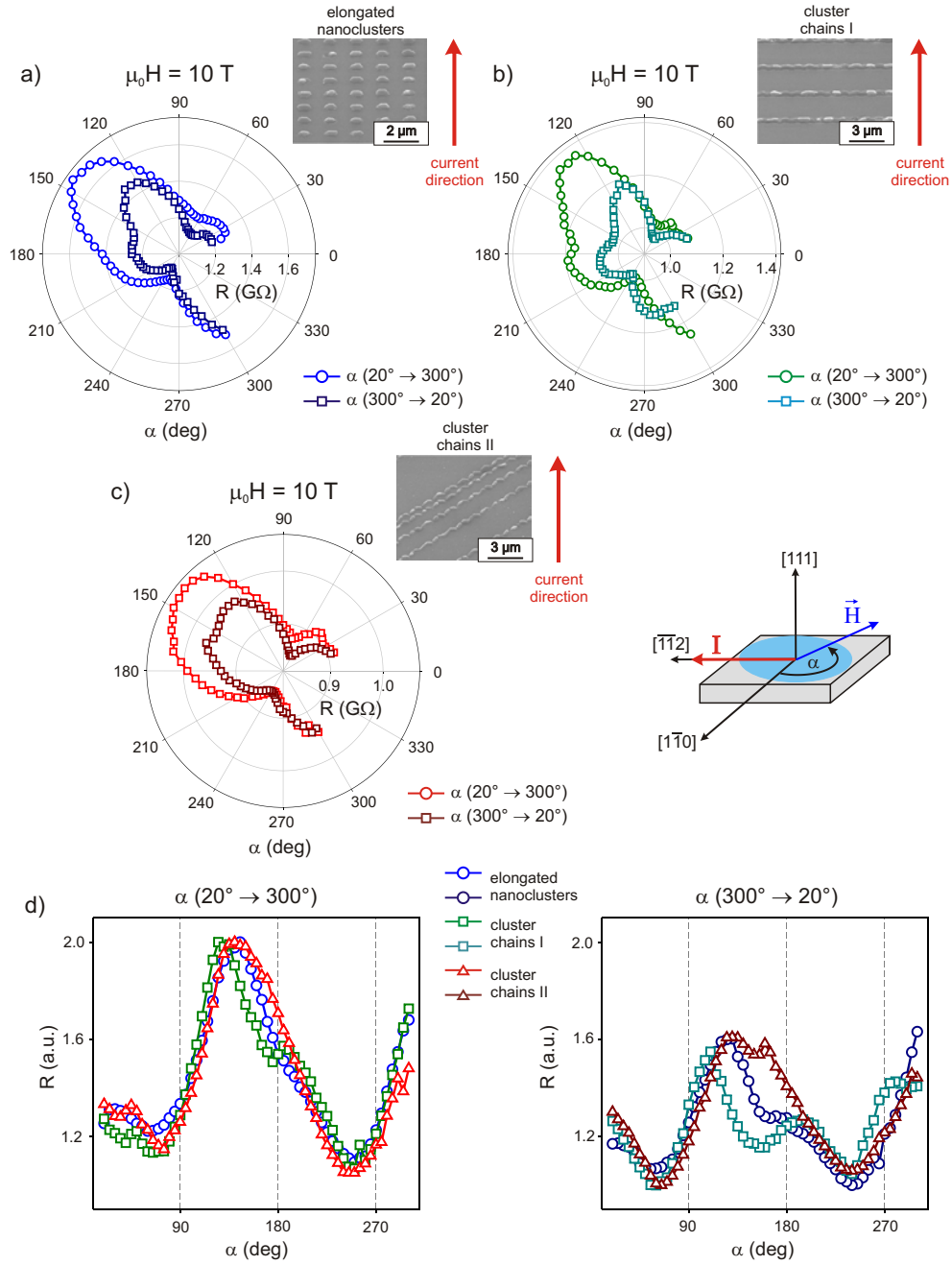the elongated nanoclusters possess an in-plane hard axes of magnetization at

Figure 4.23: Polarplot of the angle-dependent magnetoresistance in-plane ge-
ometry at 10 T for the arrangements a) with elongated nanoclus-
ters, b) with the cluster chains I and c) with the cluster chains II.
d) Comparison of the standardized in-plane magnetoresistance of
all three cluster arrangements.

$\alpha = 60°$, it seems that the magnetization prefers to stay in the vicinity of the
easy axes along the $[2\bar{1}\bar{1}]$-direction. The same behaviour can be observed, when
the magnetic field reaches $\alpha = 180°$, where it is parallel to the major axes of
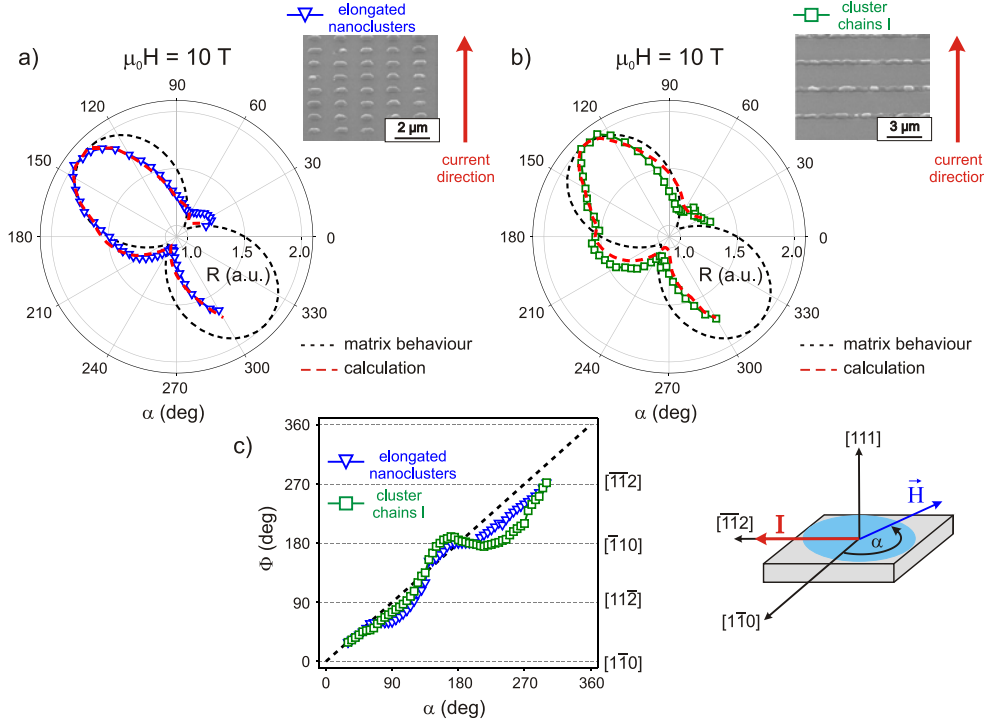
Figure 4.24: Comparison between the measurements and the calculations of the magnetoresistance in in-plane geometry at 10 T for the arrangements with elongated nanoclusters a) and with cluster chains I b). c) Plot of the corresponding in-plane angle Φ of the magnetization versus the angle of rotation of the external magnetic field α.

elongation of the nanocluster. Again the magnetization remains in the vicinity of an easy axes of magnetization resulting in the observed decrease of the magnetoresistance between 150° and 180°.

For the arrangement with cluster chains II, the situation is a little different. A correct description of the experimental results can only be obtained, if the magnetization is oriented nearly parallel to the direction of the external magnetic field between $\alpha = 30°$ and 160°. Only for $\alpha = 90°$ the magnetization shortly rotates along the easy axes occuring parallel to the $[\bar{1}\bar{1}2]$-direction. However, for $\alpha = 160°$ the magnetization rotates into the $[\bar{1}10]$-direction, i.e. parallel to the main axes of the cluster chains, and remains there until the magnetic field is rotated to $\alpha = 270°$. The strong two-fold anisotropy of the cluster chains oriented along the $[\bar{1}10]$-direction is therefore responsible for the pronounced second maximum in the angle-dependent magnetoresistance.

The angular dependence of the magnetoresistance of the arrangement with cluster chains II only exhibits a sine-dependent behaviour, as shown in figure 4.23. Because the cluster chains are arranged along the $[\bar{1}01]$-direction, the current path and thus the transport properties are nearly unaffected by the cluster arrangement as discussed in section 4.4.2. An influence of the magnetization orientation on the transport behaviour is therefore not observable.

Nevertheless, the angle-dependent measurements of the magnetoresistance for the arrangements with elongated nanoclusters and cluster chains I confirm the results of the FMR measurements presented in section 3.2.6, that the additional two-fold anisotropy due to the elongation of the nanoclusters is much stronger for the cluster chains I than for the isolated elongated nanoclusters.

Although the model used for explaining the angle-dependent magnetoresistance effects only considers an average behaviour of the magnetization, a good qualitative agreement between theory and experiment can be obtained. For a detailed description of the experimental results, the individual character of the single nanoclusters as well as the magnetic coupling between them should be taken into account. However, the angle-dependent measurements clearly show, that the magnetization orientation has an influence on the transport properties of the paramagnetic matrix, which cannot be neglected.

Summary

The magnetic and magnetotransport properties of granular hybrids with randomly arranged hexagon-shaped MnAs nanoclusters grown by MOVPE as well as of ordered arrangements of elongated nanoclusters and cluster chains grown by the new method of selective-area MOVPE were investigated in the framework of this thesis.

The self-assembled growth of MnAs nanoclusters on (111)B-GaInAs surfaces by MOVPE offers the possibility to prepare samples with randomly distributed MnAs nanoclusters of high crystalline quality. During the growth, Mn diffuses into the GaInAs surface, leading to p-type conductivity and a paramagnetic behaviour of the matrix. The investigation of the magnetic anisotropy of the nanoclusters by ferromagnetic resonance measurements reveals a hard magnetic axes along the clusters' c-axes. Their magnetization is therefore oriented in the (111)-plane, where it experiences a weak six-fold anisotropy due to the hexagonal crystal structure and the cluster shape.
The magnetoresistance behaviour of these samples exhibits a coexistence and competition between positive and negative magnetoresistance effects, which is typical for granular paramagnetic-ferromagnetic hybrid structures. The positive and negative magnetoresistance effects can be understood qualitatively by taking into account magnetic field-induced changes of the bandstructure of the paramagnetic matrix. This behaviour is in good agreement with theoretical modeling based on a resistor network model developed by Michel et al., which predicts a strong dependence of the magnetotransport properties on the cluster arrangement. However, the strong dependence of the magnetoresistance effects on the cluster arrangement and density hinders the technological application of paramagnetic-ferromagnetic hybrid structures with random cluster distributions in miniaturized magnetoelectronic devices.

The new method of self-assembled growth of MnAs nanoclusters on pre-patterned (111)B-GaAs substrate allows one to prepare ordered MnAs nanocluster arrangemements with well defined cluster size, shape and position on the GaAs substrate. This control overcomes the problem of randomness making such cluster arrangements building blocks for magnetoelectronic devices.
Regular arrangements of isolated elongated nanoclusters as well as arrangements with cluster chains were prepared by selective-area MOVPE. Investigations with scanning electron microscopy as well as atomic force microscopy reveal, that the chains consisting of nanoclusters still show some openings making an optimization of the growth process necessary. Nevertheless investigations by ferromagnetic resonance measurements reveal an additional two-fold anisotropy in the sample plane for the elongated nanoclusters as well as a magnetic cou-

pling between the nanoclusters of the cluster chains. These results are also confirmed by magnetic force microscopy, which shows an alignment of the magnetization along the clusters' main axes of elongation.

Like for the samples with randomly distributed nanoclusters positive as well as negative magnetoresistance effect are observable in the magnetoresistance measurements for the different cluster arrangements prepared. At temperatures above 30 K the results are mainly in accordance with theoretical calculations done with the resistor network model for different regular cluster arrangements. Differences can be attributed to the inhomogeneous Mn distribution in the paramagnetic matrix, which arises in the process of the controlled positioning of the nanoclusters on the substrate. Nevertheless, the experimental results confirm, that the magnetoresistance properties can be tuned in a controlled way by changing the nanocluster arrangement.

At low temperatures hopping seems to be the dominating transport mechanism leading to the occurance of large positive magnetoresistance effects. Additionally, in this temperature regime a non-ohmic current-voltage characteristic is observable, due to the influence of the nanocluster arrangements on the transport properties.

Finally, angle-dependent transport measurements show a magnetoresistance behaviour of the cluster arrangements which strongly deviates from an expected sine-dependence of the paramagnetic matrix. This behaviour can be described qualitatively by a simple model, which considers an average behaviour of the nanoclusters' magnetizations.

The obtained results show, that regular arrangements of nanoclusters or cluster chains have a large influence on the transport properties of the paramagnetic matrix, which can be understood qualitatively. However, especially at low temperatures further investigations on samples with different cluster arrangements are necessary, in order to clarify, whether the proposed mechanisms for explaining the large positive magnetoresistance effect as well as the occurrence of a non-ohmic current-voltage characteristic are correct.

Another interesting aspect of the arrangements with cluster chains is to investigate the transport through the cluster chains directly and not through the paramagnetic matrix. Especially the investigation of the transport through cluster chains consisting of nanoclusters, whose magnitizations show a different switching behaviour in an external magnetic field, will be another important step for the realization of innovative planar magnetoelectronic devices.

Bibliography

[1] P. V. Dorpe et al., Applied Physics Letters **84**, 3495 (2004).

[2] J. M. Kikkawa and D. D. Awschalom, Science **281**, 656 (1998).

[3] J. Hübner et al., Phys. Rev. Lett. **90**, 216601 (2003).

[4] M. N. Baibich et al., Phys. Rev. Lett. **61**, 2472 (1988).

[5] P. Grünberg, R. Schreiber, Y. Pang, M. B. Brodsky, and H. Sowers, Phys. Rev. Lett. **57**, 2442 (1986).

[6] M. Julliere, Physics Letters A **54**, 225 (1975).

[7] A. E. Berkowitz et al., Phys. Rev. Lett. **68**, 3745 (1992).

[8] W. Heimbrodt et al., Journal of Superconductivity and Novel Magnetism **18**, 315 (2005).

[9] H.-A. K. von Nidda et al., Journal of Physics: Condensed Matter **18**, 6071 (2006).

[10] C. Brosseau, J. B. Youssef, P. Talbot, and A.-M. Konn, Journal of Applied Physics **93**, 9243 (2003).

[11] C. Michel et al., Applied Physics Letters **92**, 223119 (2008).

[12] N. Bohr, *Studier over Metallernes Elektrontheori*, PhD thesis, Kopenhagen, 1911.

[13] H.-J. Van Leeuwen, J. Phys. Radium **2**, 361 (1921).

[14] P. Weiss, J. Phys. Theor. Appl. **6**, 661 (1907).

[15] W. Heisenberg, Zeitschrift für Physik **49**, 619 (1928).

[16] M. A. Rudermann and C. Kittel, Physical Review **96**, 99 (1954).

[17] T. Kasuya, Progress of Theoretical Physics **16**, 45 (1956).

[18] K. Yosida, Physical Review **106**, 893 (1957).

[19] E. C. Stoner, Proceedings of the Royal Society of London. Series A. Mathematical and Physical Sciences **169**, 339 (1939).

[20] R. G. Piety, Phys. Rev. **50**, 1173 (1936).

[21] M. Farle, Reports on Progress in Physics **61**, 755 (1998).

[22] M. Jamet et al., Phys. Rev. B **69**, 024401 (2004).

[23] J. Garcia-Otero, M. Porto, J. Rivas, and A. Bunde, Journal of Applied Physics **85**, 2287 (1999).

[24] Y. Liu, B. Ellman, and P. Grutter, Applied Physics Letters **71**, 1418 (1997).

[25] P. Drude, Annalen der Physik **306**, 566 (1900).

[26] P. Drude, Annalen der Physik **308**, 369 (1900).

[27] E. H. Hall, American Journal of Mathematics **2**, 287 (1879).

[28] E. Fawcett, Advances in Physics **13**, 139 (1964).

[29] J. E. Huffman, M. L. Snodgrass, and F. J. Blatt, Phys. Rev. B **23**, 483 (1981).

[30] H. Weiss and M. Wilhelm, Zeitschrift für Physik **176**, 399 (1963).

[31] C. H. Moller et al., Applied Physics Letters **80**, 3988 (2002).

[32] S. A. Solin, T. Thio, D. R. Hines, and J. J. Heremans, Science **289**, 1530 (2000).

[33] O. Madelung, Die Naturwissenschaften **14**, 406 (1955).

[34] J. Janek et al., Progress in Solid State Chemistry **32**, 179 (2004).

[35] R. Xu et al., Nature **390**, 57 (1997).

[36] M. M. Parish and P. B. Littlewood, Nature **426**, 162 (2003).

[37] G. Beck, C. Korte, J. Janek, F. Gruhl, and M. Kreutzbruck, Journal of Applied Physics **96**, 5619 (2004).

[38] M. M. Parish and P. B. Littlewood, Phys. Rev. B **72**, 094417 (2005).

[39] S. Bulgadaev and F. Kusmartsev, Physics Letters A **342**, 188 (2005).

[40] V. Guttal and D. Stroud, Phys. Rev. B **71**, 201304 (2005).

[41] W. Thomson, Proceedings of the Royal Society of London **8**, 546 (1856).

[42] I. A. Campell, A. Fert, and O. Jaoul, Journal of Physics C: Solid State Physics **3**, 95 (1970).

[43] H. Ebert, A. Vernes, and J. Banhart, Phys. Rev. B **54**, 8479 (1996).

[44] T. McGuire and R. Potter, IEEE Transactions on Magnetics **11**, 1018 (2003).

[45] O. Jaoul, I. A. Campbell, and A. Fert, Journal of Magnetism and Magnetic Materials **5**, 23 (1977).

[46] S. S. P. Parkin, N. More, and K. P. Roche, Phys. Rev. Lett. **64**, 2304 (1990).

[47] G. Binasch, P. Grünberg, F. Saurenbach, and W. Zinn, Phys. Rev. B **39**, 4828 (1989).

[48] R. Mahendiran, R. Mahesh, A. K. Raychaudhuri, and C. N. R. Rao, Journal of Physics D: Applied Physics **28**, 1743 (1995).

[49] W. P. Pratt et al., Phys. Rev. Lett. **66**, 3060 (1991).

[50] J. Q. Xiao, J. S. Jiang, and C. L. Chien, Phys. Rev. Lett. **68**, 3749 (1992).

[51] P. M. Tedrow and R. Meservey, Phys. Rev. Lett. **26**, 192 (1971).

[52] M. B. Stearns, Journal of Magnetism and Magnetic Materials **5**, 167 (1977).

[53] D. D. Djayaprawira et al., Applied Physics Letters **86**, 092502 (2005).

[54] J. Shi et al., Nature **377**, 707 (1995).

[55] P. J. Wellmann, J. M. Garcia, J.-L. Feng, and P. M. Petroff, Applied Physics Letters **71**, 2533 (1997).

[56] H. Akinaga et al., Applied Physics Letters **72**, 3368 (1998).

[57] M. Moreno et al., Physical Review B **72** (2005).

[58] M. Yokoyama, H. Yamaguchi, T. Ogawa, and M. Tanaka, Zinc-blende-type MnAs nanoclusters embedded in GaAs, volume 97, page 10D317, AIP, 2005.

[59] M. Lampalzer et al., Institute of Physics Conference Series **170**, 249 (2002).

[60] K. Volz, M. Lampalzer, A. Schaper, J. Zweck, and W. Stolz, Institute of Physics Conference Series **169**, 211 (2001).

[61] A. Chanda, H. Lenka, and C. Jacob, Journal of Superconductivity and Novel Magnetism **22**, 401 (2009).

[62] H. M. Manasevit and W. I. Simpson, Journal of The Electrochemical Society **116**, 1725 (1969).

[63] S. Hara and T. Fukui, Applied Physics Letters **89**, 113111 (2006).

[64] A. Kwiatkowski et al., Journal of Applied Physics **101**, 113912 (2007).

[65] M. Kästner, L. Däweritz, and K. H. Ploog, Surface Science **511**, 323 (2002).

[66] S. Hara, D. Kawamura, H. Iguchi, J. Motohisa, and T. Fukui, Journal of Crystal Growth **310**, 2390 (2008).

[67] S. Hara, J. Motohisa, and T. Fukui, Journal of Crystal Growth **298**, 612 (2007).

[68] S. Ito, S. Hara, T. Wakatsuki, and T. Fukui, Applied Physics Letters **94**, 243117 (2009).

[69] T. Wakatsuki, S. Hara, S. Ito, D. Kawamura, and T. Fukui, Japanese Journal of Applied Physics **48**, 04C137 (2009).

[70] S. Hara and A. Kuramata, Nanotechnology **16**, 957 (2005).

[71] M. T. Elm et al., Journal of Applied Physics **107**, 013701 (2010).

[72] J. Bardeen, L. N. Cooper, and J. R. Schrieffer, Phys. Rev. **106**, 162 (1957).

[73] J. Bardeen, L. N. Cooper, and J. R. Schrieffer, Phys. Rev. **108**, 1175 (1957).

[74] B. D. Josephson, Physics Letters **1**, 251 (1962).

[75] I. F. Gribanov and E. A. Zavadskii, physica status solidi (b) **142**, 559 (1987).

[76] T. Kim, H. Lee, J. Lee, H. Jeon, and T. Kang, Journal of Crystal Growth **292**, 62 (2006).

[77] T. Hartmann et al., Physica E **19**, 572 – 576 (2002).

[78] J. Shi et al., Magnetic properties and imaging of Mn-implanted GaAs semiconductors, volume 79, pages 5296–5298, AIP, 1996.

[79] M. Lampalzer et al., Journal of Crystal Growth **248**, 474 (2003).

[80] I. Galanakis and P. Mavropoulos, Phys. Rev. B **67**, 104417 (2003).

[81] T. Kato, K. Nagai, and T. Aisaka, Journal of Physics C: Solid State Physics **16**, 3183 (1983).

[82] R. Podloucky, Journal of Magnetism and Magnetic Materials **43**, 204 (1984).

[83] L. M. Sandratskii, R. Singer, and E. Şaşıoğlu, Phys. Rev. B **76**, 184406 (2007).

[84] P. Zeeman, Philosophical Magazine Series 5 **43**, 226 (1897).

[85] E. Zavoisky, J. Phys. U.S.S.R. **9** (1945).

[86] F. Bloch, Phys. Rev. **70**, 460 (1946).

[87] F. Bloch, W. W. Hansen, and M. Packard, Phys. Rev. **70**, 474 (1946).

[88] N. Bloembergen, Phys. Rev. **78**, 572 (1950).

[89] M. J. Pechan et al., Phys. Rev. B **65**, 064410 (2002).

[90] A. H. MacDonald, P. Schiffer, and N. Samarth, Nat Mater **4**, 195 (2005).

[91] X. Liu and J. K. Furdyna, Journal of Physics: Condensed Matter **18**, R245–R279 (2006).

[92] C. Bihler et al., Applied Physics Letters **89** (2006).

[93] C. Kittel, Phys. Rev. **73**, 155 (1948).

[94] J. H. Van Vleck, Phys. Rev. **78**, 266 (1950).

[95] A. G. Gurevich and G. A. Melkov, *Magnetization oscillations and waves*, CRC Press, 1996.

[96] W. P. Mason, Phys. Rev. **96**, 302 (1954).

[97] J. Smit and H. Beljers, Philips Research Report **10** (1955).

[98] J. Smit and H. Wijn, Advances in Electronics and Electron Physics **6**, 70 (1954).

[99] H. Suhl, Phys. Rev. **97**, 555 (1955).

[100] A. H. Morrish, *The Physical Principles of Magnetism*, Wiley, New York, 1965.

[101] Y. Takagaki, J. Herfort, and K.-J. Friedland, Phys. Rev. B **76**, 184409 (2007).

[102] M. Tanaka et al., Epitaxial ferromagnetic MnAs thin films grown by molecular-beam epitaxy on GaAs: Structure and magnetic properties, volume 76, pages 6278–6280, AIP, 1994.

[103] F. Schippan et al., Journal of Applied Physics **88**, 2766 (2000).

[104] V. A. Ivanshin et al., Phys. Rev. B **61**, 6213 (2000).

[105] S. Haneda, N. Kazama, Y. Yamaguchi, and H. Watanabe, Journal of the Physical Society of Japan **42**, 1201 (1977).

[106] R. W. D. Blois and D. S. Rodbell, Journal of Applied Physics **34**, 1101 (1963).

[107] K.-J. Friedland, M. Kästner, and L. Däweritz, Journal of Superconductivity **16**, 261 (2003).

[108] F. J. Giessibl, S. Hembacher, H. Bielefeldt, and J. Mannhart, Science **289**, 422 (2000).

[109] G. Binning and H. Rohrer, Helvetica Physica Acta **55** (1982).

[110] G. Binning, C. F. Quate, and C. Gerber, Physical Review Letters **56** (1986).

[111] G. Meyer and N. M. Amer, Applied Physics Letters **53**, 1045 (1988).

[112] Y. Martin, C. C. Williams, and H. K. Wickramasinghe, Journal of Applied Physics **61**, 4723 (1987).

[113] K. W. Edmonds et al., Journal of Applied Physics **93**, 6787 (2003).

[114] F. Matsukura, H. Ohno, A. Shen, and Y. Sugawara, Phys. Rev. B **57**, R2037 (1998).

[115] H. Ohno, Science **281**, 951 (1998).

[116] A. Van Esch et al., Phys. Rev. B **56**, 13103 (1997).

[117] C. Michel et al., Journal of Applied Physics **102** (2007).

[118] P. J. Wellmann, J. M. Garcia, J.-L. Feng, and P. M. Petroff, Applied Physics Letters **73**, 3291 (1998).

[119] S. Ye et al., Applied Physics Letters **83**, 3927 (2003).

[120] S. Ye et al., Journal of Superconductivity: Incorporating Novel Magnetism **16**, 159 (2003).

[121] S. U. Yuldashev et al., Journal of Applied Physics **90**, 3004 (2001).

[122] J. Yaeger and M. Hrusch-Tupta, editors, *Low Level Measurements Handbook: Precision DC Current, Voltage, and Resistance Measurements*, Keithley Instruments Inc., 6th edition edition, 2004.

[123] S. Hara et al., Journal of Crystal Growth **261**, 330 (2004), Proceedings of the 11th Biennial (US) Workshop on Organometallic Vapor Phase Epitaxy (OMVPE).

[124] T. Jungwirth, J. Sinova, J. Mašek, J. Kučera, and A. H. MacDonald, Rev. Mod. Phys. **78**, 809 (2006).

[125] S. Phatak, S. Bedair, and S. Fujita, Solid-State Electronics **23**, 839 (1980).

[126] C. Gould, K. Pappert, G. Schmidt, and L. Molenkamp, Advanced Materials **19**, 323 (2007).

[127] T. Jungwirth et al., Phys. Rev. B **72**, 165204 (2005).

[128] J. K. Furdyna, Journal of Applied Physics **64**, R29 (1988).

[129] T. Dietl, A. Haury, and Y. M. d'Aubigné, Physical Review B **55**, R3347 (1997).

[130] T. Dietl, H. Ohno, and F. Matsukura, Physical Review B **63** (2001).

[131] T. Dietl, H. Ohno, F. Matsukura, J. Cibert, and D. Ferrand, Science **287**, 1019 (2000).

[132] O. Goede and W. Heimbrodt, physica status solidi (b) **146**, 11 (1988).

[133] H. Akinaga, M. Mizuguchi, K. Ono, and M. Oshima, Applied Physics Letters **76**, 2600 (2000).

[134] W. Heimbrodt and P. J. Klar, Magnetic interactions in granular paramagnetic-ferromagnetic GaAs:Mn/MnAs Hybrids, in *Local-Moment Ferromagnets*, edited by M. Donath and W. Nolting, volume 678 of *Lecture Notes in Physics*, pages 167–184, Springer Berlin / Heidelberg, 2005.

[135] Y. D. Park et al., Applied Physics Letters **78**, 2739 (2001).

[136] F. Badia et al., Journal of Applied Physics **82**, 677 (1997).

[137] J. H. Jiang, Y. Zhou, T. Korn, C. Schüller, and M. W. Wu, Phys. Rev. B **79**, 155201 (2009).

[138] D. J. Hilton and C. L. Tang, Phys. Rev. Lett. **89**, 146601 (2002).

[139] J. M. Kikkawa and D. D. Awschalom, Phys. Rev. Lett. **80**, 4313 (1998).

[140] Z. G. Yu, S. Krishnamurthy, M. van Schilfgaarde, and N. Newman, Phys. Rev. B **71**, 245312 (2005).

[141] K. Ganesan and H. L. Bhat, Journal of Applied Physics **103**, 043701 (2008).

[142] C. Michel et al., Superlattices and Microstructures **37**, 321 (2005), Spintronics: Spin Injection, Transport, and Manipulation.

[143] P. Parchinskiy et al., Journal of Electroceramics **17**, 1047 (2006).

[144] M. Berciu and B. Jankó, Phys. Rev. Lett. **90**, 246804 (2003).

[145] M. C. Qian, C. Y. Fong, W. E. Pickett, and H.-Y. Wang, An ab initio investigation on the zinc-blende MnAs nanocrystallite, volume 95, pages 7459–7461, AIP, 2004.

[146] W. Schottky, Zeitschrift für Physik A Hadrons and Nuclei **118**, 539 (1942).

[147] C. Michel, *Theoretical studies of spin-dependent transport phneomena*, Cuvillier Verlag, 2007.

[148] L. Vegard, Zeitschrift für Physik **5**, 17 (1920).

[149] J. C. Woicik et al., Applied Physics Letters **68**, 3010 (1996).

[150] G. Giesecke and H. Pfister, Acta Crystallographica **11**, 369 (1958).

[151] A. Afzali-Kushaa and G. I. Haddad, Journal of Applied Physics **77**, 6549 (1995).

[152] C. R. Pidgeon and R. N. Brown, Phys. Rev. **146**, 575 (1966).

[153] H. Falk, J. Hübner, P. J. Klar, and W. Heimbrodt, Phys. Rev. B **68**, 165203 (2003).

[154] D. Suisky et al., Phys. Rev. B **58**, 3969 (1998).

[155] C. Michel, P. J. Klar, S. D. Baranovskii, and P. Thomas, Physical Review B **69** (2004).

[156] B. Gudden and W. Schottky, Zeitschrift für technische Physik **16**, 323 (1935).

[157] B. Shklovskii and A. Efros, *Electronic Properties of Doped Semiconductors*, Springer-Verlag, 1984.

[158] F. Máca and J. Mašek, Phys. Rev. B **65**, 235209 (2002).

[159] N. Mott, Journal of Non-Crystalline Solids **1**, 1 (1968).

[160] H. Kamimura, Philosophical Magazine Part B **52**, 541 (1985).

[161] M. T. Elm et al., Journal of Applied Physics **103**, 093710 (2008).

[162] S. T. B. Goennenwein et al., Physical Review B **71** (2005).

[163] W. Limmer et al., Physical Review B **205205** (2006).

[164] R. R. Birss, *Symmetry and Magnetism*, North Holland, Amsterdam, 1966.

[165] P. K. Muduli, K.-J. Friedland, J. Herfort, H.-P. Schoenherr, and K. H. Ploog, Physical Review B **72**, 104430 (2005).

[166] W. Limmer et al., Microelectronics Journal **37**, 1490 (2006).

[167] A. C. Smith, J. F. Janak, and R. B. Adler, *Electronic Conduction in Solids*, McGraw-Hill Book Company, 1967.

List of publications

- M.T. Elm, J. Teubert, P.J. Klar, W. Heimbrodt, C. Michel, P. Thomas, S.D. Baranovskii, *Transport study of annealing-induced transition from $Ga_{1-x}Mn_xAs$ alloys to GaAs:Mn/MnAs hybrids*, AIP Conference Proceedings, **893**, 1275 (2007).

- C. Michel, S.D. Baranovskii, P. Thomas, W. Heimbrodt, M.T. Elm, P.J. Klar, B. Goldlücke, U. Wurstbauer, M. Reinwald and W. Wegscheider, *Quantitative modeling of the annealing-induced changes of the magnetotransport in $Ga_{1-x}Mn_xAs$ alloys*, J. Appl. Phys., **102**, 073712 (2007).

- C. Michel, M.T. Elm, S.D. Baranovskii, P. Thomas, W. Heimbrodt, B. Goldlücke, P.J. Klar, *Influence of non-random incorporation of Mn ions on the magnetotransport properties of $Ga_{1-x}Mn_xAs$ alloys*, phys. status solidi c **5**, 819, (2008).

- M.T. Elm, P.J. Klar, W. Heimbrodt, U. Wurstbauer, M. Reinwald, W. Wegscheider, *Annealing-induced transition from a (311)A-oriented $Ga_{0.98}Mn_{0.02}As$ alloy to a GaMnAs/MnAs hybrid structure studied by angle-dependent magnetotransport*, J. Appl. Phys., **103**, 9 (2008).

- C. Michel, M.T. Elm, B. Goldlücke, S.D. Baranovskii, P. Thomas, W. Heimbrodt, P.J. Klar, *Tailoring the magnetoresistance of MnAs/GaAs:Mn granular hybrid nanostructures*, Appl. Phys. Lett., **92**, 22 (2008).

- M.T. Elm, T. Henning, P.J. Klar, B. Szyszka, *Effects of artificially structured micrometer holes on the transport behaviour of Al-doped ZnO layers*, Appl. Phys. Lett., **93**, 232101 (2008).

- C. Knies, M.T. Elm, P.J. Klar, J. Stehr, D.M. Hofmann, N. Romanov, T. Kammermeier, A. Ney, *Nonferromagnetic nanocrystalline ZnO:Co thin films doped with Zn interstitials*, J. Appl. Phys., **105**, 073918 (2009)

- M.T. Elm, C. Michel, J. Stehr, D.M. Hofmann, P.J. Klar, S. Ito, S. Hara, H.-A. Krug von Nidda, *Comparison of the magnetic properties of GaInAs/MnAs and GaAs/MnAs hybrids with random and ordered arrangements of MnAs nanoclusters*, J. Appl. Phys., **107**, 013701 (2010).

- M. Piechotka, M.T. Elm, T. Henning, B. Szyszka, B.K. Meyer, P.J. Klar, *Transport properties of microstructured MF-sputtered $Zn_{0.98}Al_{0.02}O$*, phys. status solidi c, **7**, 1580 (2010).

Acknowledgments

meinen Freunden, die nach der Arbeit immer für einen Ausgleich gesorgt haben.

Ein ganz besonderer Dank gilt meiner Familie, die mich während meiner gesamten Studienzeit unterstützt hat.

Ich erkläre:

Ich habe die vorgelegte Dissertation selbstständig und ohne unerlaubte fremde Hilfe und nur mit den Hilfen angefertigt, die ich in der Dissertation angegeben habe. Alle Textstellen, die wörtlich oder sinngemäß aus veröffentlichten Schriften entnommen sind, und alle Angaben, die auf mündlichen Auskünften beruhen, sind als solche kenntlich gemacht. Bei den von mir durchgeführten und in der Dissertation erwähnten Untersuchungen habe ich die Grundsätze guter wissenschaftlicher Praxis, wie sie in der „Satzung der Justus-Liebig Universität Gießen zur Sicherung guter wissenschaftlicher Praxis" niedergelegt sind, eingehalten.

Matthias Thomas Elm